Title	Ultra-low Reflectivity Nanocrystalline Si Solar Cells Fabricated by Surface Structure Chemical Transfer Method
Author(s)	Francisco, C. Franco Jr.
Citation	大阪大学, 2013, 博士論文
Version Type	VoR
URL	https://doi.org/10.18910/26249
rights	
Note	

Ultra-low Reflectivity Nanocrystalline

Si Solar Cells Fabricated by

Surface Structure Chemical Transfer Method

（化学的転写法を用いて形成した極低反射

ナノクリスタルシリコン太陽電池）

A Thesis Submitted to the

Department of Chemistry
Graduate School of Science
Osaka University

In Partial Fulfillment of the
Requirements for the Degree of
Doctor of Philosophy (Ph.D.)

Francisco C. Franco Jr.

September 2013

Table of Contents

Chapter I

General Introduction

1-1   General Motivation

1-1-1 The Energy Problem

The human basic needs of the modern society require the use of various forms of energy for: food, transportation, communication, etc. Therefore, in order maintain the current modern society; all our energy needs must be supplied. Fig. 1-1 shows the shares of energy sources in total global energy supply in 2008 [1], with the renewable energy sources expanded on the right. It is observed that a very large share of the energy consumed, i.e., coal, oil, and gas, are all derived from fossil fuels. Fossil fuels are non-renewable energy sources, which mean that there, will come a time when all the remaining energy reserves will be totally consumed and depleted.

1-1-2 Global Warming

In addition, in order to have a healthy and liveable environment for the future, it is imperative that the energy is supplied with low environmental impacts. Carbon dioxide, from the burning of fossil fuels has long been identified as the main cause of global warming [2]. Fig. 1-2 shows the carbon dioxide emissions from 1965 to 2011 [3]. It is observed that from 1965, the world carbon dioxide emission is steadily increasing and almost tripled after five decades. Therefore, we can safely assume that the carbon dioxide emissions will continuously rise as a result of the increase in fossil fuel burning, i.e., increasing global energy demand.
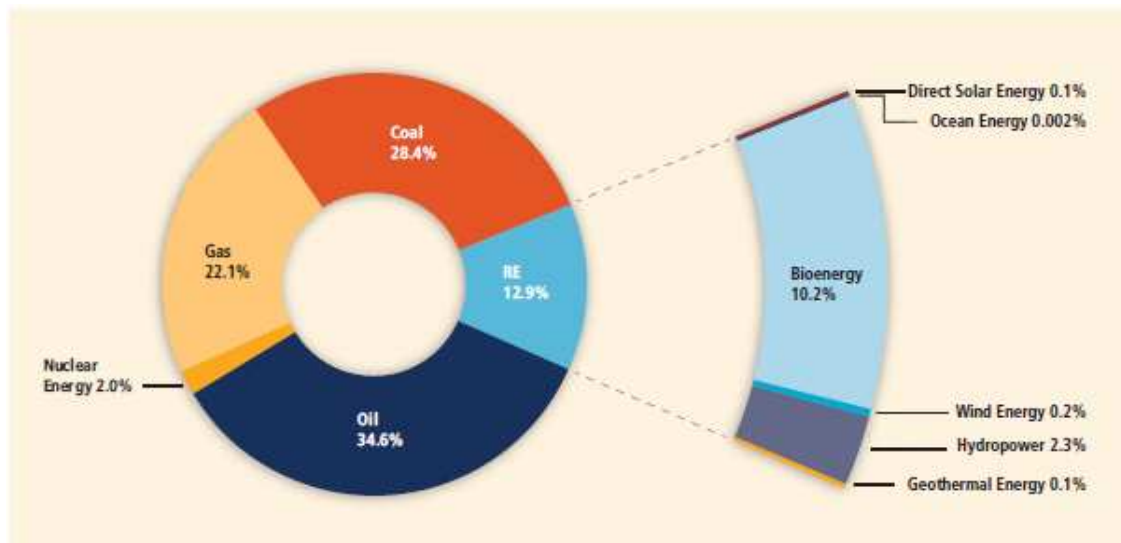
Fig. 1-1. The shares of energy sources in total global primary energy supply in 2008. The renewable energy (RE) sources are expanded on the right.
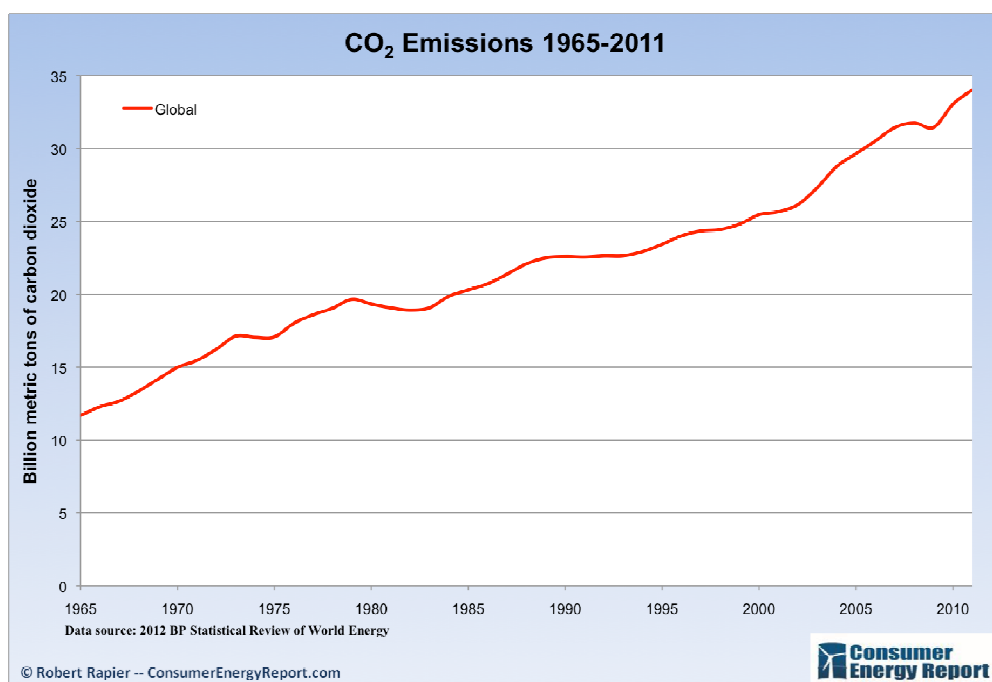
Fig. 1-2. Global CO_2 Emissions from 1965 to 2011.

1-1-3 Solar Energy as an Alternative Source of Energy

Renewable energy sources can provide sustainable energy while mitigating the effects of climate change. As shown in Fig. 1-1, the renewable energy sources only account for the 12.9% of the total global energy consumption of 2008. The particular renewable energy source of interest for this thesis is the solar energy source, which only account for 0.1% of the total global energy consumption. On the average, an area on the earth's surface receives about 1000 W/m^2 of solar energy for about 8 hours in a day for a year, which is equivalent to about 3000 hours of sunlight. In 2008, the total global energy consumption was around 143,000 TWh [4].   If we calculate for the total surface area needed to produce the same amount of energy in 2008 with a 15% efficient solar cell, then we'll get an area of about 317,000 km^2. In comparison, this area is a little less than the total land area of Japan, i.e., 377,000 km^2 or just about 3.5% the land area of Sahara desert, i.e., 9,000,000 km^2. This rough estimate shows that it is very possible to supply the global energy needs using only solar energy.   However, the current commercial solar cell efficiencies (Fig. 1-3), i.e., 15~21% [5], and the high production costs limit the full potential of using solar cells for household and commercial use. Therefore, great efforts must be given to the study of solar cells in order to maximize the use of the free and clean solar energy. In the next section, the details on how solar cells convert solar energy into electrical energy will be discussed.
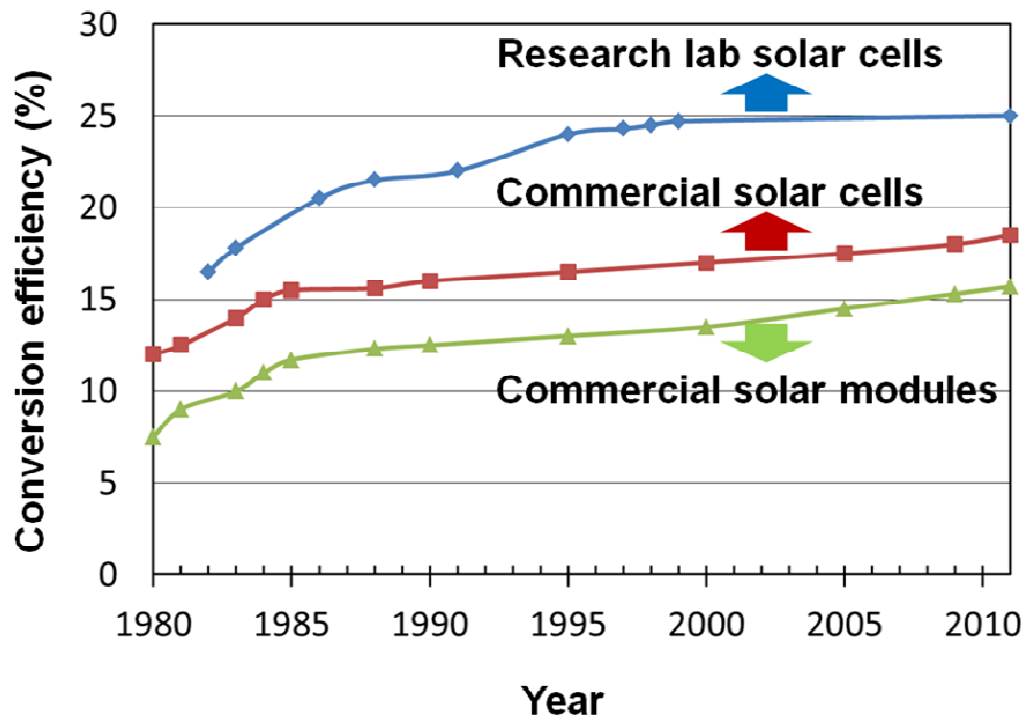
Fig. 1-3.   Conversion efficiencies vs. year for research lab. commercial solar cells and commercial solar modules.

1-2   Solar Cells

1-2-1 Si solar cells

There are various types of solar cells, such as: single crystalline Si, polycrystalline Si, amorphous Si, thin films (CdTe, GaAs, etc.). However, in order to produce solar cells with high conversion efficiencies at a relatively low cost, the solar cell material must be of high quality, abundant raw materials and low cost of production. Since crystalline, i.e., mono- and polycrystalline, Si-based solar cells fit these criteria, we will only focus on the study of crystalline Si for this thesis.
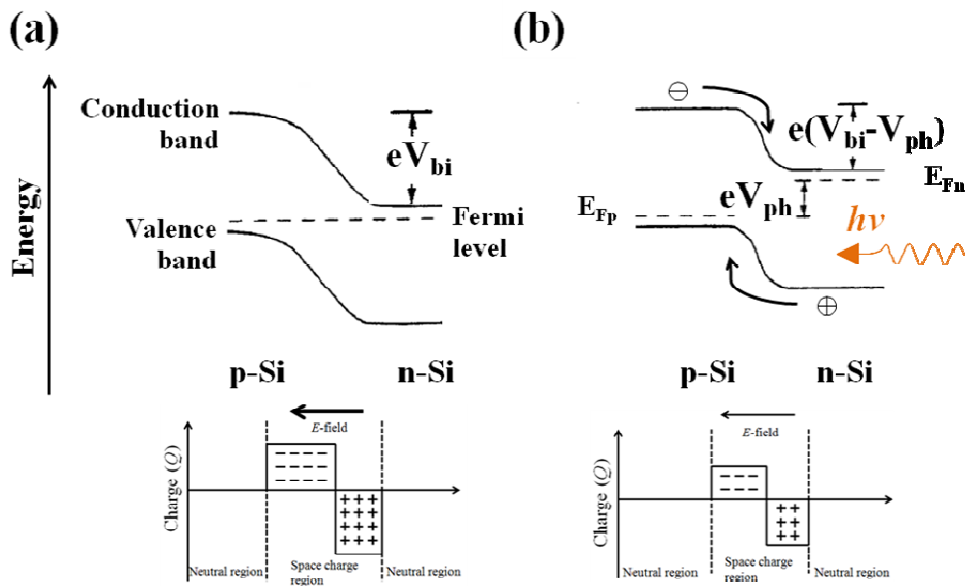
Fig. 1-4. Band diagram of a pn-junction in the dark (a) and with photovoltage, V_{ph}, generated by incident light (b).

A solar cell is a semiconductor device that converts light energy into electrical energy [6,7,8]. When a semiconductor absorbs a photon greater than its band-gap energy, an electron is excited from its valence band to the conduction band. In order to separate the generated electron-hole pairs, a built-in asymmetry must be present in the solar cell. Fig. 1-4a shows the band diagram for a pn-junction in the dark. When different regions of a semiconductor are doped differently, i.e., p- and n-type, an interface will be created in the semiconductor material. Since the work function of the p-type region is larger than the n-type region, then the electrostatic potential of the p-type will be larger than the n-type, thus, an electric field is established at the p-n junction of the semiconductor material. Fig. 1-4b shows the band diagram of a pn-junction with photovoltage, V_{ph}, generated by an incident light. After absorption of light, electron-hole pairs are generated in the material. Due to the electric field in the space charge region, electrons (holes) flow to the n-region (p-region). The electrons and holes are then enhanced above their equilibrium values, and the electron and hole quasi-Fermi levels are split. Therefore, the photovoltage, V_{ph}, is the difference between the quasi-Fermi energies of electrons and holes.
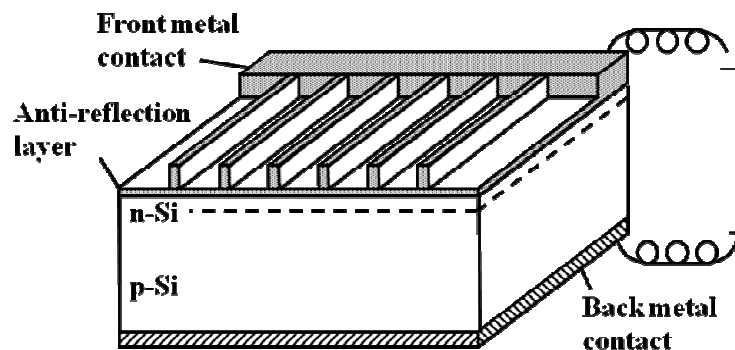
Fig. 1-5. Basic structure of a Si solar cell.

Fig. 1-5 shows the basic structure of a solar cell. A basic Si solar cell is made of a pn-junction Si material, an anti-reflection coating to reduce surface reflections, and front and back metal contacts to collect the generated current. When an incident light, as shown in Fig. 1-6, hits the solar cell, electron-hole pairs are generated. The electrons move to the n-side while the holes move to the p-side due to the electric field created at the pn-junction. The carriers are then collected at the front and back metal contacts and transported to the external circuit.
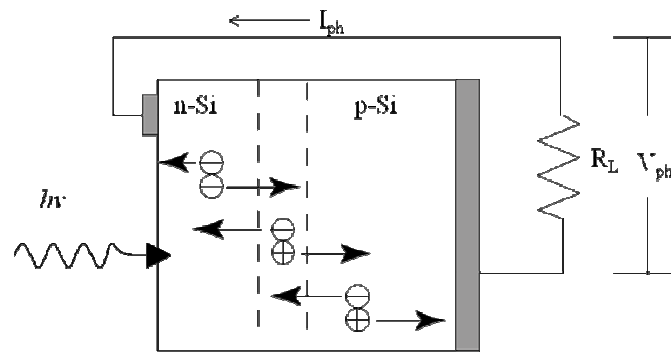
Fig. 1-6. Basic mechanism of a Si solar cell.

1-2-2   Losses in solar cells

1-2-2-1   Reflection losses in Si solar cells

The maximum theoretical conversion efficiency of a single crystalline Si solar cell under non-concentrated light illumination is 28% [9]. However, due to various loss mechanisms, as mentioned in section 1-1-3, the conversion efficiencies of current

commercial solar cells are only in the range between 15 and 21%. The two main losses in Si solar cells are the: reflection losses and recombination losses.

When light hits the Si solar cell, most of the light is reflected, i.e., above 40%, thus, not absorbed. The band-gap energy of Si is 1.1 eV [10], therefore, Si can absorb light whose wavelength is below 1100 nm. However, Si has a high refractive index, i.e., 3.9~4.5, in the range between 300 and 1100 nm [11], thus resulting in a high reflectivity. The conventional methods to produce low-reflectivity Si surfaces are: (1) formation of a textured surface [12], and (2) deposition of an anti-reflection coating [13]. The formation of a textured surface is normally done by the alkaline etching of Si (to be discussed in the next chapter) forming a pyramidal-textured Si surface. The pyramid structure allows multiple reflections on the Si surface resulting in more absorption. On the other hand, an anti-reflection coating is deposited on the Si surface in order to reduce the difference between the refractive index of air and the Si surface. The conventional anti-reflection coating used is silicon nitride, with a refractive index of ~2.

The intensity of the reflected light when passing through between media of different refractive indices was first observed by Fresnel (1827). The Fresnel equations describe the fraction of the reflected and refracted/transmitted light. Fig. 1-7 shows the reflection and transmission of light on an interface.
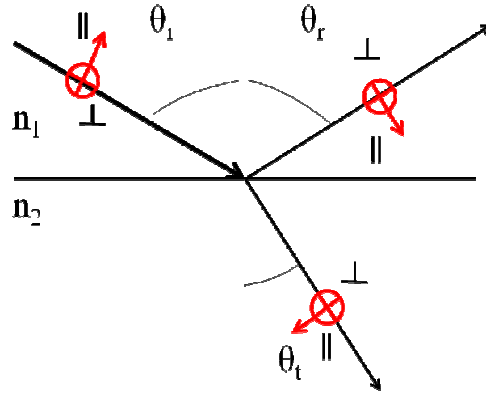
Fig. 1-7. Reflection and Transmission of light.

where θ_i, θ_r, and θ_t are the incident, reflected, and transmitted angles respectively, and the refractive indices of the two media are labelled as n_1 and n_2.

At the interface between the two media, the incident light can both be reflected and refracted. The angle of the reflected light is given by the law of reflection,

$$\sigma_i = \sigma_r \tag{1-1}$$

while the transmitted light is given by the Snell's law.

$$\frac{\sin\theta_i}{\sin\theta_t} = \frac{n_2}{n_1} \tag{1-2}$$

In order to determine the fraction of light reflected, R, the polarization of light must be considered. The electric field component perpendicular to the plane of incidence is said

to be *s*-polarized (crossed circle in Fig. 1-6), while the electric field component parallel

to the plane of incidence is said to be *p*-polarized (arrow in Fig. 1-6).

$$R_{\perp} = \left(\frac{n_1 \cos \theta_i - n_2 \cos \theta_t}{n_1 \cos \theta_i + n_2 \cos \theta_t} \right)^2 \qquad \text{(1-3)}$$

$$R_{II} = \left(\frac{n_1 \cos \theta_t - n_2 \cos \theta_i}{n_1 \cos \theta_t + n_2 \cos \theta_i} \right)^2 \qquad \text{(1-4)}$$

For the unpolarized light, i.e., having equal fractions of *s*- and *p*-polarized light, *R* can

be represented by:

$$R = \frac{R_{II} + R_{\perp}}{2} \qquad \text{(1-5)}$$

Reflections on a Si surface can be greatly reduced by applying an anti-reflection

coating, i.e., <10%. Fig. 1-8 shows the anti-reflection coating mechanism for a Si

surface. Anti-reflection coating consists of a thin layer of dielectric material, whose

thickness is chosen so that the interference effects in the anti-reflection coating can

cause the wave reflected from the anti-reflection coating surface to be out of phase with

the wave reflected from the Si surface resulting to zero net reflection as shown in Fig. 1-

8.
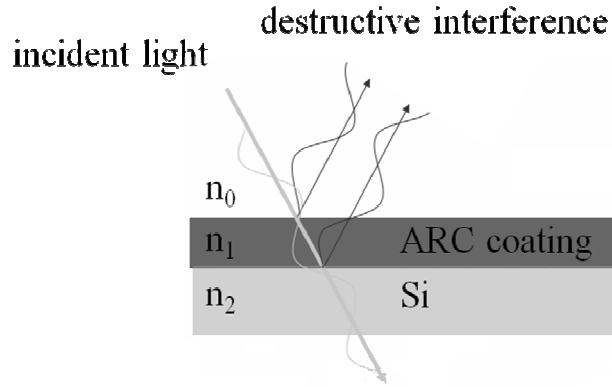
Fig. 1-8. Anti-reflection coating (ARC) mechanism.

Therefore, thickness, d, of the anti-reflection coating is chosen such that it is equal to one-quarter wavelength, λ, of the incoming light.

$$d = \frac{\lambda}{4n_1} \tag{1-6}$$

Reflectivity can be further reduced if the refractive index of the anti-reflection coating is the geometric mean of air, i.e., 1, and Si, i.e., 3.8 – 4.5, as expressed by eq. 1-7.

$$n_1 = \sqrt{n_0 n_2} \tag{1-7}$$

where n_0, n_1, and n_2 are the refractive indices of air, anti-reflection coating, and Si respectively.

1-2-2-1 Recombination losses in Si solar cells

After absorption of light, it is possible that electrons at the conduction band may recombine with holes in the valence band before electrons and holes are separated by the electric field in the space charge region. Recombinations in a solar cell normally occur through defect states such as surface defects [14], e.g., surface dangling bonds. Fig. 1-11a shows a dangling bond for Si and the electron-hole recombination through surface defect states (Fig. 1-11b). The surface defect states possess energy levels that can act as an efficient recombination center for electrons and holes. In order to reduce surface recombination centers, the surface dangling bonds must be removed by forming a passivation layer on the surface. The conventional surface passivation is normally done by the deposition of a silicon nitride layer which contains high concentration hydrogen [15].

Recombination is the process by which electron-hole pairs are lost due to the spontaneous transition of an excited electron in the conduction band to an unoccupied state (hole) in the valence band. The time-dependent decay of the excess carrier density, $\Delta n(t)$, can be expressed by the equation:

$$\frac{\partial \Delta n(t)}{\partial t} = -U(\Delta n(t), n_0, p_0) \qquad (1\text{-}8)$$

where U is the recombination rate, n_0 and p_0 are the electron and hole concentrations, and Δn is the carrier injection density. The time constant of the decay is called the recombination lifetime, τ:

$$\tau(\Delta n, n_0, p_0) = \frac{\Delta n}{U(\Delta n, n_0, p_0)} \tag{1-9}$$

As will be shown, there are various recombination mechanisms that may occur in a given sample. Therefore, the total recombination rate, U_{eff}, is expressed as the summation of the individual recombination rates of each recombination mechanism. This allows us to determine the total carrier lifetime, τ_{eff}:

$$U_{eff} = \sum_v U_v \tag{110}$$

$$\frac{1}{\tau_{eff}} = \sum_v \frac{1}{\tau_v} \tag{1-11}$$

There are three main types of recombination mechanism in semiconductors [16]. Fig. 1-9 shows the first two types of recombinations, radiative (a) and Auger (b) recombinations. Radiative recombination (Fig. 1-9a) occurs when an electron in the conduction band directly recombines with a hole in the valence band. The recombination process also releases energy in the form of photon whose energy is the same as the band-gap energy. However in Si, radiative recombination rarely occurs, due to indirect band-gap as band-to-band recombination in Si must be accompanied by phonon emission or absorption to conserve both energy and momentum. Auger recombination (Fig. 1-9b) occurs when two similar carriers collide with each other resulting to the excitation of one carrier and the recombination of another carrier with the opposite carrier across the band-gap. The energy released from the recombination

14

of the carrier is then used up as the kinetic energy of the other carrier. The gained

kinetic energy of the carrier is then lost as heat as the excited carrier relaxes to the band

edge.
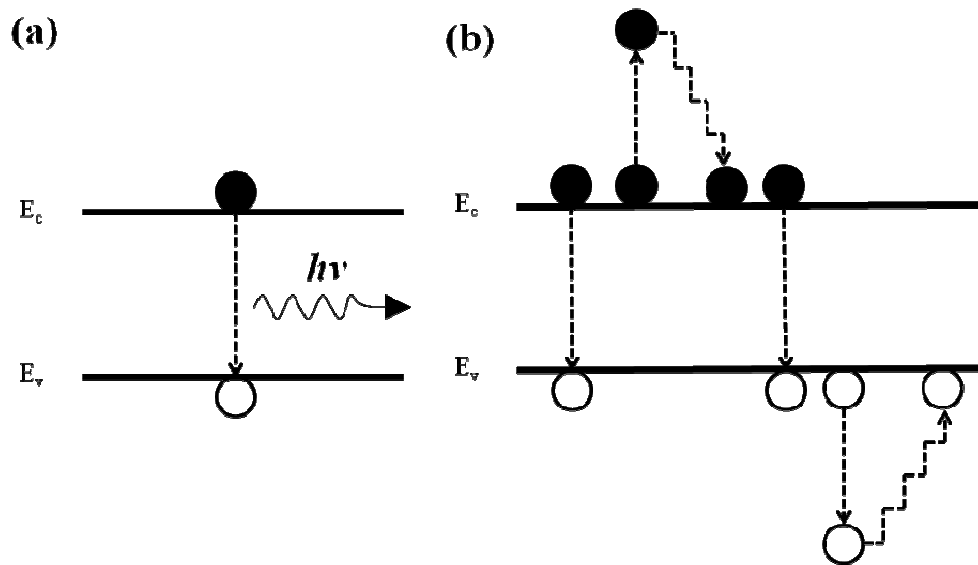
Fig. 1-9. Recombination mechanisms for electrons and holes: radiative

recombination (a), Auger recombination (b).

The third and most important type of recombination mechanism is the

recombination via defect or interface states, also called as the Shockley-Read-Hall

(SRH) recombination [18]. Fig. 1-10 shows the different interactions of carriers in the

presence of bulk defect states: 1) electron emission, 2) electron capture, 3) hole capture,

and 4) hole emission.
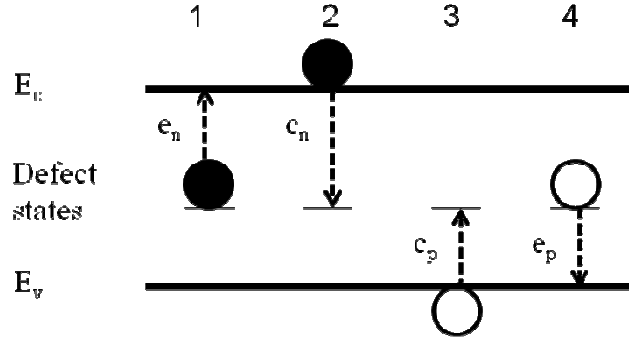
Fig. 1-10. Recombination through bulk defect states. Electron emission (1), electron capture (2), hole capture (3), and hole emission (4).

In order to determine the rates at which the electron density n in conduction band and hole density p in the valence band change, the total emission and capture due to the presence of defect states have to be balanced for both electrons and holes. The capture rates for electrons c_n^* and holes c_p^* may be expressed as:

$$c_n^* = c_n n = (\sigma_n v_{th})n \tag{1-12}$$

$$c_p^* = c_p p = (\sigma_p v_{th})p \tag{1-13}$$

If we set the electrons (holes) as having their own frame of reference, then the defect centers move randomly with a thermal velocity v_{th} while the electrons (holes) are immobile. Having a capture cross-section σ_n, the defect center then sweeps out a volume per unit time of σ_n x v_{th}.

Let N_t be the density of defect centers and f_t the probability of occupation by an electron. Since the total electron emission (total hole capture) is proportional to the

density of occupied defect centers $N_t \times f_t$ and the total electron capture (total hole emission) to the number of unoccupied defect centers $N_t \times (1-f_t)$, the time rates of change of n and p due to generation and recombination can be written as:

$$\left(\frac{dn}{dt}\right) = (1) - (2) = e_n \times N_t f_1 - c_n n \times N_t (1 - f_t) \qquad \text{(1-14)}$$

$$\left(\frac{dp}{dt}\right) = (4) - (3) = e_p \times N_t (1 - f_1) - c_p p \times N_t f_t \qquad \text{(1-15)}$$

At equilibrium, the rates of concentration change for both electrons (dn/dt) and holes (dp/dt) must be zero. Therefore, if we introduce the expressions for the equilibrium concentrations n_0 and p_0, and the occupation probability, f_t, is identified with the Fermi-Dirac distribution function, then the emission rates e_n and e_p can be expressed as functions of the defect energy E_t and the capture coefficients c_n and c_p:

$$e_n = c_n n \frac{1 - f_t}{f_t} = c_n N_c \exp\left(-\frac{E_c - E_t}{k_B T}\right) = c_n n_1 \qquad \text{(1-16)}$$

$$e_p = c_p p \frac{f_t}{1 - f_t} = c_p N_v \exp\left(-\frac{E_t - E_v}{k_B T}\right) = c_p p_1 \qquad \text{(1-17)}$$

where N_c and N_v are the effective density of states in the conduction and valence bands respectively, E_c and E_v are the energies of the conduction and valence band edges respectively. The n_1 and p_1 terms are statistical factors used in the SRH theory:

$$n_1 \equiv N_c \exp\left(-\frac{E_c - E_t}{k_B T}\right) \tag{1-18}$$

$$p_1 \equiv N_v \exp\left(-\frac{E_t - E_v}{k_B T}\right) \tag{1-19}$$

In order to find an expression for the SRH recombination rate, a non-equilibrium case must be considered. If the expression for e_n and e_p are inserted in equations 1-14 and 1-15, equating $dn/dt = dp/dt$ yields the occupation probability f_t of the defect centers as a function of the defect (n_1, p_1, c_n and c_p) and excitation (n and p) parameters. The net recombination rate for SRH recombination through defects then takes the form:

$$U_{SRH} = \left(\frac{dn}{dt}\right) = \left(\frac{dp}{dt}\right) = \frac{n_p - n_i^2}{[N_t \sigma_n v_{th}]^{-1}(p + p_1) + [N_t \sigma_p v_{th}]^{-1}(n + n_1)} \tag{1-20}$$

The recombination lifetime is defined as:

$$\tau_{SRH}(\Delta n, n_0, p_0) = \frac{\Delta n}{U(\Delta n, n_0, p_0)} \tag{1-21}$$

Therefore, if the non-equilibrium densities are replaced by $n=n_0+n$ and $p=p_0+p$, the SRH lifetime can be expressed as:

$$\tau_{SRH} = \frac{\tau_{n0}(p_0 + p_1 + \Delta n) + \tau_{p0}(n_0 + n_1 + \Delta n)}{p_0 + n_0 + \Delta n} \qquad (1\text{-}22)$$

where τ_{n0} and τ_{p0} are the capture time constants of electrons and holes which are related to the thermal velocity v_{th}, the defect concentration N_t, and the capture cross-sections σ_n and σ_p of the specific defect center.

$$\tau_{p0} = (N_t \sigma_p v_{th})^{-1} \qquad (1\text{-}23)$$

$$\tau_{n0} = (N_t \sigma_n v_{th})^{-1} \qquad (1\text{-}24)$$
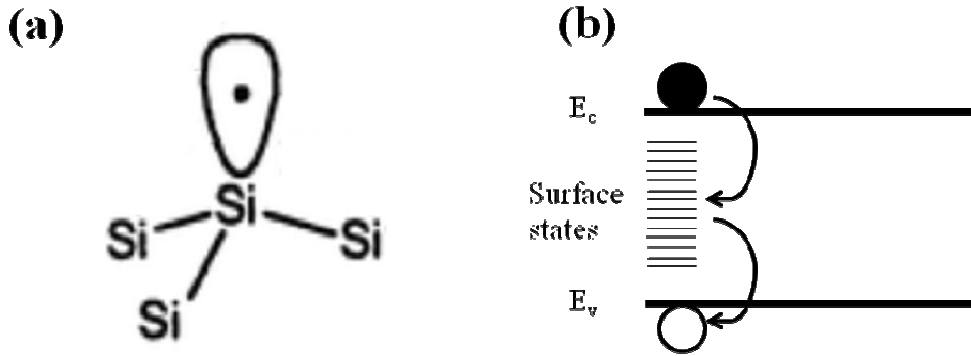
Fig. 1-11. Dangling bond in Si (a), and recombination through surface states (b).

Surface recombination is a special case of the SRH recombination. The surface is a discontinuity in the crystalline structure of a material. Dangling bonds, shown in Fig. 1-11a, are produced when Si atoms are partially bonded. Dangling bonds produce defect energy states in the band-gap energy. Unlike the bulk SRH defect states, the

19

surface defect states are continuously distributed along the band-gap (Fig. 1-11b). Therefore, the interface trap density $D_{it}(E_t)$ and the capture cross-sections $\sigma_n(E_t)$ and $\sigma_p(E_t)$ are energy dependent quantities. While the recombination rate of any single surface state can be expressed by eq. 1-20, the total surface recombination rate U_s can be determined by integrating the expression over the entire band-gap:

$$U_s = (n_s p_s - n_i^2) \times \int_{E_v}^{E_c} \frac{v_{th} D_{it}(E_t) dE_t}{[n_s + n_1(E_t)\sigma_p^{-1}(E_t) + [p_s + p_1(E_t)]\sigma_n^{-1}(E_t)}$$

(1-25)

The surface recombination velocity S (SRV) is defined as:

$$S \equiv \frac{U_s}{\Delta n}$$

(1-26)

S can then be expressed as a function of n_s, n_0 and p_0.

$$S(\Delta n_s, n_0, p_0) \equiv \frac{U_s(\Delta n_s, n_0, p_0)}{\Delta n_s}$$

$$= \int_{E_v}^{E_c} \frac{(n_0 + p_0 + \Delta n_s)v_{th}D_{it}}{[n_0 + n_1 + \Delta n_s]\sigma_p^{-1} + [p_0 + p_1 + \Delta n_s]\sigma_n^{-1}} dE$$

(1-27)

All the recombination mechanisms may occur simultaneously in a given sample. Therefore, the overall recombination rate is just the summation of the individual recombination rates. The effective lifetime, τ_{eff}, of a sample is then given by:

$$\frac{1}{\tau_{eff}} = \left(\frac{1}{\tau_{SRH}} + \frac{1}{\tau_{Auger}} + \frac{1}{\tau_{rad}} \right) + \frac{1}{\tau_{surface}} = \frac{1}{\tau_{bulk}} + \frac{1}{\tau_{surface}} \quad (1\text{-}28)$$

1-2-3 High efficiency single crystalline Si solar cell - The PERL solar cell

The highest efficiency single crystalline Si solar cell ever produced is the passivated emitter, rear locally-diffused (PERL) cell structure having an efficiency of 24.7% [17]. Fig. 1-12 shows the structure of the PERL solar cell. The PERL solar cell has an inverted pyramid structure with double-layered anti-reflection coating, well-passivated front and rear cell regions, and heavy doping at the front and rear metal contacts. The PERL structure was able to obtain a very high open circuit voltage, i.e., 0.706 V, photocurrent density, i.e., 42.2 mA/cm^2 and fill factor of 0.828.
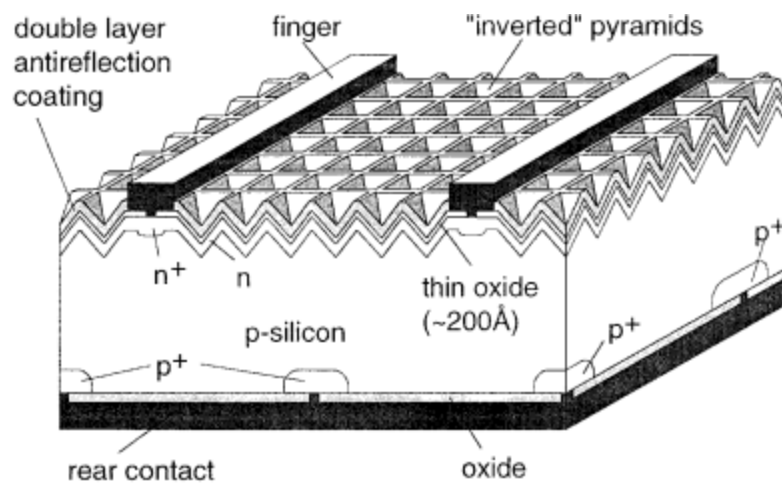
Fig. 1-12. The passivated emitter, rear locally-diffused (PERL) solar cell structure.

1-3   Purpose of this Study

In the previous sections, solar cells were introduced as alternative energy sources to reduce carbon dioxide emissions from burning of fossil fuels. However, the current solar cell technology and high production costs are still far from being the ideal alternative energy sources for supplying the world energy demand. Therefore, the main purpose of this work is to provide a new method, i.e., the "surface structure chemical transfer method" (SSCT), on how to improve the Si solar cell characteristics, i.e., high photocurrent density, for more efficient Si solar cell devices while providing a fast, i.e., ~30 s, and simple, i.e., room temperature, solar cell processing for more cost-effective device production.

This work on solar cells will greatly benefit the development of better solar cell technology and for the reduction of production costs. In the following chapters, a fast and simple method to produce ultra-low reflectivity Si surfaces will be introduced. Solar cells were then fabricated from the ultra-low reflectivity surfaces, and results showed great improvement in the solar cell characteristics. The HF-treatment for Si wafers will also be discussed and some proposals for better Si wafer processing will be provided.

However, this work will not only benefit the applications point of view, but also, for the enrichment of science. Nanocrystalline Si is a very promising material with many exciting properties, some of which will be discussed in this work, i.e., photoluminescence, structure, etc. Some chemical mechanisms will also be discussed, i.e., chemical-electrochemical reaction of a Pt metal with Si in $HF:H_2O_2$, phosphorus

dopant diffusion in a nanocrystalline Si/Si structure, and the initial oxidation of a H-terminated Si surface.

An outline of the following chapters is provided below.

Chapter 2 introduces the chemical methods performed in this thesis, i.e., RCA clean method and saw damage removal by KOH. Also, the instruments and analytical tools used were all introduced, i.e., microwave photoconductive decay method, X-ray photoelectron spectroscopy, Kelvin probe method, reflectance spectroscopy, photoluminescence spectroscopy, scanning electron microscopy, transmission electron microscopy, and solar simulation.

Chapter 3 introduces the surface structure chemical transfer method (SSCT) for the production ultra-low reflectivity Si surfaces. The morphology and structure of the nanocrystalline Si surface were studied and mechanisms for the nanocrystalline formation and ultra-low reflectivity were proposed. The photoluminescence of the Si nanocrystals were measured and was used to explain the observed increase in the minority carrier lifetime.

Chapter 4 introduces the solar cell production and pn-junction formation processes. The conditions for the nanocrystalline Si/Si structured pn-junction were studied, and changes in some properties before and after the pn-junction formation were observed. Finally, the solar cell with the best solar cell characteristics was discussed.

Chapter 5 shows changes of surface properties of HF-treated Si wafers caused by air exposure. The changes in minority carrier lifetime based on the humidity conditions of air were shown. The chemical species involved during the oxidation in air were determined by XPS and work function measurements.

Chapter 6 summarizes all the results and general discussions were presented.

References

[1]   Intergovernmental Panel on Climate Change. *IPCC Special Report on Renewable Energy Sources and Climate Change Mitigation.* Cambridge University Press, Cambridge, United Kingdom and New York, NY, USA, (2011).

[2]   D. Lashof and D. Ahuja, Nature **344** 529 (1990)

[3]   R. Rapier. (2012). *Global Carbon Dioxide Emissions.* Retrieved from http://www.energytrendsinsider.com/2012/07/02/global-carbon-dioxide-emissions-facts-and-figures/

[4]   U.S. Energy Information Administration. (2011). *International Energy Outlook 2011 (DOE/EIA-0484).* Retrieved from http://www.http://www.eia.gov/forecasts/ieo/pdf/0484(2011).pdf

[5]   J. Carabe and J. Gandia, *Optoelectronics Review*, **12** 1 (2004)

[6]   P. Wurfel, *Physics of Solar Cells 2nd ed.* (Wiley-VCH) (2009)

[7]   J. Nelson, *The Physics of Solar Cells* (Imperial College Press) (2004)

[8]   A. R. Jha, *Solar Cell Technology and Applications* (CRC) (2010)

[9]   W. Shockley and H. Queisser, *J. Appl. Phys.* **32** 510 (1961)

[10]   G.L. Pearson and J. Bardeen, *Phys. Rev.* **75** 865 (1949)

[11]   H. R. Philipp and E.A. Taft, *Phys. Rev.* **120** 37 (1960)

[12]   H. Seidel, L. Csepregi, A. Heuberger, and H. Baumgartel, *J. Electrochem. Soc.* **137** 3612 (1990)

[13]   A.D. Wilson, *Solar Energy Materials* **10** 9 (1984)

[14]   J.G. Fossum, F.A. Lindholm, M.A. Shibib, Electron Devices, IEEE Transactions

on **26** 1294 (1979)

[15] S.M. Hu, *J. Electrochem. Soc*. **113** 693 (1966)

[16] S. Rein, *Lifetime Spectroscopy: A Method of Defect Characterization in Silicon for Photovoltaic Applications* (Springer) (2005)

[17] M.A. Green, J. Zhao, A. Wang, S.R. Wenham, *Electron Devices, IEEE Transactions on* **46** 1940 (1999)

[18] W. Shockley, W.T. Read, Statistics of the Recombinations of Holes and Electrons *Phys. Rev*. **87** 835 (1952)

Chapter II

Experimental Methods: Chemical Methods; and Instrumentation and Analysis

2-1   Chemical Methods

2-1-1 The RCA clean method

Metal and organic contaminants accumulated at the surface of Si wafers during / or after processing have to be removed prior to subsequent high temperature processing steps, i.e., oxidation, diffusion, etc., in order to produce semiconductor devices of high performance and reliability. The RCA clean method was developed by Werner Kern during 1965 [1] while working for the Radio Corporation of America, hence the name RCA.

Fig. 2-1 shows the summary of the RCA clean process. The RCA clean process is divided into two steps, with ultrapure water rinsing between each steps: (1) APM (Ammonium hydroxide – hydrogen Peroxide Mixture), which is the removal of insoluble organic contaminants and particle contaminants in 1:1:5 $NH_4OH:H_2O_2:H_2O$ solution at temperatures between 70 and 80°C for 10 min; (2) HPM (Hydrochloric acid – hydrogen Peroxide Mixture), which is the removal of ionic and heavy metal contaminants in 1:1:5 $HCl:H_2O_2:H_2O$ solution at temperatures between 80 and 90°C for 10 min. These two steps are followed by HF-etching oxide strip, which is the removal of the thin oxide layer that contains the metal contaminants as a result of APM and HPM using a diluted HF (0.5%) solution at room temperature for 2 min.

The first step was designed to remove organic surface films by oxidative breakdown and dissolution to expose the silicon or oxide surface for concurrent or subsequent decontamination reactions. Hydrogen peroxide solutions at high pH are effective for organic contaminant removal by oxidation. Also, the hydroxide ions attack

the native oxide layer consequently etching the oxide layer. The bare Si surface is then oxidized by hydrogen peroxide. Due to this, a rough surface is then formed after the cleaning step. Metal contaminants may also removed by forming an ammonium hydroxide complex, e.g., $Cu(NH_3)_4^{+2}$ amino-complex for Cu contaminants. However, metal contaminants may also form NH_4OH-insoluble hydroxides in basic solutions [2]. The second step is then designed to remove the remaining metal contaminants by forming water soluble complexes at low *pH* values. At low *pH*, protonation of the surface is favoured, forcing the removal of the metal ions adsorbed on the surface.
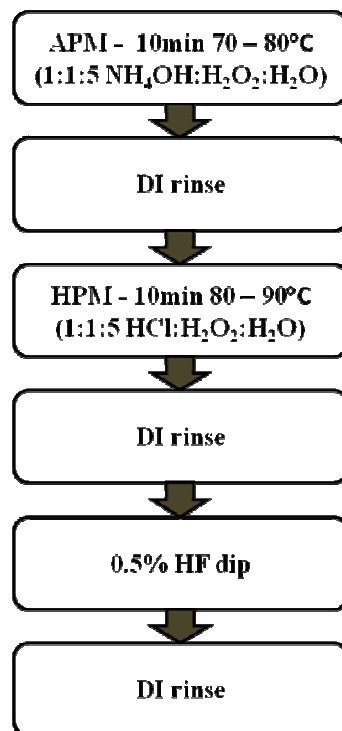
Fig. 2-1. The RCA clean process

However, considering the conditions and mechanism of the RCA cleaning method, the disadvantages of this method are: 1) high concentration of solutions, i.e., 2~3%, 2) re-adsorption of metal impurities, 3) elevated temperature, i.e., 50~80%, and 4) Si etching which results in roughening of surface, i.e., formation of defects.

In this thesis, Si wafers were treated with the RCA clean process prior to any subsequent chemical processes.

2-1-2 Alkaline etching of Si

Alkaline etching of Si by KOH is normally used in solar cell processing for the fast removal of saw damage from as-sliced Si ingots and/or formation of a mat-textured surface for low reflectivity surfaces [3].

The saw damage removal is done in a 21% (w/w) KOH solution at 80°C for about 10 min. The etch rate for this condition in a Si(100) wafer was determined to be about 1 μm/min. This condition will approximately etch about 10 μm of Si which is well above the typical saw damage layer height of about a few microns for as-sliced Si wafers [4].

Fig. 2-2 shows the SEM micrograph of a polycrystalline Si surface before and after saw damage removal by KOH etching. In Fig. 2-2a, the rough surface caused by the wire saw damage can be observed. However, after KOH etching, the saw damage was removed, revealing the polycrystalline surface.
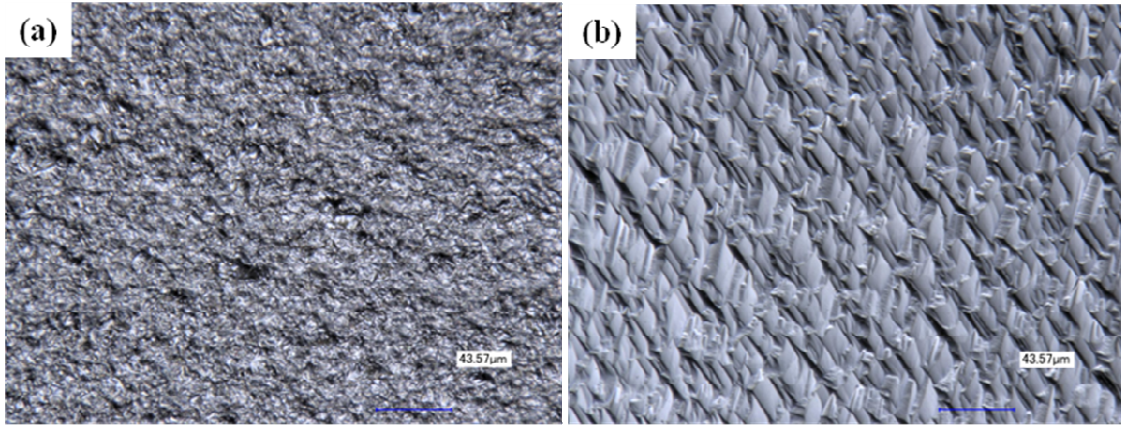
Fig. 2-2. SEM micrograph of a polycrystalline Si surface before (a) and after (b) saw damage removal by KOH etching.

The chemical reaction involved in KOH etching of Si is shown in (2-1) [3].

$$Si + 2(OH)^- + 4H_2O \rightarrow Si(OH)_6^{2-} + 2H_2 \qquad (2\text{-}1)$$
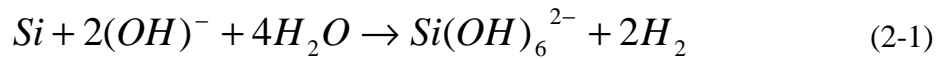
Si is attacked by hydroxide ions in the presence of water and results in a water soluble Si-hydroxide complex. It was previously determined that the reaction also yields hydrogen gas as a by-product in a stoichiometric ratio of 2 H_2/Si [3].

Due to the high etching rate at high temperatures and high KOH concentrations, non-isotropic etching occurs, therefore, saw damage removal is possible even for polycrystalline Si wafers. However, at low temperatures and low KOH concentrations, the reaction slows down resulting in a more pronounced etch anisotropy which is highly dependent upon the surface orientation.
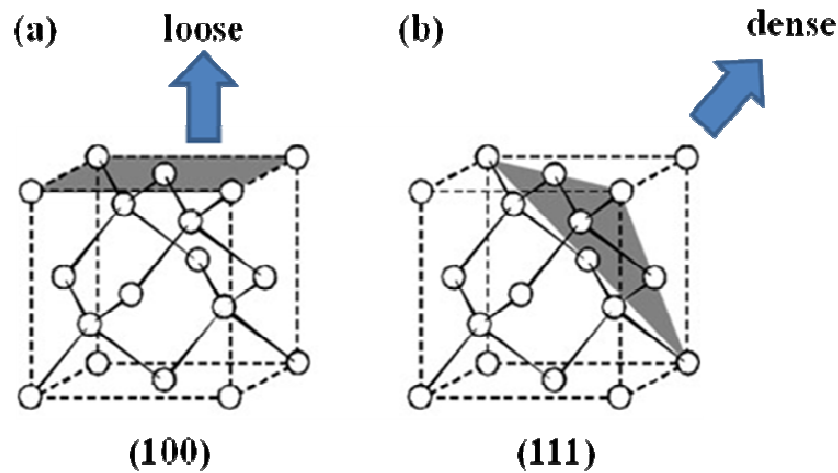
Fig. 2-3. Si crystal structure showing the (100) (a) and (111) (b) surfaces.

Fig. 2-3 shows the Si crystal structure along with the (100) and (111) surfaces. It can be observed that the (100) surface is more loosely packed and has two dangling bonds per atom as compared to a (111) surface which is the most closely packed and has only one dangling bond per atom. For this reason, the etching rate of a (100) surface is faster as compared to a (111) surface which has the lowest etching rate.

For Si(100), the anisotropy for low KOH concentrations can be taken advantage to produce a pyramidal-textured (Fig. 2-4a) surface having a pyramidal structure with (111) surface. However, for a polycrystalline Si wafer, having random surface orientations with only a part of (100) oriented regions, alkaline etching cannot be form uniform pyramidal structure. For this case, a polycrystalline (Fig. 2-4b) textured surface is formed by acid etching [5] as shown in 2-2 to 2-5. The HF:HNO$_3$ solution attacks Si isotropically, therefore, a textured surface can be formed regardless of the surface crystal orientation. The general mechanism is as follows:

$$HNO_2 + HNO_3 \rightarrow 2NO_2 + H_2O \qquad \text{(2-2)}$$

$$2NO_2 + Si \rightarrow Si^{2+} + 2NO_2^{-} \qquad \text{(2-3)}$$

$$Si^{2+} + 2(OH)^{-} \rightarrow SiO_2 + H_2 \qquad \text{(2-4)}$$

$$SiO_2 + 6HF \rightarrow H_2SiF_6 + 2H_2O \qquad \text{(2-5)}$$
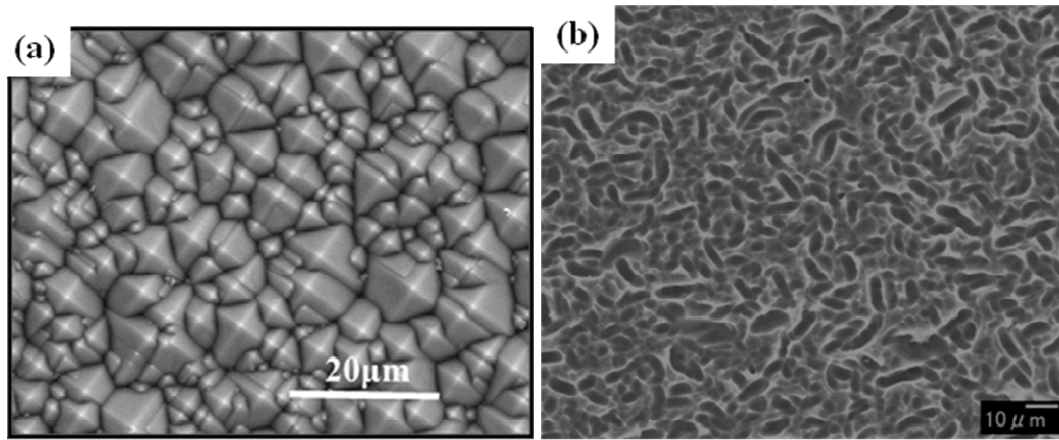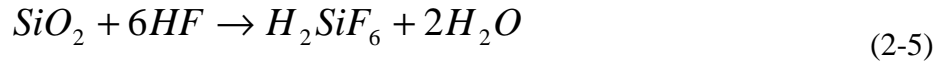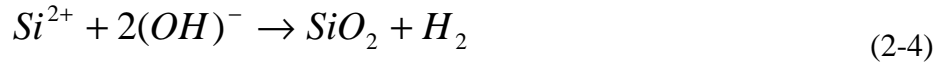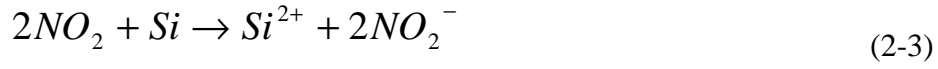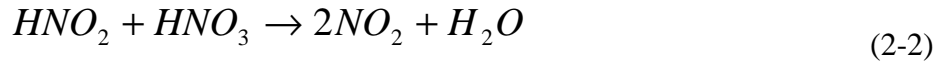
Fig. 2-4. A pyramidal-textured Si surface produced by alkaline etching from a Si(100) wafer (a) and a textured polycrystalline Si wafer produced by acid etching (b).

In this thesis, the reflectivities of the textured surfaces by alkaline etching and acid etching were compared with a nanocrystalline Si surface and their corresponding light absorption mechanisms (Chapter 3).

2-2   Instrumentation and analysis

2-2-1 Minority carrier lifetime measurements – Microwave Photoconductive Decay (MW-PCD) spectroscopy

The minority carrier lifetime is a very important parameter for the production of high efficiency solar cells, especially the open-circuit photovoltage, i.e., V_{oc}. The minority carrier lifetime determines the rate of recombination of excess carriers in a solar cell. Therefore, it can determine the quality of a solar cell and its impact in the solar cell performance.
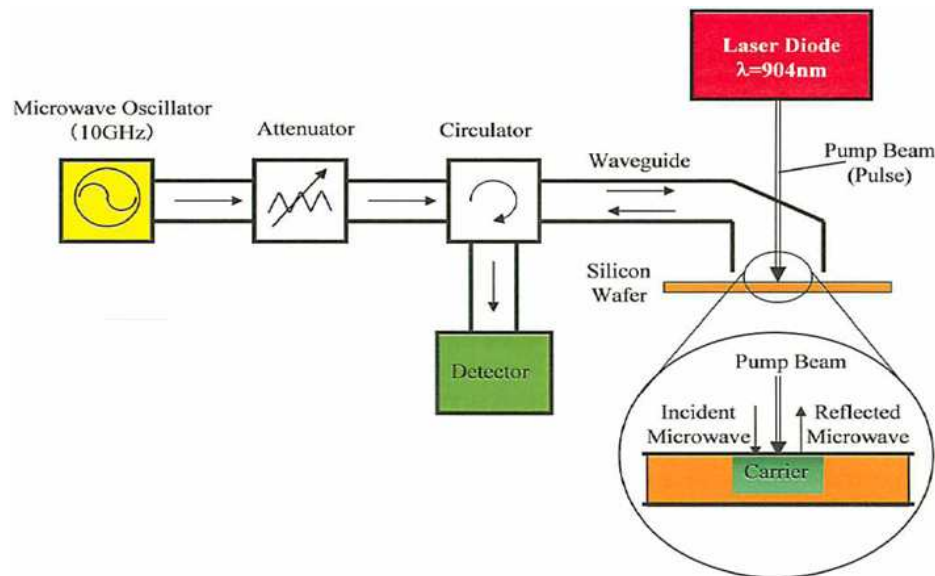
Fig. 2-5. Schematic of the Microwave Photoconductance Decay (MW-PCD) system used for minority carrier lifetime measurements.

The minority carrier lifetime measurement technique used in this thesis is the microwave photoconductive decay (MW-PCD) spectroscopy [6]. A schematic of the MW-PCD minority carrier lifetime measurement is shown in Fig. 2-5. The MW-PCD technique is a transient technique, wherein, the carrier lifetime is determined from the asymptotic decay of the average excess carrier density after the pulse excitation by the laser diode. The excess carrier decay is monitored via changes in the sample's photoconductance, measured by the sample's microwave reflectance.
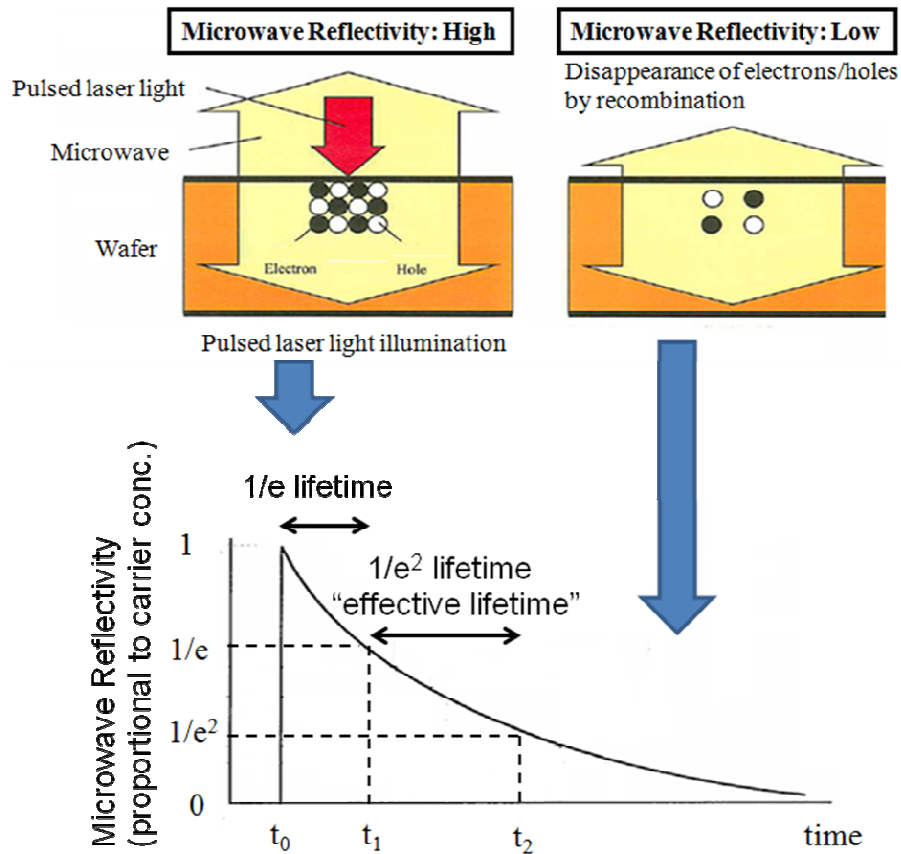
Fig. 2-6. Principle of minority carrier lifetime measurement by Microwave Photoconductance Decay (MW-PCD) spectroscopy
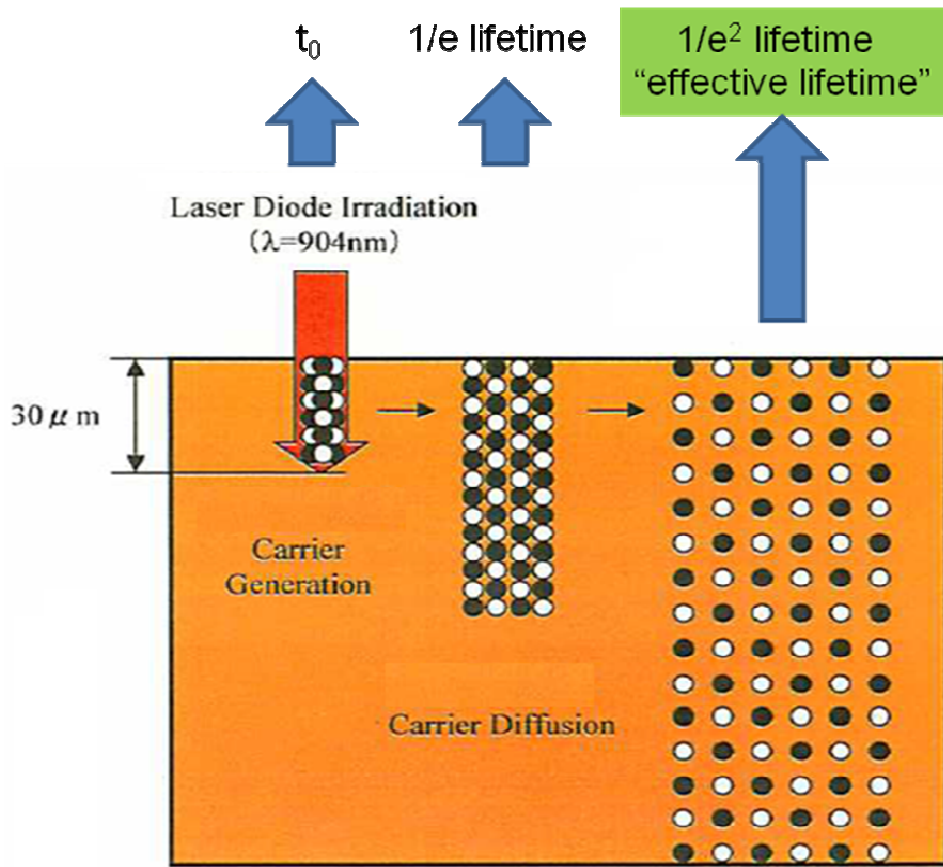
Fig. 2-7. The carrier generation, diffusion and the effective lifetime in MW-PCD.

In Fig. 2-6, the principle of MW-PCD is shown. At t_0, excess carriers are produced immediately after the laser pulse, which results in an increase in microwave reflectivity due to the very high photoconductance of the sample. The microwave reflectivity is normalized according to the photoconductance after the laser pulse at $t = 0$. After which, the excess carriers start recombining which results in the decay curve shown in Fig. 2-6. The 1/e lifetime, i.e., time from t_0 to t_1, corresponds to the initial portion of the decay curve, i.e., the time carriers diffuse in the sample (Fig. 2-7), and is

mainly dominated by surface recombinations. The $1/e^2$ lifetime, time from t_1 to t_2, corresponds to the exponential portion of the decay curve in Fig. 2-6. The $1/e^2$ lifetime is the time when the excess carriers are homogeneously distributed in the sample (Fig. 2-7), also called the effective lifetime [7] which is a function of both surface and bulk recombinations. The minority carrier lifetime values used in this thesis are the $1/e^2$, i.e., effective lifetime.

In this thesis, minority carrier lifetime measurements were done for the nanocrystalline Si surface (Chapter 3), and HF-treated Si wafers (Chapter 5). Minority carrier lifetime of the Si wafers were determined from measurements of microwave reflectivity decay caused by 904 nm wavelength incident light with a carrier injection density of $1\times10^{15}/cm^3$ using a KOBELCO Wafer LTA-1510 system.

2-2-2 Electron Spectroscopy for Chemical Analysis (ESCA) – X-ray Photoelectron Spectroscopy (XPS)

When the surface of a material is irradiated with photons of energy $h\nu$, electrons were observed to be emitted from the surface of the material provided the photon energy is greater than the work-function of the material. This phenomenon, later called the "photoelectric effect" (Fig. 2-8) was first observed by H. Hertz in 1887 [8] and was later explained by A. Einstein in 1905, wherein, he won the Noble Prize in Physics (1921) [9]. XPS was later developed by K. Siegbahn, and was called the Electron Spectroscopy for Chemical Analysis (ESCA) [10]. ESCA is one of the most versatile techniques for the chemical and electronic analysis of surfaces.
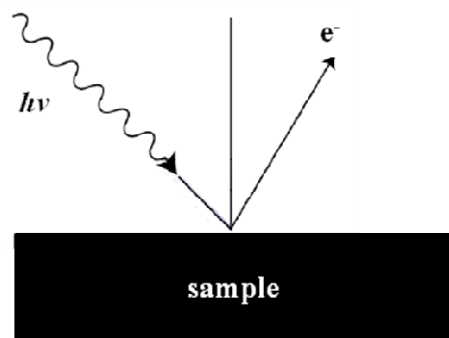
Fig. 2-8. The photoelectric effect.

Fig. 2-9 shows the energetics of XPS [10]. A monochromatic beam of X-rays is incident upon the sample which causes the photoemission of electrons from both the core and valence levels of surface atoms into the vacuum. The core level electrons do not participate in chemical bonding and are located in the inner quantum shells, while the valence electrons are the electrons that participate in chemical bonding which are weakly bound and located in the outer quantum shells. The core electrons are mostly insensitive to the outer surroundings, therefore, can be used to determine the signature binding energies, E_b, for elemental indentification. The binding energy is defined as the energy of the core level with respect to the highest occupied level (E_F) of the sample. The vacuum level is the energy at which an electron will have zero kinetic energy at an infinite distance from the surface. A plot of the number of electrons, $N(E)$, having a certain kinetic energy, E_k, is also shown in Fig. 2-9.
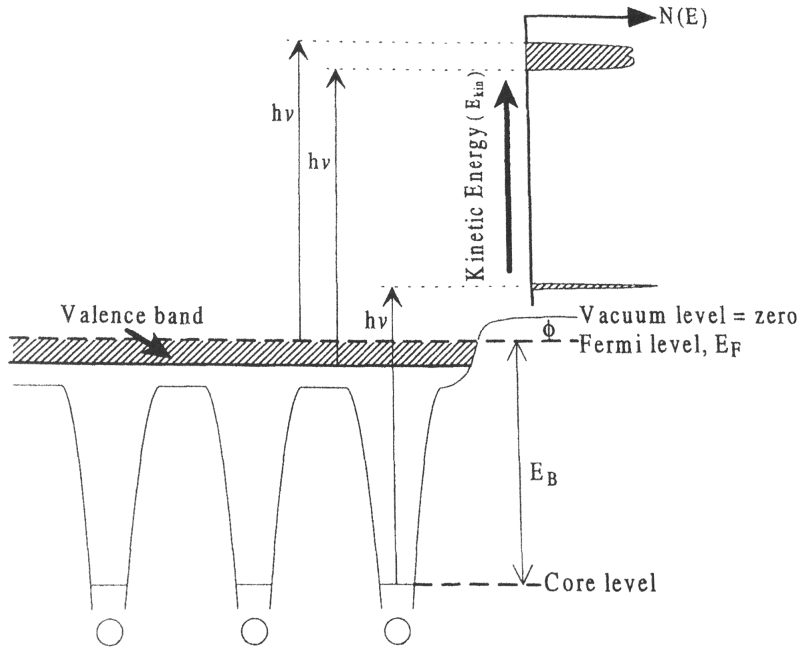
Fig. 2-9. The energetics of X-ray Photoelectron Spectroscopy (XPS).

The kinetic energy of emitted electrons, E_k, is given by the equation (2-6):

$$E_k = h\nu - E_b - \phi_{sp} \qquad (2\text{-}6)$$

where $h\nu$ is the energy of the incident photon, E_b is the binding energy of the electron emitted from the sample, and φ_{sp} is the spectrometer work-function. The binding energy, E_b, can be calculated once the kinetic energy, E_k, is measured. Since the binding energy, E_b, is highly dependent on the chemical state of the atom, it can be used for the determination of important chemical information regarding the sample, i.e., elemental identification, chemical composition, etc [9]. In this thesis, the chemical states were obtained by determining the binding energy shift of the peaks. A higher binding energy

shift means a more positively charged state, while a lower binding energy shift means a less positively charged state.

XPS was also used to approximate the thickness, d_{ox}, of the SiO$_2$ layer on Si by using the equation [11]:

$$d_{ox} = \lambda_{ox} \ln \left[\frac{I_{ox}}{I_{Si}} \cdot \frac{I_{Si}^{\alpha}}{I_{ox}^{\alpha}} + 1 \right]$$

(2-7)

where I_{ox} and I_{Si} are the intensities of the SiO$_2$ and Si core level peaks, respectively. And

$$I_{Si}^{\alpha} = D_{Si} \sigma_{Si} \lambda_{Si}$$

(2-8)

$$I_{ox}^{\alpha} = D_{ox} \sigma_{ox} \lambda_{ox}$$

(2-9)

where λ is the mean free path of the photoelectrons, D is the atomic density, σ is the photoionization cross section and the subscripts ox and Si correspond to the value for the SiO$_2$ and Si, respectively.

In this thesis, XPS was used to determine the chemical species present in the HF-treated Si wafers and the thickness of the SiO$_2$ layer formed (Chapter 5). XPS measurements were carried out using a VG Scientific ESCALAB 220i-XL spectrometer with a monochromatic Al Kα radiation source. Photoelectrons were detected in the surface-normal direction.

2-2-3 Workfunction measurements – Kelvin Probe (KP) analysis

The Kelvin method is a technique used to measure changes in work-function of metals, semiconductors, etc., by the use of a vibrating capacitor. W.A. Zisman used an idea by Professor Knoble in 1932 [12], to utilize a constantly vibrating reference probe for work-function measurements.

The KP method is a non-contact, non-destructive measurement for the determination of work-function changes. The KP used for the work-function measurements as shown in Fig. 2-10 consists of both a sample and a vibrating reference electrode in a parallel-plate configuration. The probe tip is normally connected to the preamplifier, while the sample is connected to the ground. The sample and KP tip are then electrically connected via an external "backing" potential (Vb).
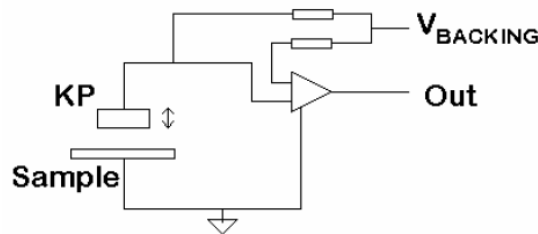
Fig. 2-10.   Kelvin Probe (KP) configuration used in the work function measurements.

As shown in Fig. 2-11a, when the KP tip and sample are in close proximity but not electrically connected, the Fermi levels (E_F) align at the vacuum level (E_{vac}) depending on their respective work-functions (φ). When the KP tip and the sample are

then made electrically connected as shown in Fig. 2-11b, the electrons flow from the material with a smaller work-function to the material with a larger work function. The material with the lower work-function then becomes positively charged while the material with a higher work-function becomes negatively charged. Surface charges completely disappear when the electric field is able to compensate for the work-function difference. In Fig. 2-11c, a backing potential (V_b) is applied until the charges becomes zero, at this time, the backing potential is exactly the same value as the contact potential difference (V_{CPD}) but of opposite sign, i.e, . $V_b = -V_{CPD}$.
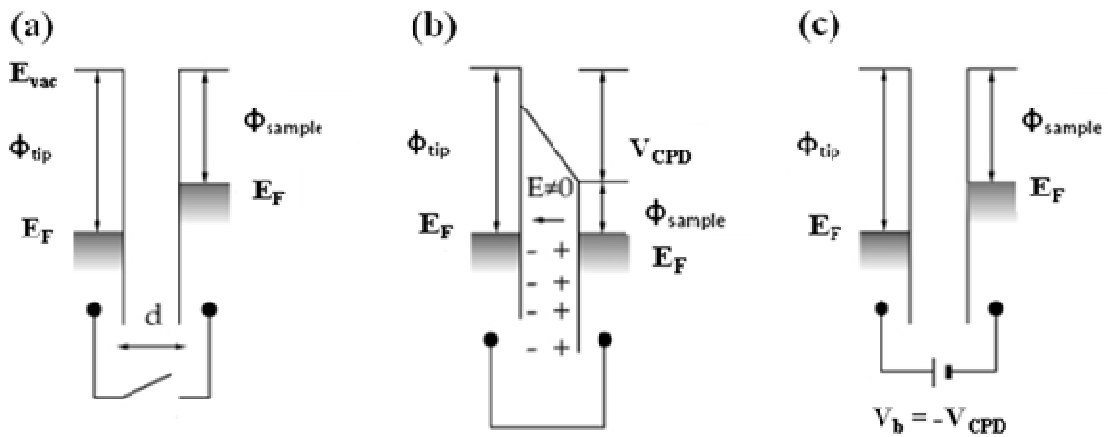
Fig. 2-11. Determination of the contact potential difference of the sample (V_{CPD}) by a backing potential (V_b). When the KP tip and sample are not electrically connected (a), electrically connected (b), and the V_b equals the $-V_{CPD}$ (c).

To determine the work function changes of samples used for this thesis, the work function of the probe tip was assumed to be constant during the whole measurement period. The probe tip was a 304 stain steel type with a robust and chemically stable

native oxide layer. The work-function changes ($\Delta\varphi$) in a sample can be calculated by equations 2-10 to 2-12:

$$V_{CPD(1)} = \phi_{tip} - \phi_{sample(1)} \tag{2-10}$$

$$V_{CPD(2)} = \phi_{tip} - \phi_{sample(2)} \tag{2-11}$$

$$\Delta\phi = V_{CPD(1)} - V_{CPD(2)} = \phi_{sample(2)} - \phi_{sample(1)} \tag{2-12}$$

In this thesis, work function measurements were taken for the HF-treated Si wafers (Chapter 5). Measurements of workfunction changes were performed by a contact potential difference method using a McAllister KP6500 Digital Kelvin Probe.

2-2-4 Reflectivity measurements

One of the most important techniques for the analysis of solar cells is the reflectivity measurements. Reflection occurs when light moves from a medium with one index of refraction into a second one with a different index of refraction. The reflection of light at the surface of solar cells is a key parameter affecting the conversion efficiency, wherein, the higher incident light intensity results in higher generated photocurrent. When a textured surface and/or an anti-reflection coating are used to enhance the performance of the solar cells, the reflectivity of the solar cell can be used to measure the quality of the textured surface and anti-reflection coating used. A Si sample is normally scanned in the wavelength range between 300 and 1100 nm, i.e, the wavelength range absorbed by silicon [13].

Fig. 2-12 shows the two types of surface reflections. In a specular reflection (2-12a), caused by a smooth surface, i.e., mirror, the incident angle of light is equal to the angle of reflection. In the diffuse reflection (2-12b), caused by a rough surface, the incident light is reflected at various angles. Therefore, in this thesis, an integrating sphere was used during the reflectivity measurements to accurately measure all the reflections occurring in the Si surface.
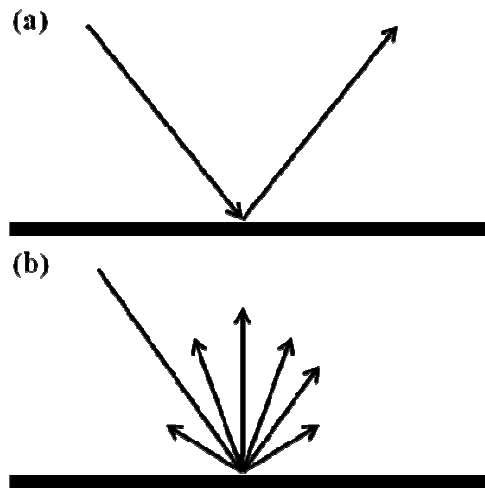
Fig. 2-12. Types of reflections: specular reflection – polished surface (a); diffuse reflection – rough surface (b).

Fig. 2-13 shows the set-up used for the reflectivity measurements. The integrating sphere rotates around the sample, and is able to record both reflection and transmission.

In this thesis, reflectivity measurements were carried out for the nanocrystalline Si surfaces (Chapter 3 and 4). Reflectivity spectra were recorded using a JASCO V-670

UV-Vis spectrometer attached to a JASCO automated absolute reflectance measurement ARMN-735 accessory.
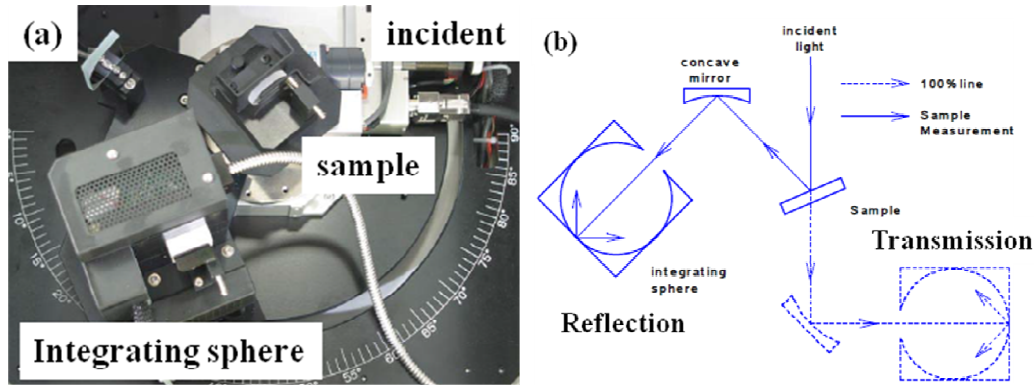
Fig. 2-13. Reflectivity measurement set-up apparatus (a) schematic (b)

2-2-5 Photoluminescence spectroscopy

Photoluminescence spectroscopy is a technique that can be used to determine the band-gap of a semiconductor [14]. Fig. 2-14 shows a summary of the photoluminescence process in semiconductors. The semiconductor material is irradiated with a photon of energy hv, which is greater than the band-gap of the semiconductor material. This result to an electron excited to the conduction band from the valence band. The excited electron relaxes to the lowest unoccupied orbital in the conduction band before recombining with a hole in the valence band. The electron-hole pair recombination emits a photon which has an energy corresponding to the band-gap of the semiconductor material [14]. Therefore, photoluminescence spectroscopy can be used to determine the band-gap of a semiconductor material. Photoluminescence

spectroscopy can also be used for the determination of defect states and other recombination mechanisms [15] present in the semiconductor sample since the defect state transitions may also involve radiative transitions.
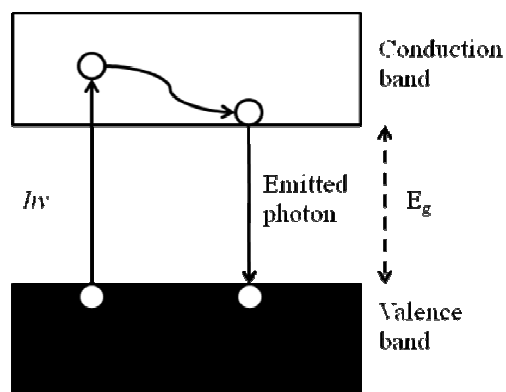
Fig. 2-14. A summary of the photoluminescence process in semiconductors.

In this thesis, photoluminescence spectroscopy was used to determine the band-gap widening of Si after the production of nanocrystalline Si (Chapter 3). Photoluminescence (PL) spectra were measured using a JASCO CT100GD grating spectrometer and a photomultiplier tube at room temperature. The excitation light source was a 325 nm He-Cd laser.

2-2-6 Electron Microscopy (EM) – Scanning Electron Microscopy (SEM) and Transmission Electron Microscopy (TEM)

In 1930's, the limit in optical microscopes, which could magnify specimens only up to x500 or x1000 and a resolution of 0.2 μm, had been reached. However, higher

magnifications of around x10K was needed to see the finer details in organic cell structures, i.e., mitochondria, nucleus, etc. The Transmission Electron Microscope (TEM), the first type of Electron Microscope (EM) was developed in 1931 by Max Knoll and Ernst Ruska, which was modeled exactly like that of a optical microscope except that instead of using light, a focused beam of electrons was used. The first Scanning Electron Microscope (SEM) was introduced in 1942, while the first commercial SEMs were released in 1965.
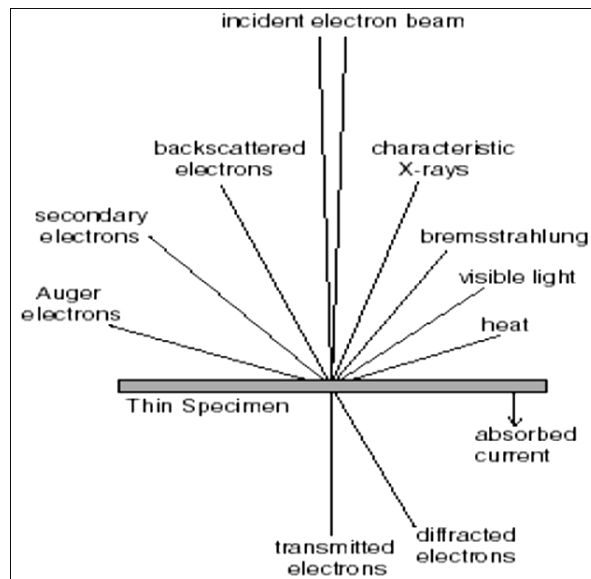
Fig. 2-15. Different effects produced by bombardment of a material with electrons.

Electron microscopes work very much like optical microscopes, however instead of light, electron beams are irradiated on the sample to gain information, i.e., structure, composition, etc. Electrons microscopes work as follows: (1) electrons are produced in an electron gun at high vacuum, (2) these electrons are then accelerated

towards the sample having a positive electrical potential, (3) the electrons hit the sample, and depending on the interaction with the sample, (4) electrons are detected and images are formed.

Fig. 2-15 shows the different possible interactions of incident electrons with a thin specimen. In SEM [17], the secondary and back-scattered electrons emitted from the surface by excitation of the primary beam are detected and converted to an image. Fig. 2-16 shows the schematic of a typical SEM set-up. Electrons are produced from an electron source, and these electrons are guided to the sample by the objective lens and scan coils. Once the primary electrons hit the sample, electrons in the specimen are excited and may undergo elastic and inelastic collisions until the electrons escape the surface, i.e., if the electrons still have sufficient energy. These electrons are called the secondary electrons and are collected in a photomultiplier which is then converted to images. However, electrons originating from the primary electrons can also be reflected back from the surface.   These high-energy electrons are called the back-scattered electrons.   Secondary and back-scattered electrons are distinguished from each other according to their energies. Secondary electrons are typically electrons emitted from the surface having energies less than 50 eV, while back-scattered electrons are electrons typically having energies greater than 50 eV. In SEM, electrons can penetrate a small depth on the surface, making it suitable for surface topography determination [18].

In this thesis, the surface structure of the nanocrystalline Si was determined by SEM (Chapter 3 and 4).   SEM micrographs were taken using a HITACHI S-2150 microscope with the incident electron energy of 20 keV, while, field emission scanning electron micrographs (FE-SEM) were measured using a JSM-6335F with the incident electron energy of 20 keV.
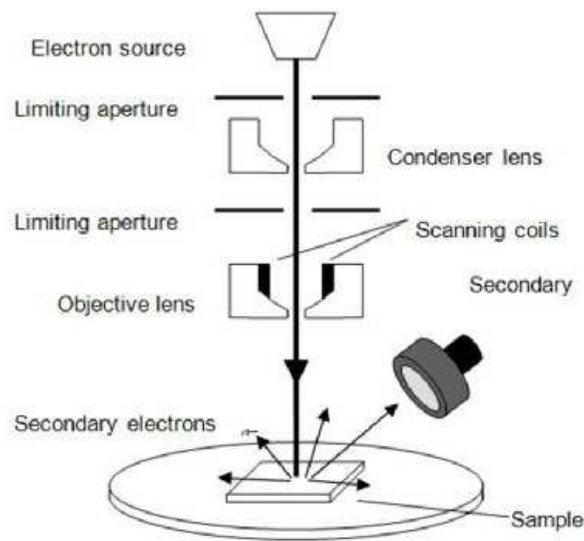
Fig. 2-16. Schematic of a typical Scanning Electron Microscope (SEM).

In TEM [16], unscattered and elastically scattered electrons are detected to form an image. Fig. 2-17 shows the schematic of a typical TEM set-up. As with the SEM, primary electrons are produced in an electron gun, and these electrons are guided to the thin specimen by the scan coils and objective lens. However, once the electrons hit the thin specimen, the electrons can pass through it without any interactions and these electrons are called the transmitted or unscattered electrons. The transmission of unscattered electrons is inversely proportional to the specimen thickness. Therefore, thicker areas in a specimen will appear to be darker while thin areas will appear lighter. Primary electrons hitting the sample may also be deflected by the atoms present in the thin specimen without any energy loss (elastic) and these electrons are called scattered electrons. After scattering, the electrons will then just be transmitted through the thin specimen. The primary electrons scattered by the same atomic spacing will also be

49

scattered at the same angle. Therefore, TEM can also determine information such as crystal orientation, atomic arrangements in addition to structural determination.

In this thesis, cross-sectional TEM was employed to determine the cross-sectional structure of the nanocrystalline Si surface (Chapter 3 and 4) and the crystal sizes (Chapter 3). TEM micrographs were taken using a JEOL EM-3000F microscope with the incident electron energy of 300 keV.
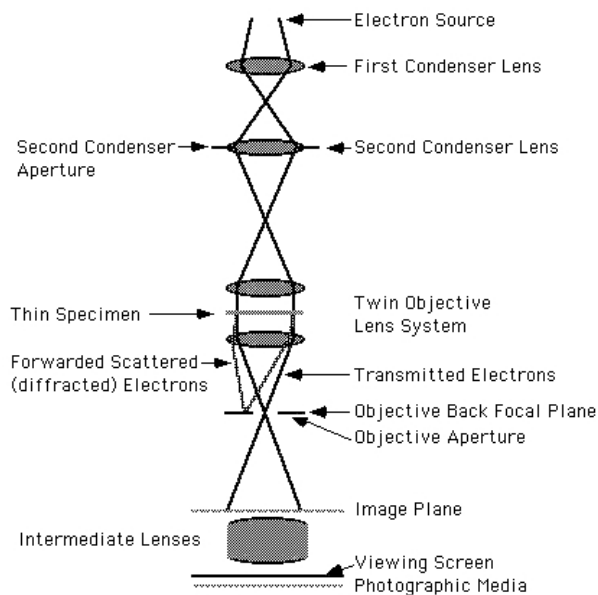
Fig. 2-17. Schematic of a typical Transmission Electron Microscope (TEM).

2-2-7 Solar simulator and current-voltage (I-V) measurements

After the production of solar cell devices, they are tested for its efficiency and other key solar cell parameters. A solar simulator provides an artificial solar energy

source to determine the efficiency and other key solar cell parameters of a solar cell. However, the solar spectrum varies by location, time of the day, season, etc. Therefore, a standard reference spectrum is needed in order to compare the performances of different solar cell devices.

The solar power density of the sun just outside the earth's atmosphere, referred to as air mass 0, AM0, has an integrated power density of 1353.1 W/m^2. However, when the sun light passes through the earth's atmosphere, the light is absorbed and scattered by the gases present in the atmosphere. In the infrared region, light is absorbed mainly by atmospheric water vapor (H_2O) and carbon dioxide (CO_2), while in the ultraviolet region, light is mainly absorbed by nitrogen (N_2), ozone (O_3) and oxygen (O_2) [20]. Therefore, the solar power density is reduced in the earth's surface. The air mass in the earth's surface is defined as (2-13):

$$ AM = \frac{1}{\cos\theta} \tag{2-13} $$

where θ is the angle from the surface normal. When the sun is directly overhead the earth's surface ($\theta = 0$), air mass = 1 (AM1). However, solar panels do not operate at AM1 due to the curvature of the earth's atmosphere. To approximate the earth's yearly average sunlight, and to provide a standard for solar cell measurements, $\theta = 48.2$ is used corresponding to AM1.5, and has an integrated power density of 1000 W/m^2.

Fig. 2-18 shows the standard solar spectrum vs. the solar simulator power density used for this thesis. The lamp used was a Xe short-arc lamp, due to its high intensity and having a spectral distribution close to sunlight. However, some emission

lines can be observed in the infrared regions, therefore, filters were also used to reduce the effects of the emission lines during the solar simulation measurements.
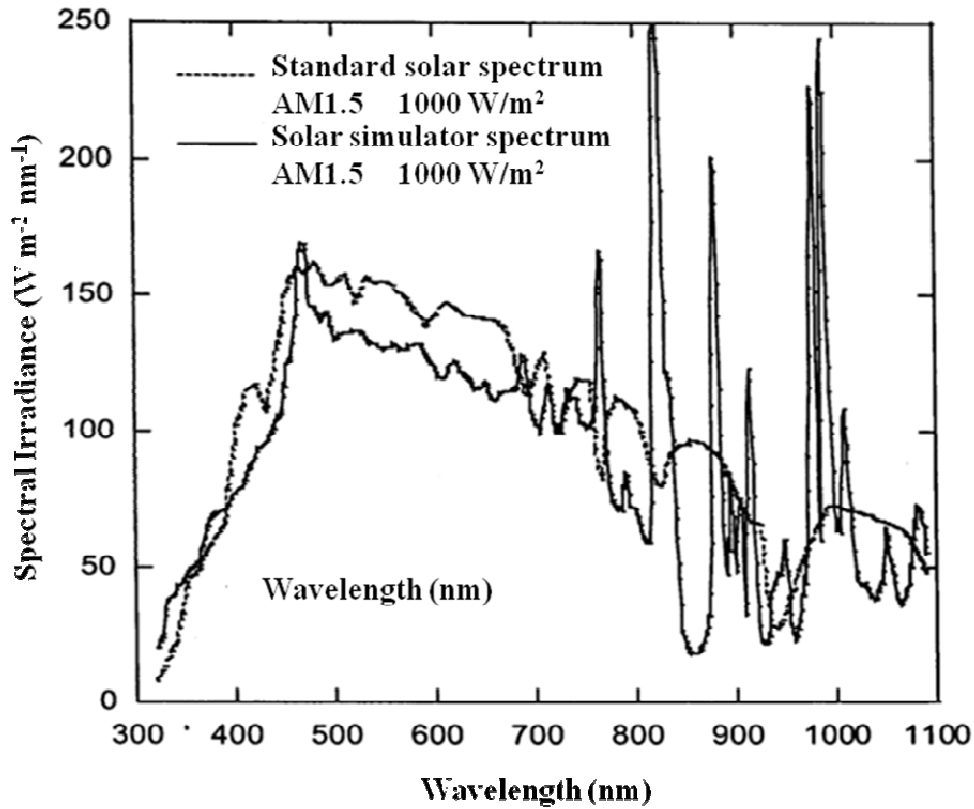
Fig. 2-18. Standard solar spectrum vs. the solar simulator power density used.

The schematic of the solar simulation measurements used for this thesis is shown in Fig. 2-19. The solar cell sample is irradiated with the light coming from the Xe short-arc lamp, while the applied voltage and current measurements were provided by the DC voltage/current source (ADVANTEST R6245). The intensity of the light was calibrated against a standard (1000 W/m^2) at the start of every measurement. The current-voltage measurements employed the four-point probe method, in which, the

voltage was applied between two probes while the current was measured by the other two probes.
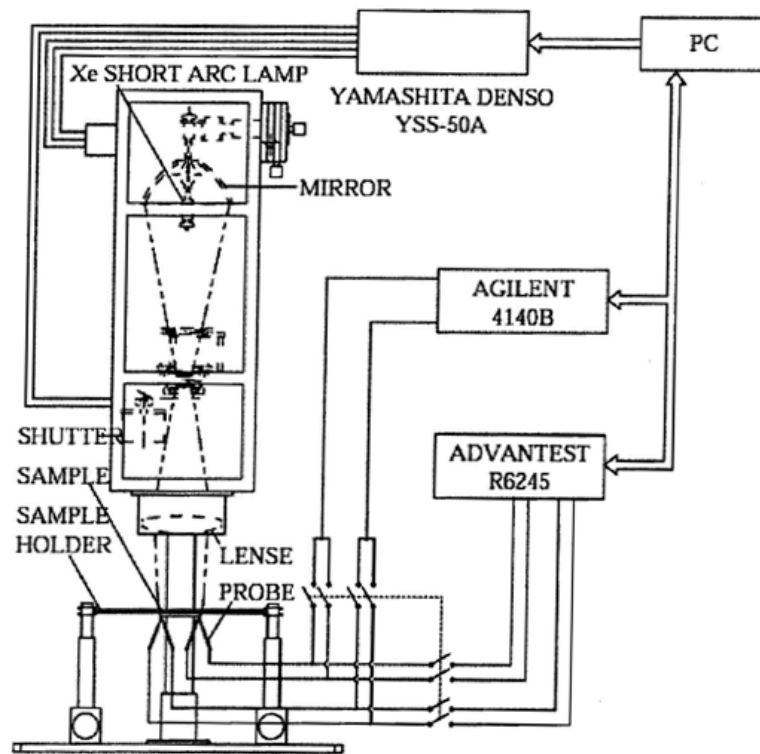
Figure 2-19. Schematic of the solar simulation measurements.

2-2-8 Calculation of the solar cell efficiency

A solar cell device behaves like a diode in the dark, i.e., a high density current flows only under forward bias ($V > 0$). For an ideal diode, the dark current density (J_{dark}) varies according to (2-14):

$$J_{dark} = J_o(e^{qV/k_BT)} - 1)$$

(2-14)

where J_o is the reverse saturation current, q is the electronic elementary charge, k_B is the boltzmann's constant and T is the temperature in K.

Under illumination, the total current density can be approximated as the sum of the dark current density and the photocurrent, J_{ph} (2-15).

$$J = J_{ph} - J_{dark}$$

(2-15)

This convention means that the photocurrent will have positive values as shown in Fig. 2-19a. Substituting (2-14) to (2-15) results to

$$J = J_{ph} - J_o(e^{qV/k_BT)} - 1)$$

(2-16)

When the contacts are isolated, the potential difference reaches its maximum value, called the open circuit voltage (V_{oc}).

$$V_{oc} = \frac{kT}{q} \ln\left(\frac{J_{ph}}{J_o} + 1\right)$$

(2-17)
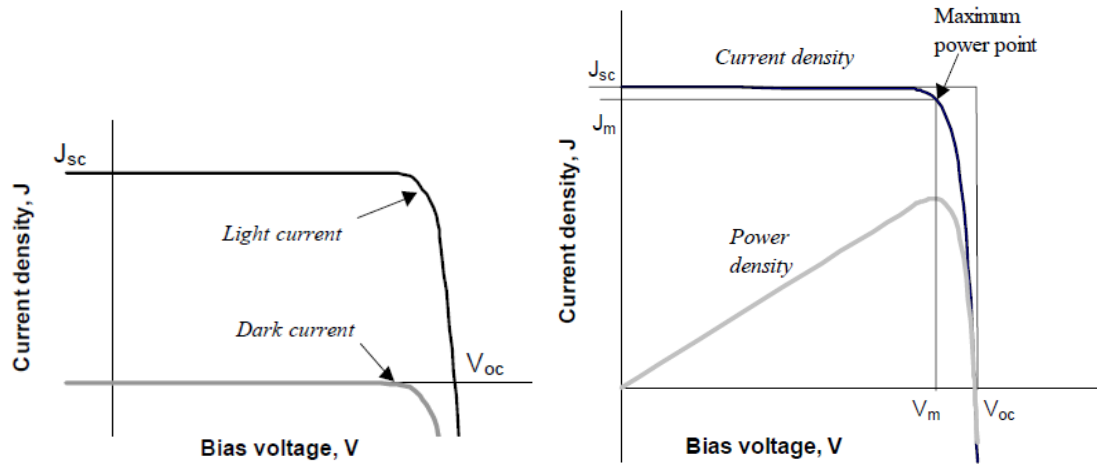
Fig. 2-20. Solar cell current-voltage curves showing the light and dark currents
(a) and the maximum power density (b).

The solar cell operates at forward bias, in the range between 0 and V_{oc}, where
the solar cell can deliver power. The incident photon power density, P is represented by

$$P = JV \qquad (2\text{-}18)$$

At a certain operating point, the solar cell has its maximum power density, which occurs
at some voltage (V_m) and current density (J_m) as shown in Fig. 2-20b. The fill factor
(*FF*) can then be calculated by (2-19)

$$FF = \frac{J_m V_m}{J_{sc} V_{oc}} \qquad (2\text{-}19)$$

The *FF* is the ratio of the maximum power density of the solar cell to the product of *Jsc* and *Voc*. The *FF* determines the "squareness" of the *J-V* curve as shown in Fig. 2-20b, i.e., the higher the area of the rectangle inside the *J-V* curve, the higher the *FF*.

The efficiency, η of the solar cell is the ratio of the maximum power density to the incident power density, P_{in}.

$$\eta = \frac{J_m V_m}{P_{in}} \tag{2-20}$$

Relating J_{sc}, V_{oc} and FF to η from (2-21).

$$\eta = \frac{J_{sc} V_{oc} FF}{P_{in}} \tag{2-21}$$

J_{sc}, V_{oc}, *FF* and η are the key solar cell parameters. In this thesis, these parameters will be defined together with the solar cell current-voltage curves.

However, in practical solar cells, the dark current does not obey the ideal diode equation (2-22). The non-ideal behavior is approximated by introducing an ideality factor, *n*, in the ideal diode equation. The ideality factor can be used to measure the recombinations in a solar cell. A high value of *n* mainly lowers *FF*.

$$J_{dark} = J_o(e^{qv/nk_BT}) - 1) \qquad (2\text{-}22)$$

The ideality factor, n, can be 1, corresponding to diffusion current or, 2, corresponding to recombination current. Fig. 2-21 shows the voltage dependence of the dark current. At lower voltages, the dark current is dominated by the recombination current, $n = 2$, while at higher voltages, the dark current is dominated by the diffusion current, $n = 1$. In Fig. 2-21, the recombination current is dominant at the voltage of the maximum power point. At V_{oc}, the diffusion current is the dominant current component.
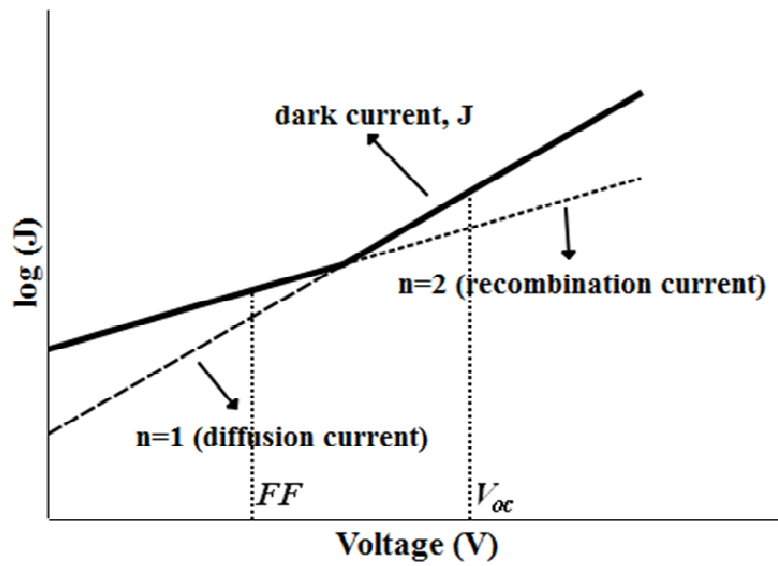
Fig. 2-21. Voltage dependence of the dark current for pn-junction.

References

[1]   W. Kern, and D. Puotinen, *RCA Rev*. **31** 187 (1970)

[2]   W. Kern, *J. Electrochem. Soc*. **137** 1887 (1990)

[3]   H. Seidel, L. Csepregi, A. Heuberger, and H. Baumgartel, *J. Electrochem. Soc*. **137** 3612 (1990)

[4]   E. Saccocio, and W. McKeown, *J. Appl. Phys*. **38** 2702 (1967)

[5]   H. Robbins, and B. Schwartz, *J. Electrochem. Soc*. **107** 108 (1960)

[6]   S. Rein, *Lifetime Spectroscopy: A Method of Defect Characterization in Silicon for Photovoltaic Applications* (Springer) (2005)

[7]   T. Pisarkiewicz, *Opto-Electronics Rev*. **12** 33 (2004)

[8]   A. Einstein, *Annalen der Physik* **17** 132 (1905)

[9]   T. Barr Modern ESCA: The principles and practice of X-ray photoelectron spectroscopy (CRC) (1994)

[10]   G. Attard, and Colin Barnes, Surfaces (Oxford Science Publications) (1998)

[11]   F. Himpsel, F. McFeely, A. Taleb0Ibrahimi, J. Yarmoff, and G. Holligner, *Phys Rev. B* **38** 6084 (1988)

[12]   W. A. Zisman, *Rev. Sci*. Instrum. **3** 367 (1932)

[13]   K. Rajkanan, R. Singh, and J. Shewchun, *Solid-State Electronics* **22** 793 (1979)

[14]   H. Nakashima, and Y. Shiraki, *Appl. Phys. Lett*. **33** 257 (1978)

[15]   H. Nakashima, and Y. Shiraki, *Appl. Phys. Lett*. **33** 545 (1978)

[16]   D. Williams, and C.B. Carter, *Transmission Electron Microscopy 2nd ed*. (Springer) (2009)

[17]   P. Echlin, *Handbook of Sample Preparation for Scanning Electron Microscopy*

and X-ray Microanalysis (Springer) (2009)

[18]   A. Angstrom, *Geografiska Annaler* **11** 156 (1929)

Chapter III

Ultra-low Reflectivity Si Surfaces Fabricated by Surface Structure Chemical Transfer Method

3-1　Introduction

For achievement of high efficiencies by crystalline Si solar cells, the formation of low reflectivity Si surfaces is indispensable. The conventional method to decrease the reflectivity of Si surfaces employs fabrication of mat-textured surfaces using anisotropic alkaline etching [1]. Strong alkaline solutions such as sodium hydroxide (NaOH) and potassium hydroxide (KOH) plus e.g., isopropanol causes anisotropic etching based on the lowest etching rate of Si(111) surfaces [2] because of the most-closely packed structure, leading to the formation of pyramidal structure which consists of (111) surfaces. However, the pyramidal structure is not so sharp, and hence incident light reflected twice at the Si surfaces goes out, resulting in insufficiently low reflectivity in the range between 10 and 20 % [3]. Therefore, anti-reflection coating is necessary to obtain lower reflectivity, but its formation is time- and cost-consuming, and reflectivity only in the limited wavelength and incident angle regions becomes low. In the case of poly-crystalline Si (poly-Si) solar cells, anisotropic alkaline etching cannot form uniform textured surfaces because of the presence of various surface orientations, and acid etching using nitric acid (HNO_3) plus hydrofluoric acid (HF) is usually employed to form rough surfaces [4]. However, the reflectivity is higher (i.e., ~20 %) than that of mat-textured surfaces on single crystalline Si.

Porous Si layer can be formed by use of metal particles to drastically decrease the Si surface reflectivity [5,6]. When Si substrates with metal particles such as Ag [5] and Pt [6] are immersed in HF plus hydrogen peroxide (H_2O_2) solutions, etching of Si occurs at the contact points of metal particles with Si, and consequently, metal particles move into the Si substrates, resulting in the pore formation. Due to the production of

the porous Si layer, the surface reflectivity greatly decreases. However, there are following disadvantages in application of this method to Si solar cells: i) metal particles, which seriously degrade solar cell performance because of formation of energy states in the Si band-gap, and thus act as electron-hole recombination centers, cannot be collected and removed completely, ii) the method is time-consuming, iii) the method is difficult to apply to large size (cf. 15×15 cm^2) solar cells, iv) properties of the porous Si layer such as depth and direction of pores cannot be well controlled.

Recently, a method has been developed to fabricate low-reflectivity Si surfaces, in which a mold with a catalytic Pt layer is contacted with Si immersed in H_2O_2 plus HF solutions [7]. When the mold possesses a pyramidal structure, inverted pyramidal structure is formed on Si surfaces, resulting in a reflectivity slightly lower than that of the mat-textured surfaces. Using this method, however, the reflectivity of large Si areas cannot be made low because the solutions are supplied to Si surfaces only from the edge regions of the contacted specimens.

In this chapter, a method was developed for the formation of ultra-low reflectivity Si surfaces. When a Pt mesh is contacted with Si wafers immersed in H_2O_2 plus HF solutions, the mesh structure is instantaneously transferred to the Si surfaces and simultaneously, a nanocrystalline Si layer is formed on the surface, resulting in an ultra-low reflectivity.

3-2   Experiments

The procedure of the developed surface structure chemical transfer (SSCT) method is schematically shown in Figure 3-1. Boron-doped polished p-type Si(100), Si(111) and poly-Si wafers were immersed in 15 wt% H_2O_2 plus 25 wt% HF solutions at room temperature, and the wafers were contacted with a Pt mesh (Figure 3-1 inset) attached to a roller at the rate of ~3 cm/s, and therefore, 6 inch wafers could be treated in less than 10 s. Figures 3-2a and 3-2b show the black Si(100) and polycrystalline Si specimens after the SSCT method, respectively. Note that some areas in the Si wafers didn't turn black due to the non-contact with the Pt mesh during the rolling procedure.

Scanning electron micrographs (SEM) were measured using a HITACHI S-2150 microscope with the incident electron energy of 20 keV. Transmission electron micrograph (TEM) measurements were carried out using a JEOL EM-3000F microscope with the incident electron energy of 300 keV. Photoluminescence (PL) spectra were measured using a JASCO CT100GD grating spectrometer and a photomultiplier tube at room temperature. The excitation light source was a 325 nm He-Cd laser. Reflectance spectra were recorded using a JASCO V-570 spectrometer with an integrating sphere. Minority carrier lifetime was determined by microwave photoconductance decay (μPCD) method using a KOBELCO LTA-1512 wafer lifetime measuring system.
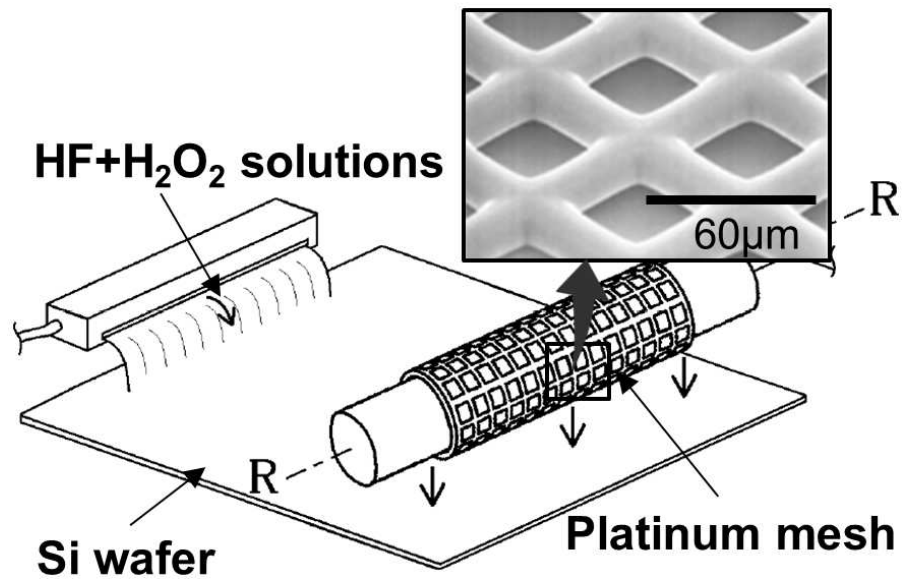
Fig. 3-1. Procedure of the SSCT method.
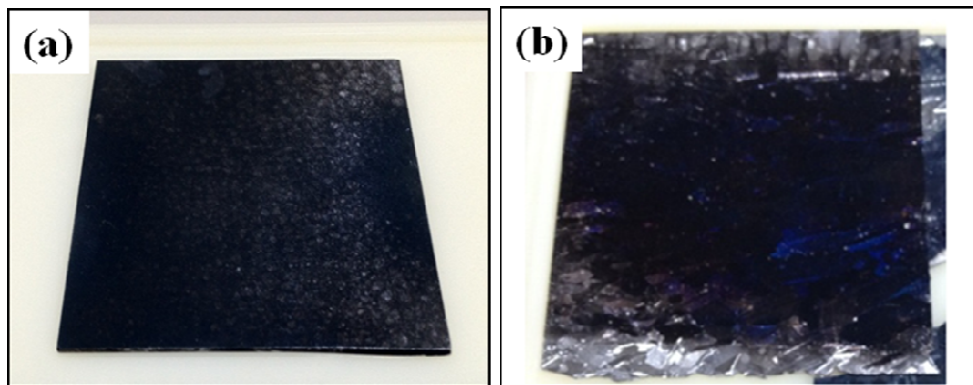
Fig. 3-2. Si(100) (a) and polycrystalline Si (b) surfaces after the SSCT method.

3-3   Results and Discussion

3-3-1 Surface structure chemical transfer on various Si surfaces

Fig. 3-3a – 3-3c show the Si(100), Si(111), and polycrystalline Si surfaces, respectively, after the SSCT method. It was observed that the structure of the mesh was transferred onto the surface of the Si wafers. Regardless of the surface orientation, the chemical transfer reaction of the mesh structure can be carried out. The surface structure chemical transfer reaction was previously observed to occur by the following chemical reactions [8]:

$$H_2O_2 \rightarrow H_2O + O \qquad (3\text{-}1)$$

$$Si + 2O \rightarrow SiO_2 \qquad (3\text{-}2)$$

$$SiO_2 + 6HF \rightarrow H_2SiF_6 + 2H_2O \qquad (3\text{-}3)$$
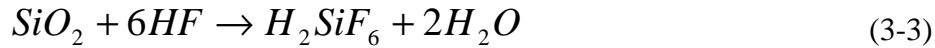
First, H_2O_2 decomposes at the Pt surface producing O atoms (3-1). The generated O atoms easily react with Si due to the low activation energy for Si oxidation (3-2). Finally, the formed SiO_2 is immediately etched by HF (3-3). Oxidation of Si by H_2O_2 was previously determined to be the rate-determining step [8]. However, the activation energy of the Si oxidation is low, resulting to the Si oxidation occurring at a high rate. As a result, the transfer of the mesh structure onto the surface can be carried out at room temperature unlike the reaction for the formation of pyramidal textured surfaces, i.e., 80°C.

65
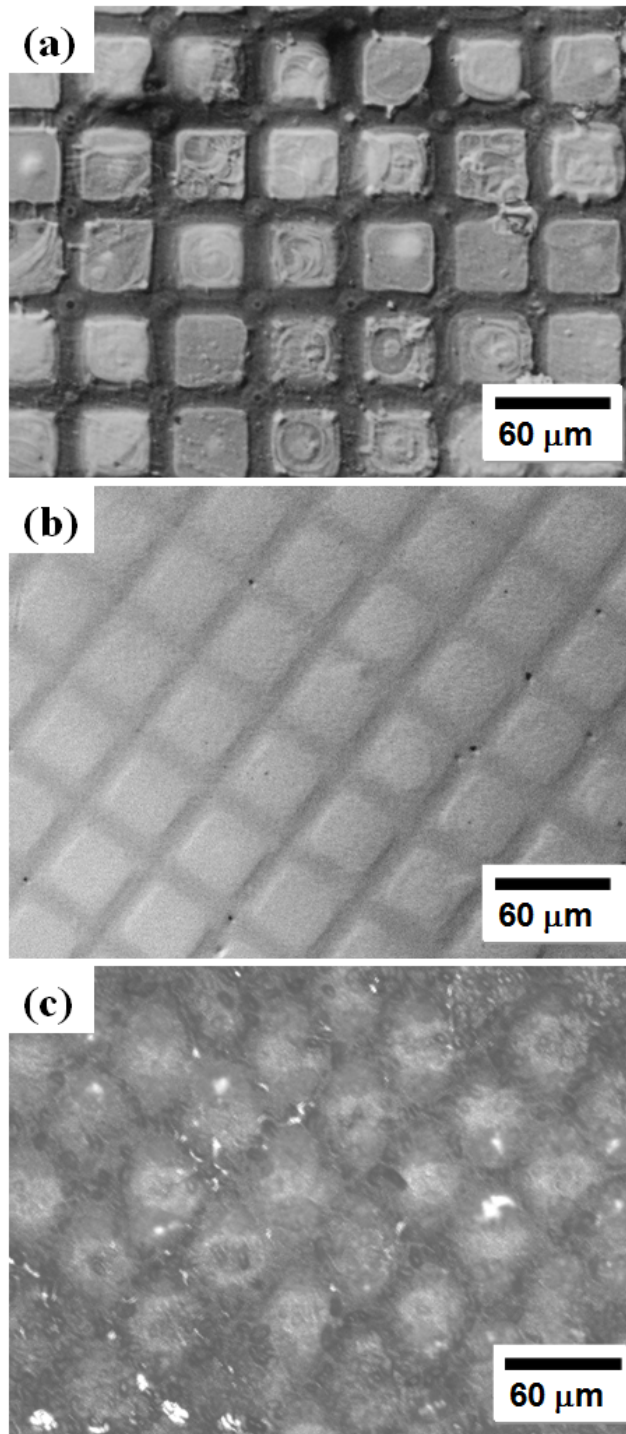
Fig. 3-3. Micrographs of the Si(100) (a), Si(111) (b) and polycrystalline Si (c) surfaces after the SSCT method.

3-3-2 Ultra-low reflectivity Si(100) and poly-Si surfaces produced by the SSCT method

Fig. 3-4 shows the reflectivity of the Si(100) surface before and after the SSCT method. The reflectivity of the mirror Si(100) surface was observed to be in the range of 40 and 80% in the 300 – 800 nm wavelength region (curve a). After the SSCT method, the reflectivity was greatly reduced to a range of 2 and 4% (curve b), which was much lower than that of single crystalline pyramidal-textured Si surfaces formed by anisotropic alkali etching (curve c).
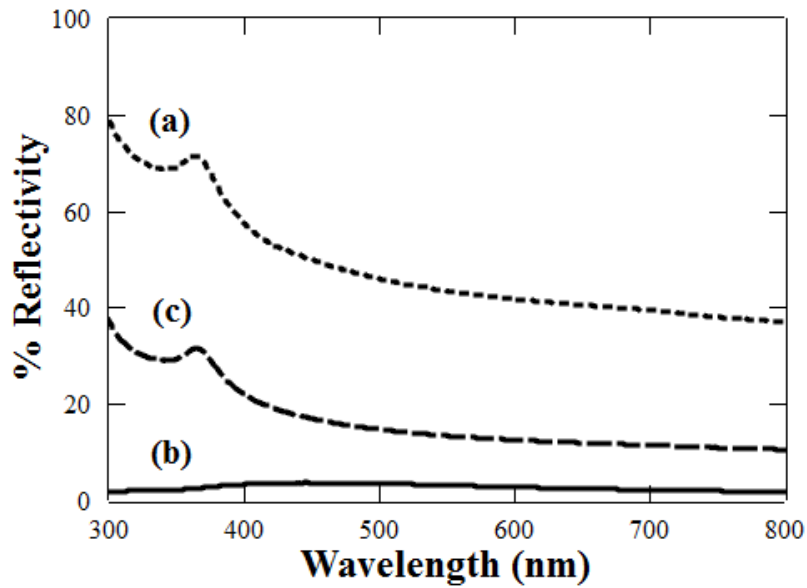
Fig. 3-4. Reflectance spectra of the Si(100) surfaces before (a) and after (b) the SSCT method. Reflectance spectrum of the pyramidal-textured Si surfaces formed on Si(100) surfaces by anisotropic alkaline etching is shown by curve (c) for reference.

Fig. 3-5, on the other hand, shows the reflectivity of the poly-Si before and after the SSCT method. The reflectivity of the as-sliced poly-Si surface was observed to be in the range 35 – 70% in the 300 – 800 nm wavelength region (curve a). After the SSCT method, the reflectivity was greatly reduced to a range of 2.5 – 4.5% which was much lower than that of isotropic acid-etched polycrystalline Si surfaces (curve c).
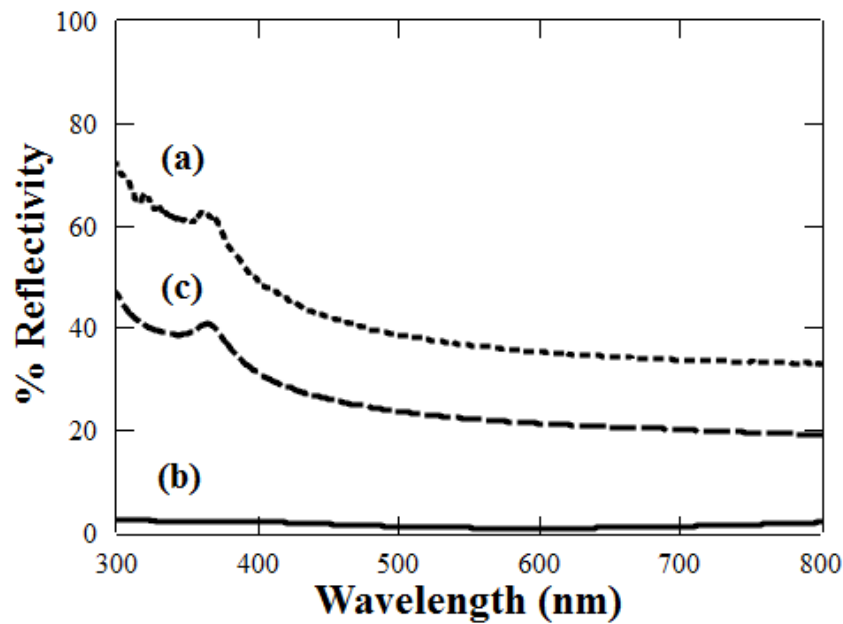
Fig. 3-5. Reflectance spectra of the polycrystalline Si surfaces before (a) and after (b) the SSCT method. Reflectance spectra of an acid etched polycrystalline Si surface formed is shown by curve (c) for reference.

In the reflectivity measurements, an integrating sphere was used to collect scattered light. Therefore, the ultra-low reflectivity is not due to surface roughness but to prevention of reflection both at the air/nanocrystalline Si and nanocrystalline Si/Si interfaces.

3-3-3 Si nanostructures formed after the SSCT method

The ultra-low reflectivity for the SSCT treated Si surfaces as shown in Figs. 3b and 3-5b cannot be attributed to the transfer of the mesh structure. The structure formed by the mesh pattern is not a steep structure and ~50% of the total Si surface remains flat after the chemical transfer reaction [18]. Therefore, the ultra-low reflectivity surfaces (i.e., between 2 and 4%) is attributed not to the mesh structure on the Si surface after the chemical transferring reactions, but to that of nanocrystalline Si produced by the electrochemical reaction caused by hole diffusion, as described below.

After the SSCT method, the Si(100) surface and polycrystalline Si surfaces were found to possess nanometer scale roughness (Fig. 3-6a and 3-6b) due to the formation of nanocrystalline Si. AFM measurements show the root-mean-square micro-roughness on the fabricated nanocrystalline Si surface was ~20 nm. Figs. 3-6c and 3-6d show the cross-sectional TEM micrograph of the nanocrystalline Si layer for Si(100) and polycrystalline Si surfaces, respectively. The thickness of the nanocrystalline Si layer was in the range between 100 and 150 nm. The diameter of a single Si nanocrystal shown in Fig. 3-6e is ~2.5 nm. Unlike metal-assisted porous Si formation [5,6], no micropores and no metal particles are visible in the nanocrystalline Si layer, in contrast to porous Si formed by metal particles [5]. We have confirmed that the concentration of Pt on the Si surfaces was less than the detection limit of total reflection X-ray fluorescence spectroscopy using synchrotron radiation of SPRING 8 (i.e., 1×10^9 atoms/cm^2).
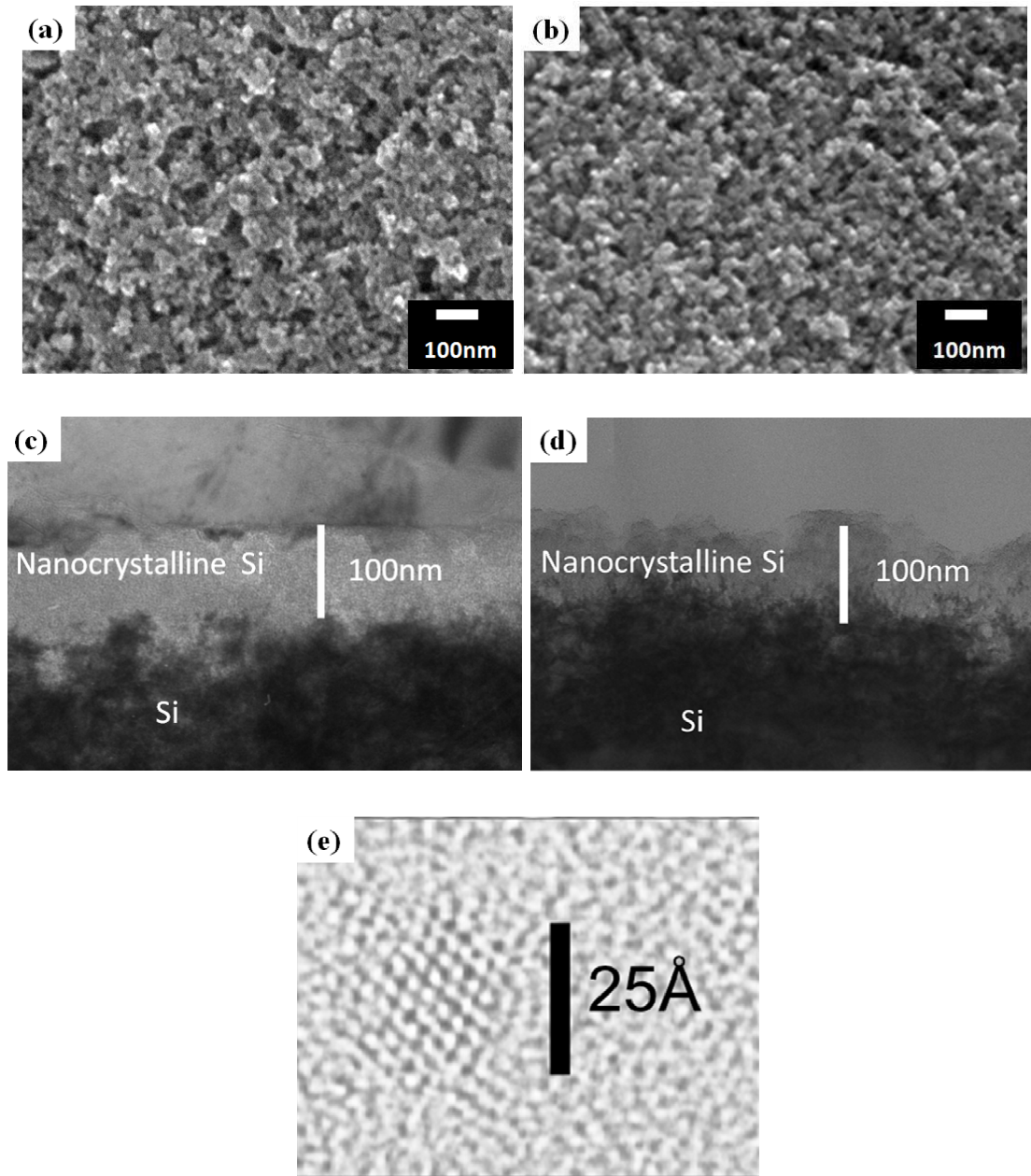
Fig. 3-6. SEM micrograph of the Si(100) (a) and polycrystalline Si (b) nanocrystalline Si surface after the SSCT method. Cross-sectional TEM micrograph of the nanocrystalline Si layer/Si(100) (c) and nanocrystalline Si layer/polycrystalline Si (d) structures after the SSCT method. Cross-sectional TEM micrograph of a single nanocrystalline Si (e).

3-3-4 Formation mechanism of the ultra-low reflectivity nanocrystalline Si surface

Figs. 3-7a and 3-7b show the proposed mechanism of the formation of ultra-low reflectivity nanocrystalline Si surfaces by the SSCT method.   The early-stage reaction and the subsequent reaction are shown in Figs. 7a and 7b, respectively. In each case, decomposition of H_2O_2 proceeds at the surface of the Pt mesh (3-4):

$$H_2O_2 + H^+ \rightarrow H_2O + OH^- + 2h^+ \qquad\qquad (3\text{-}4)$$
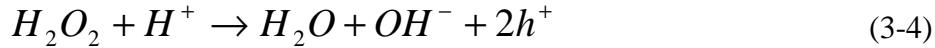
The acid dissociation constant for H_2O_2 of 11.8 is much higher than that for HF of 3.6, indicating that H^+ ions included in the reaction come from HF. Due to the high catalytic activity of Pt, this reaction occurs rapidly, resulting in formation of holes, h^+, in Pt. The generated holes are injected to Si and diffuse to the Si surface, causing the following reaction of Si dissolution (3-5):

$$Si + 6HF + 2h^+ \rightarrow H_2SiF_6 + H_2 + 2H^+ \qquad\qquad (3\text{-}5)$$
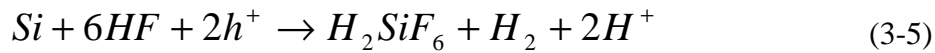
Si dissolution is likely to proceed from places where holes are trapped, e.g., surface states, resulting in the formation of nanocrystalline Si in the surface region (Fig. 3-7a). The distance between the Pt wires of the mesh of ~60 μm is shorter than the hole diffusion length in Si, i.e., 100 - 300 μm. Therefore, nanocrystalline Si is formed not only on the contacted regions of the Si surface with the Pt mesh but also on the non-

contacted regions.
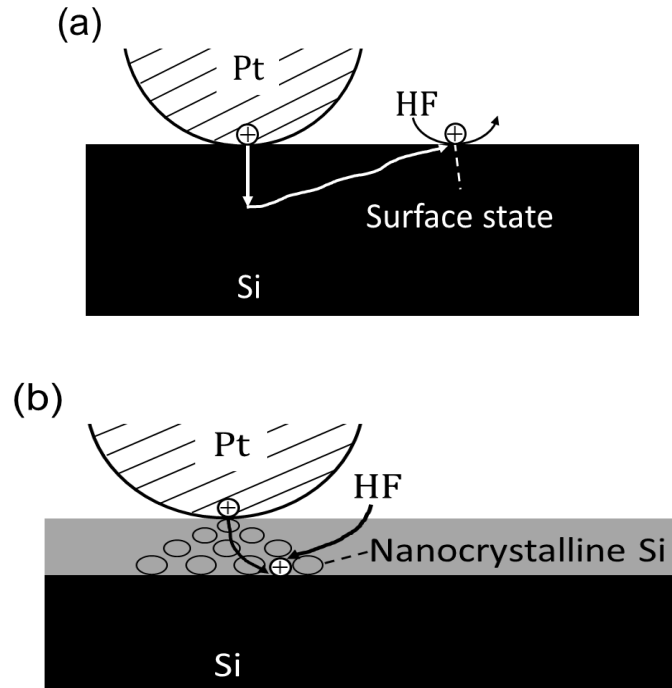
Fig. 3-7. Mechanism of the SSCT method: (a) early-stage reaction; (b) subsequent reaction after formation of a surface nanocrystalline Si layer.

After the formation of the nanocrystalline Si layer in the surface region, the HF solution can penetrate through the spaces, and the nanocrystalline Si layer becomes thicker (Fig. 3-7b). With this formation mechanism (i.e., reaction starting from the Si surface), the porosity of the nanocrystalline Si layer is high near the surface and decreases with the depth. Consequently, the refractive index is low near the surface, and continuously increases with the depth. Fig. 3-8a shows a graded porosity structure model, wherein the refractive index continuously increases from the surface (n_1) to near

the bulk Si (n_N). The ultra-low reflectivity indicates that the refractive index of the nanocrystalline Si layer near the surface (n_1) is close to the air (i.e., 1) and that near the crystalline Si (n_N) is close to that of Si (i.e., 3.8 – 4.5), which prevents light reflection both at the air/nanocrystalline Si and nanocrystalline Si/crystalline Si interfaces.

The dimensions of the nanocrystalline Si is much smaller than the wavelength of light, therefore, the relationship between the reflectivity of the surface and refractive index for normal incident light can be described by the simplified Fresnel equation (3-6) [19]:

$$\%R = \left[\frac{n_j - n_k}{n_j + n_k} \right]^2 \times 100\% \tag{3-6}$$

where *%R* is the reflectivity of the surface, n_j and n_k are two adjacent layers with different refractive indices. Figs. 3-8b and 3-8c show the refractive index vs. depth model plots for a crystalline Si surface and a nanocrystalline Si/Si structure, respectively. For a crystalline Si surface, the refractive index drastically changes from air (i.e., 1) to Si (i.e., 3.8 – 4.5), thus resulting in high reflectivities (i.e., above 40%) as shown in Figs. 3-4a and 3-5a. On the other hand, for the nanocrystalline Si/Si structure, it is shown that the surfaces possess ultra-low reflectivities (i.e. between 2 and 4%). If we assume that most of the reflections occur at the air/nanocrystalline Si interface, and that the refractive index continuously increases along the nanocrystalline structure, the refractive index of the nanocrystalline Si at the air/nanocrystalline Si interface is estimated to be in the range between 1.3 and 1.5 (corresponding the reflectivities between 2 and 4%) as shown in Fig. 3-8c.
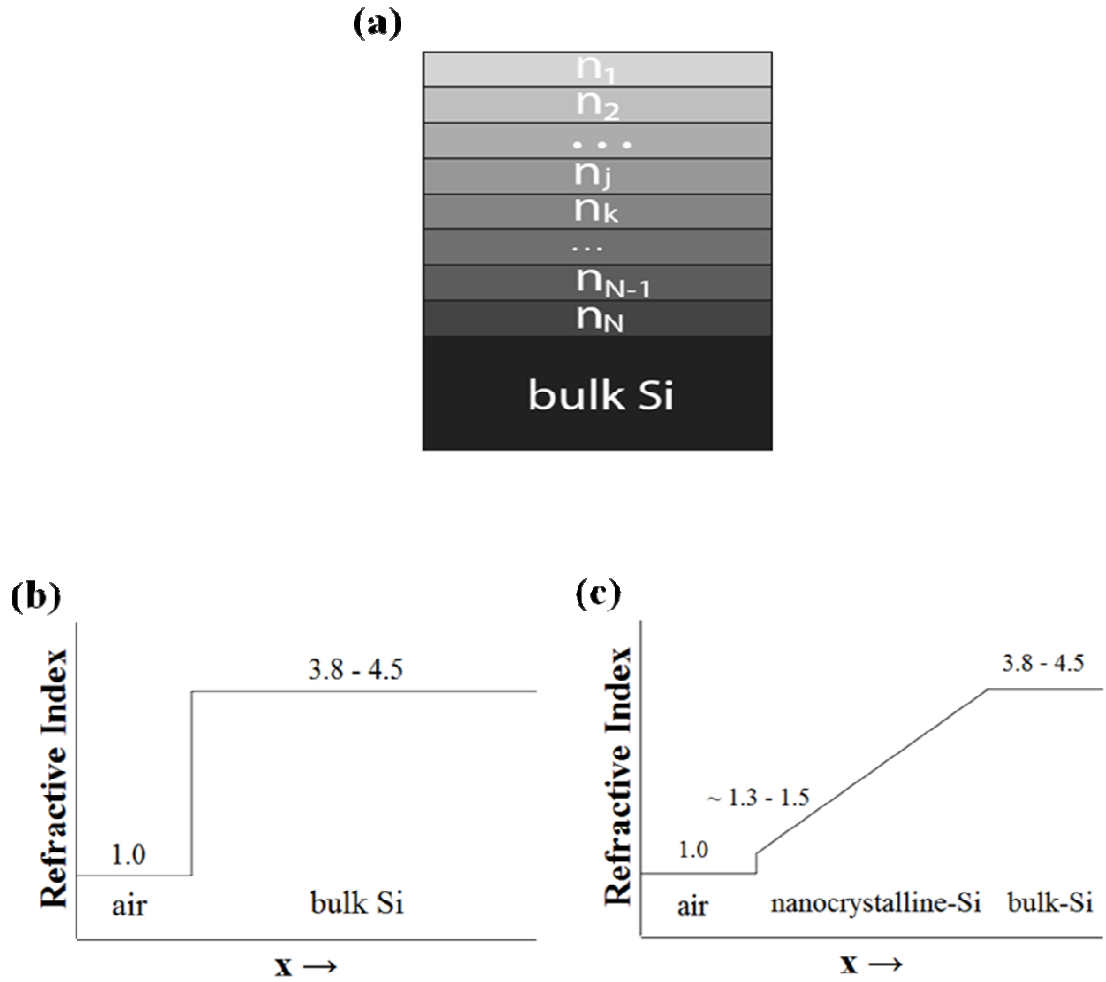
Fig. 3-8. Graded porosity structure (a) model. Plot of the refractive index vs. depth for: a crystalline Si surface (b); and a nanocrystalline Si/Si structure (c) assuming that most of the reflections occur at the air/nanocrystalline Si interface, leading to the reflectivity in the range between 2 and 4%.
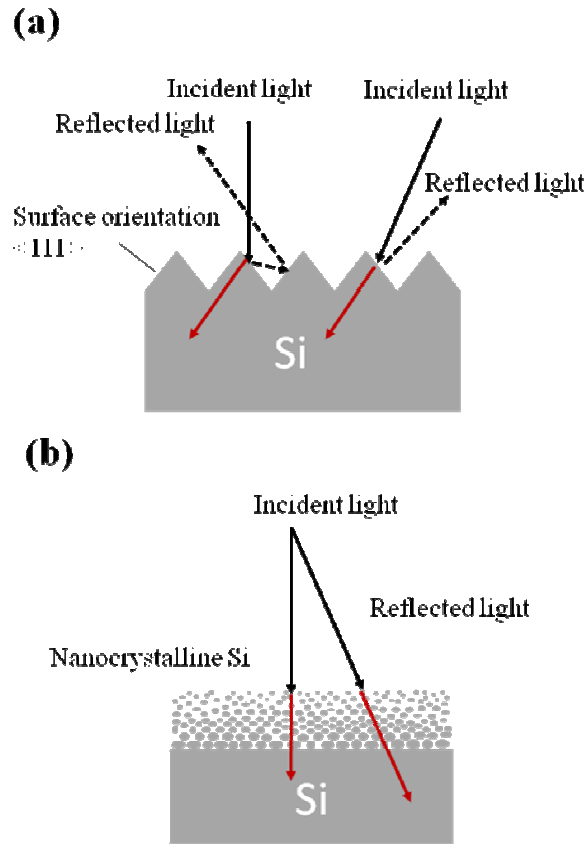
Fig. 3-9. Mechanism of light reflection by pyramidal textured (a), and nanocrystalline Si (b) surfaces.

Fig. 3-9. shows the mechanism of light reflection by pyramidal textured and nanocrystalline Si surfaces. In a textured surface, light can hit the surface twice; however, the *%R* of light at each reflection is still above 40%. In a nanocrystalline Si surface, there is no large difference between the refractive index or air and nanocrystalline Si interface. The refractive index of the nanocrystalline layer gradually increases with depth resulting to the ultra-low reflectivity, i.e., *%R = 2%*.

3-3-5 Photoluminescence of nanocrystalline Si

Fig. 3-10 shows the PL spectrum of the nanocrystalline Si layer. A strong visible PL peak was observed at ~670 nm (1.85 eV) with the full width at half maximum of ~150 nm, which was similar to previous studies for nanocrystalline Si [8-12] and porous Si [13,14].
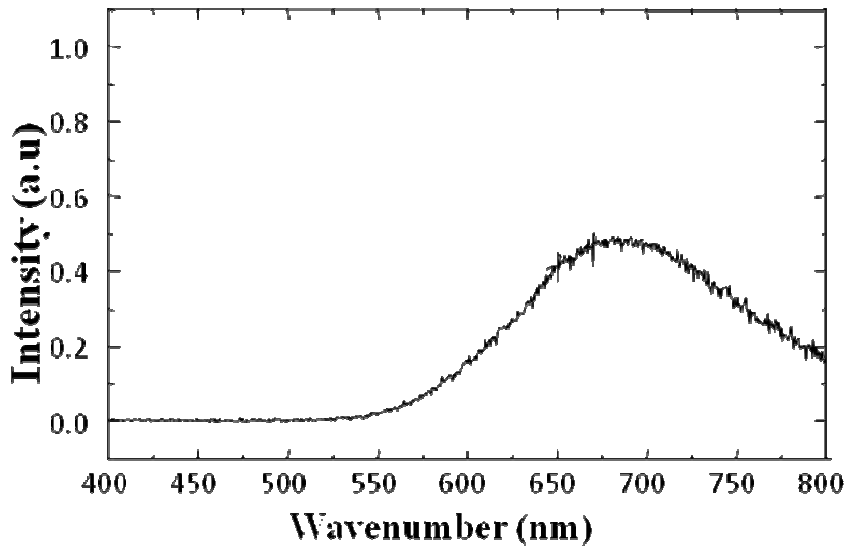
Fig. 3-10. Photoluminescence spectrum for the nanocrystalline Si layer formed on the Si surface after the SSCT method.

In particular, the relationship between the PL peak energy and the size of nanocrystalline Si (Fig. 3-6e) is in good agreement with those reported in the previous studies on nanocrystalline Si embedded in SiO_2 [10,11] and hydrogen-terminated nanocrystalline Si [12]. Therefore, it is highly probable that the PL peak arises from

band-to-band transition for nanocrystalline Si whose band-gap is widened due to the quantum-size effect [15]. On the other hand, there is a possibility that the layer consists of nanocrystalline and amorphous phases, in analogy to previous literature [16,17]. Therefore, it cannot be excluded that the PL emission results from an efficient band-gap, i.e., an average between the band-gap of the different phases, or from the amorphous phase within the layer.

3-3-6 Minority carrier lifetime of Si surface after the formation of nanocrystalline Si

Fig. 3-11 shows the minority carrier lifetime of the Si wafers. Only on the square region shown by the dotted lines in the figure, the nanocrystalline Si layer was formed by the SSCT method. It is clearly seen that the minority carrier lifetime of the non-contacted region was ~1 μs and it increased to ~5 μs after the SSCT method. Optimizing the surface passivation method of the Si surfaces, i.e., I_2 passivation, the minority carrier lifetime of ~36 μs was achieved. The effective minority carrier lifetime can be represented by (3-7) [20]:

$$\frac{1}{\tau_{effective}} = \frac{1}{\tau_{bulk}} + \frac{1}{\tau_{surface}}$$

(3-7)

where, $\tau_{effective}$ is the effective minority carrier lifetime, τ_{bulk} is the bulk lifetime and $\tau_{surface}$ is the surface lifetime.
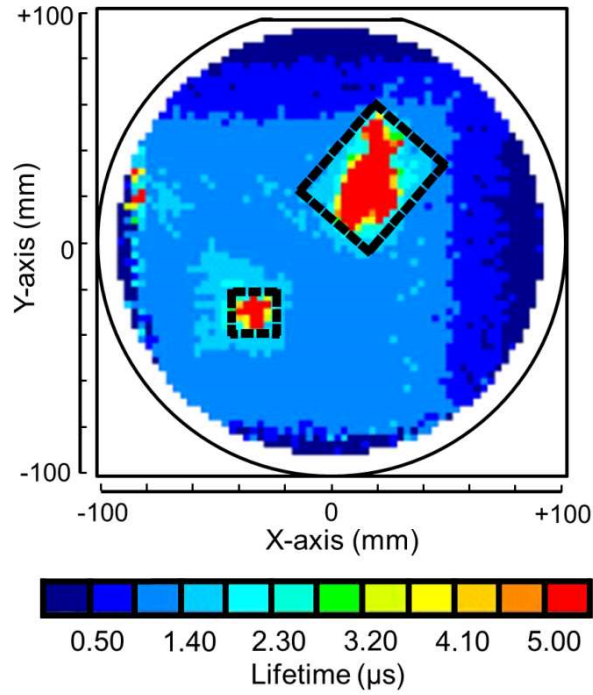
Fig. 3-11. Minority carrier lifetime for the Si surface on which a nanocrystalline Si layer is formed by the SSCT method in the area denoted by the dotted lines.

Assuming that the Si bulk lifetime is 36 μs, the surface and interface lifetime after the SSCT method is estimated to be ~6 μs from the observed effective lifetime. On the other hand, the observed effective minority carrier lifetime of the Si wafer after the HF treatment is only ~1.5 μs and the surface lifetime is estimated to be ~1.6 μs. These results clearly show that the minority carrier lifetime of the surface and the interface for the nanocrystalline Si layer/Si structure is higher than that of the Si surface.

3-3-7   Band-gap widening of the nanocrystalline Si

Fig. 3-12a shows the band-gap energy for the crystalline Si and the nanocrystalline Si after the SSCT method. The band-gap energy of 1.8 eV was approximated from the PL peak of 670 nm. Fig. 3-12b shows a band energy diagram for the crystalline Si/nanocrystalline Si interface.
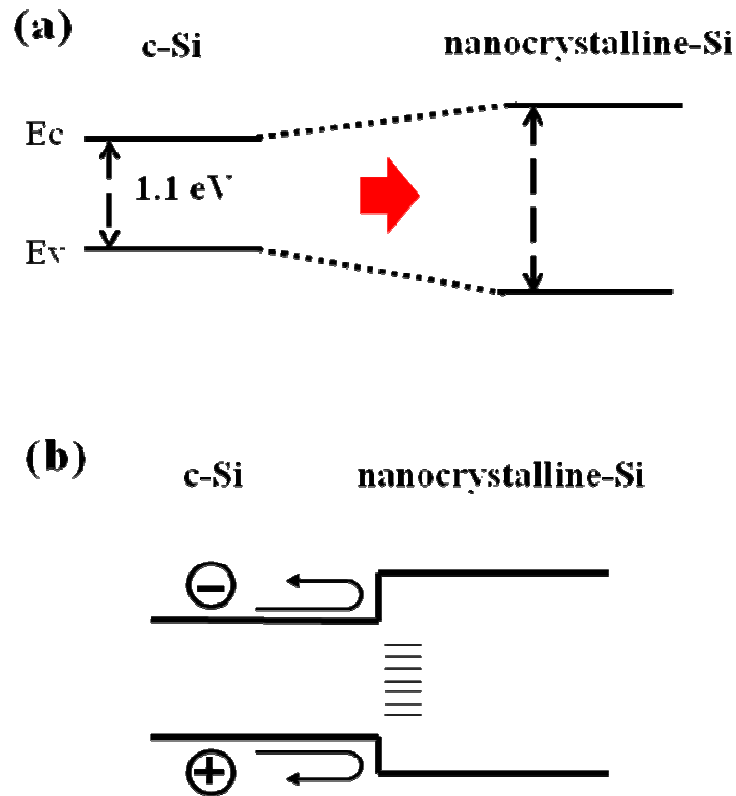
Fig. 3-12. Band-gap energy of: crystalline Si; and nanocrystalline Si after the SSCT method (a). Minority carriers being repelled at the crystalline Si/nanocrystalline Si interface.

When the nanocrystalline Si is produced from a crystalline Si, the band-gap energy widens forming an energy barrier at the crystalline Si/nanocrystalline Si interface. Due to the band-gap widening, it is possible that minority carriers are repelled at the crystalline Si/nanocrystalline Si interface, leading to suppression of electron-hole recombination. The suppressed electron-hole recombination at the crystalline Si/nanocrystalline Si interface leads to the increase in minority carrier lifetime as shown in Fig. 3-11.

3-4　Summary

A simple method for the fabrication of ultra-low (i.e., 2~4%) reflectivity Si(100) and polycrystalline Si surfaces has been developed using the SSCT method which simply involves contact of a Pt mesh with a Si wafer immersed in H_2O_2 plus HF solutions. The ultra-low reflectivity results from formation of a nanocrystalline Si layer of 100~150 nm thickness. The nanocrystalline Si layer gives a PL peak at ~670 nm, and recombination of electron-hole pairs at the nanocrystalline Si/Si interface and the air/nanocrystalline Si interface is suppressed by enlargement of the nanocrystalline Si band-gap, leading to the increase in the minority carrier lifetime.

References

[1]   F. Restrepo and C. E. Backus, *IEEE Trans. Electron Dev.* **ED-23**, 1195 (1976)

[2]   A. M. Jeffery, *Solar Cells: An Introduction of Crystalline Photovoltaic Technology*, Kluwer Academic Publishers, Dordrecht, 1997, p. 137

[3]   S. Kwon, J. Yi, S. Yoon, J. S. Lee, and D. Kim, *Curr. Appl. Phys.* **9**, 1310 (2009)

[4]   Y.-T. Cheng, J.-J. Ho, S.-Y. Tsai, Z.-Z. Ye, W. Lee, D.-S. Hwang, S.-H. Chang, C.-C. Chang, and K. L. Wang, *Sol. Ener.* **85**, 87 (2011)

[5]   C. Chartier, S. Bastide, and C. Lévy-Clément, *Electrochim. Acta.* **53**, 5509 (2008)

[6]   S. Yae, T. Kobayashi, T. Kawagishi, N. Fukumuro, and H. Matsuda, *Sol. Ener.* **80**, 701 (2006)

[7]   T. Fukushima, A. Ohnaka, M. Takahashi, and H. Kobayashi, *Electrochem. Solid-State Lett.* **14**, B13-B15 (2011)

[8]   C.-Y. Lin, Y.-K. Fang, S.-F. Chen, S.-H. Chang, and T.-H. Chou, *Mater. Sci. Eng. B* **134**, 99 (2006)

[9]   I. Umezu, T. Kimura, and A. Sugimura, *Physica B* **376**, 853 (2006)

[10]   G.Ledoux, J.Gong, F.Huisken, O.Guillois, and C.Reynaud, *Appl. Phys. Lett.*, **80**, 4834 (2002)

[11]   Chun-Yu Lin, Yean-Kuen Fang, Shin-Fang Chen, Shiuan-Ho Chang, Tse-Heng Chou, *Mater. Sci. Eng. B*, **134**, 99-102 (2006)

[12]   Roberto Guerra, Francesco Cigarini, and Stefano Ossicini, *J. Appl. Phys.*, **113**, 143505 (2013)

[13] A. Benilov, I. Gavrilchenko, I. Benilova, V. Skryshevsky, and M. Cabrera, *Sens. Actuators A***137**, 345 (2007)

[14]   J.-C. Lin, W.-C. Tsai, and P.-W. Lee, *Electrochem. Commun.* **9**, 449 (2007)

[15]   C. Meier, A. Gondorf, S. Lüttjohann, A. Lorke, and H. Wiggers, *J. Appl. Phys.* **101**, 103112 (2007)

[16] Luigi Bagolini, Alessandro Mattoni, and Luciano Colombo, *Appl. Phys. Lett.* **94**, 053115 (2009)

[17] Daniela Cavalcoli, Marco Rossi, and Anna Cavallini, *J. Appl. Phys.* **109**, 053719 (2011)

[8] M. Takahashi, T. Fukushima, Y. Seino, W.B. Kim, K. Imamura, and H. Kobayashi, *J. Electrochem. Soc*. **160** H443 (2013)

[19] E. Hecht *Optics* (Addison-Wesley) (1987)

[20] A. Buczkowski, Z. J. Radzimski, G.A. Rozgonyi, and F. Shimura, *J. Appl. Phys*. **72** 2873 (1992)

Chapter IV

Ultra-low Reflectivity Nanocrystalline Si Solar Cells Fabricated by Surface Structure Chemical Transfer Method

4-1   Introduction

In chapter 3, a simple method to produce ultra-low reflectivity Si surfaces by the surface structure chemical transfer method was introduced. In this chapter, solar cells were produced from the ultra-low reflectivity Si surfaces produced by SSCT.

The PERL structure solar cell, greatly reducing both reflection and recombination losses and having a conversion efficiency of 25% [1] is the highest ever recorded for a single crystal Si solar cell. The inverted pyramid structure together with the double layer anti-reflection coating produced a very high photocurrent density of 42.2 mA/cm^2 under AM1.5 1000 W/m^2 irradiation. However, due the very complicated structure, commercial production is not feasible as a result of the very high cost. The high reflectivity of Si arises from its high refractive index in the 300 nm – 1100 nm wavelength regions [2]. Due to this, less photo-generated electron-hole pairs are produced leading to low conversion efficiencies.

Low reflectivity nano-porous Si surfaces can be produced by the metal-assisted chemical etching of Si [3-4]. Noble metals such as Pt, Au, or Ag [6-7] are deposited on the Si surface and subsequently etched in solutions containing oxidants such as H_2O_2, HNO_3,etc. plus HF solutions. However, the nano-porous structure produced after the metal assisted etching cannot form a pn-junction due to the uncontrolled direction of the pores [8-9], and as a result, there is a need for an additional KOH / TMAH etch after the metal assisted etching which increases the reflectivity to above 10% [10].   Other disadvantages for the metal-assisted etching of Si are: 1) metal particles which seriously degrade solar cell characteristics reside in Si (Fig. 4-1) [7], 2) difficulty in application to large size (i.e., 6 inches) Si wafers, and 3) time-consuming.

In this chapter, solar cells were produced from the ultra-low reflectivity Si(100) and polycrystalline Si surface after the SSCT method. It was observed that the photocurrent density greatly increased after the SSCT method.
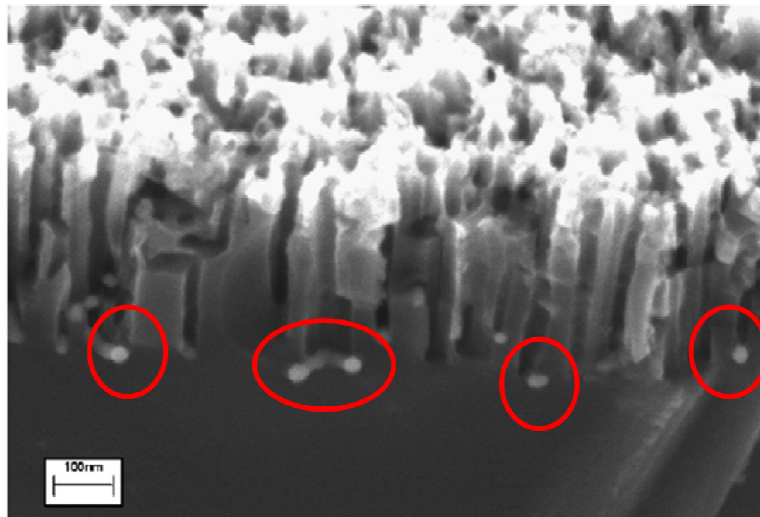
Fig. 4-1. The metal-assisted etching of Si. The metal particles residing at the bottom of the pores are encircled.

4-2   Experiments

Single crystalline Si and polycrystalline p-type Si wafers were used for the production of solar cells. For the single crystalline Si solar cells, polished boron-doped Si(100) czochralski (CZ) wafers with resistivities of 7-11 $\Omega\cdot$cm wafers were used; while for the polycrystalline Si solar cells, saw-damage removed (as described in Chapter 2) as-sliced boron-doped polycrystalline Si wafers with resistivities of 1-20 $\Omega\cdot$cm were prepared.

Field emission scanning electron micrographs (FE-SEM) were measured using a JSM-6335F with the incident electron energy of 20 keV.   Transmission electron micrograph (TEM) measurements were carried out using a JEOL EM-3000F microscope with the incident electron energy of 300 keV. Reflection spectra were recorded using a JASCO V-670 UV-Vis spectrometer attached to a JASCO automated absolute reflectance measurement ARMN-735 accessory.   Sheet resistances were measured using a four-point probe after the formation of the pn-junction. Solar cell characteristics were measured using a solar simulator at AM1.5 1000 W/m^2.

4-2-1 Solar cell production process sequence

Fig. 4-2a summarizes the solar cell production process. First, the Si wafers were cut into 5cm x 5cm squares. The Si wafers were then cleaned by the standard RCA cleaning method as described in chapter 2. Ultra-low reflectivity Si surfaces were then fabricated by the SSCT method as described in chapter 3.   The 5cm x 5cm square wafers were then further cut into 2.5cm x 2.5cm square wafers. pn-junction was then

formed from the 2.5cm x 2.5cm square wafers by the use of a commercial phosphorus dopant solution, and will be described in the next section. The p$^+$-region was formed by co-diffusing a boron source together with phosphorus [11-12]. Diffused phosphorus around the edges was then removed by mechanical sawing, to electrically isolate the cell front region from the rear cell region. Finally, ~1 μm Ag and Al electrodes were formed using the thermal evaporation method as the front and rear contacts. The solar cells produced, had an area of 2.5cm x 2.5cm. Fig. 4-2b shows the structure of the nanocrystalline Si solar cell. It must be noted that the solar cells didn't have any anti-reflection coating and passivation methods were not employed.
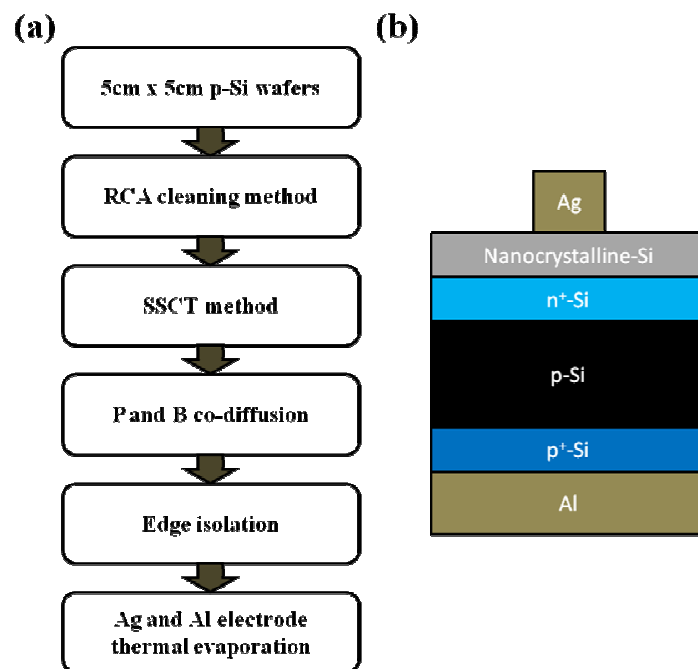
Fig. 4-2. The solar cell production process sequence (a) and the final structure of the solar cell (b)

4-2-3 Nanocrystalline Si doping process

The doping process for the nanocrystalline Si is shown in Fig. 4-3. The phosphorus dopant source, commercial phosphorus pentoxide (P_2O_5) in silica and organic solution (5 wt% P_2O_5, TOK, EPLUS-SC913) [13] was spread directly onto the nanocrystalline Si surface and was immediately spun at 3000 rpm for 30s. The dopant source was then oxidized at 600°C, forming a phosphosilicate glass (PSG) layer on the nanocrystalline Si. Phosphorus was then diffused through the nanocrystalline Si layer by increasing the temperature between 850 and 1000°C. The remaining PSG layer was then removed thoroughly by immersing the wafer in a 5% HF solution for 5 min.
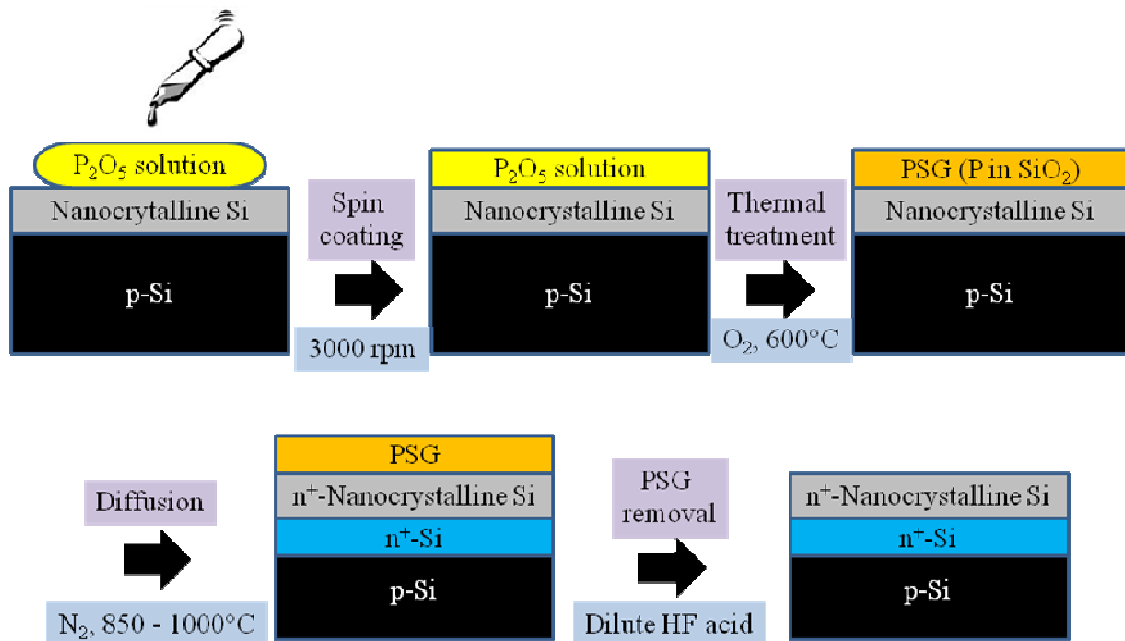
Fig. 4-3. The nanocrystalline Si doping process sequence.

4-3 Results and discussion

4-3-1 Nanocrystalline Si reflectivity after the formation of pn-junction

Fig. 4-4 shows the reflectivity of the nanocrystalline Si surface from Si(100) fabricated by SSCT before and after the formation of pn-junction. The reflectivity of the nanocrystalline Si surface before the formation of pn-junction was between 2 and 4% in the 300 – 800 nm wavelength regions (curve a). However, after the formation of pn-junction, the reflectivity was slightly increased to a range between 3 and 7% (curve b).

Fig. 4-4. Reflectance spectra of the nanocrystalline Si from Si(100) fabricated by the SSCT method before (a) and after (b) the formation of pn-junction.

4-3-2 Nanocrystalline Si structure after formation of pn-junction

Fig. 4-5a and 4-5b shows the SEM micrograph of the nanocrystalline Si surface from Si(100) fabricated by the SSCT method before and after the formation of pn-junction, respectively. Figs 4-5c and 4-5d show the cross-sectional TEM micrograph of the nanocrystalline layer before and after the formation of pn-junction, respectfully. It can be observed from the SEM micrographs that the surface still possesses nanocrystalline Si layer even after the formation of pn-junction. However, in the cross-sectional TEM micrographs, it can be observed that the thickness of the nanocrystalline Si layer was reduced by a few tens of nm after the formation of pn-junction.

During the formation of the pn-junction, the dopant source was oxidized to produce a PSG layer [14]. Therefore, it is possible that a surface portion of the nanocrystalline Si was also oxidized during the formation of PSG. During the PSG etching, the oxidized nanocrystalline Si region was also etched off together with the PSG layer [15]. This explains the decrease in the nanocrystalline Si thickness after the formation of pn-junction and PSG etching. The etching of the topmost nanocrystalline Si region may result in the removal of the low refractive index layer, as shown in chapter 3, thus the increase in the reflectivity after the formation of pn-junction.
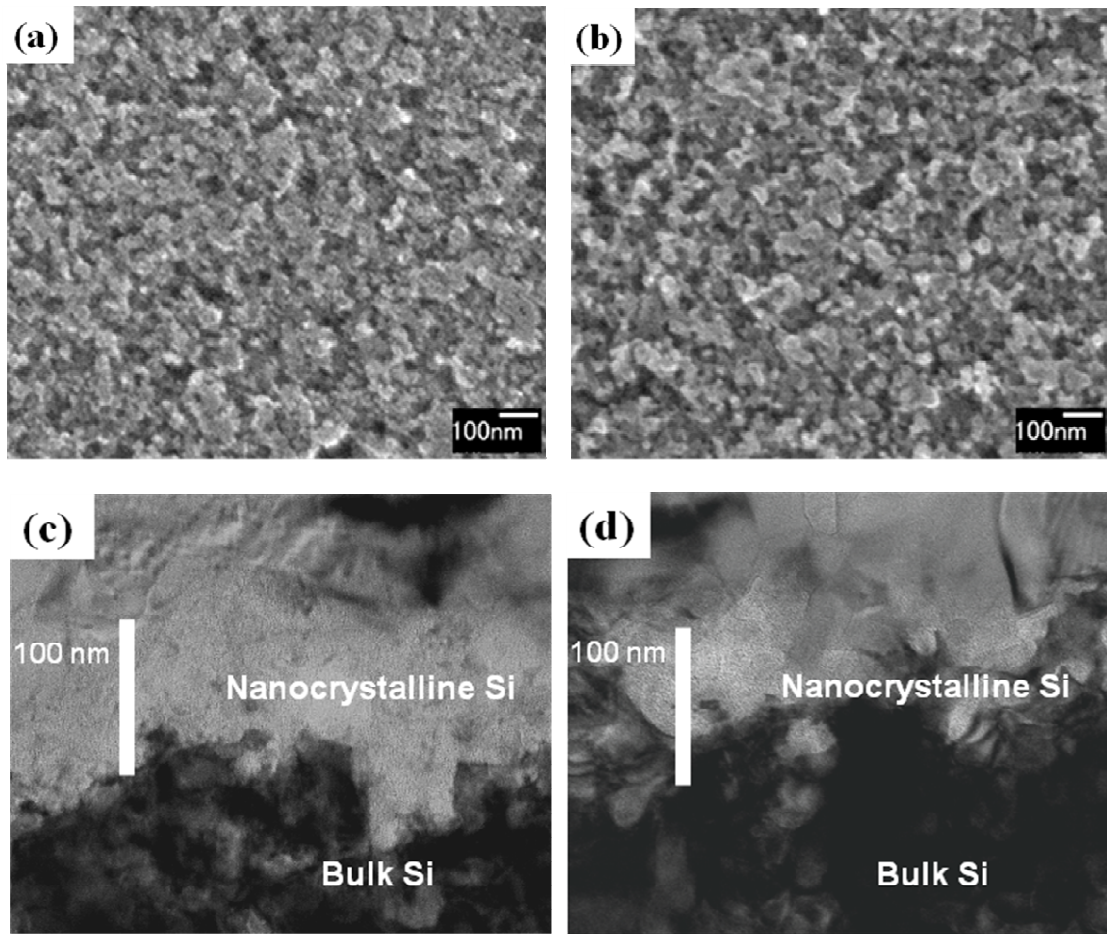
Fig. 4-5. SEM micrograph of the nanocrystalline Si surface from Si(100) fabricated by the SSCT method before (a) and after (b) the formation of pn-junction. Cross-sectional TEM micro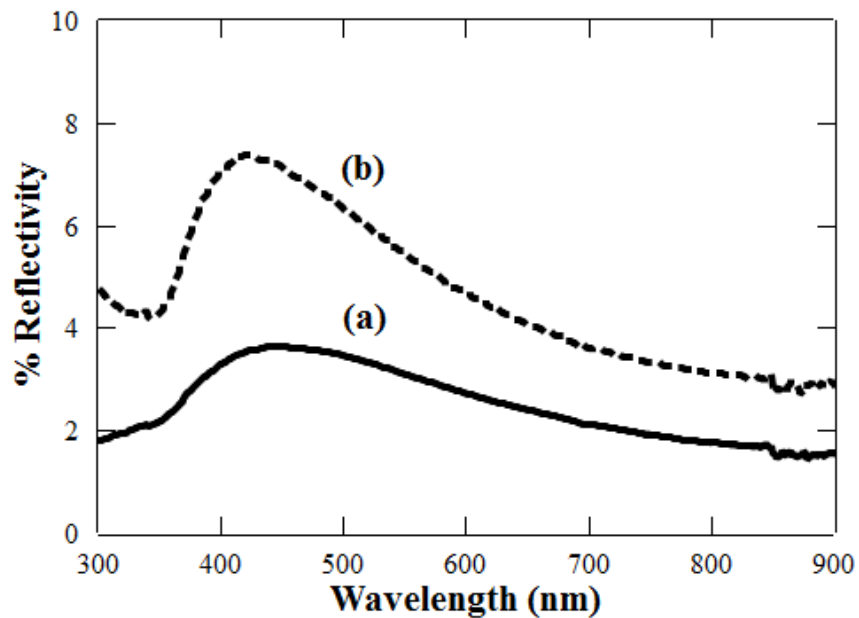graph of the nanocrystalline Si/Si structure from Si(100) fabricated by the SSCT method before (c) and after (d) the formation of pn-junction.

4-3-3 Nanocrystalline Si pn-junction formation

Fig. 4-6 shows the sheet resistance of the nanocrystalline Si surface at varying diffusion temperatures with a fixed diffusion time of 10 min. The sheet resistance decreased from ~1200 Ω/square to ~65 Ω/square as the diffusion temperature was increased from 850°C to 950°C. When the temperature is increased, the diffusion coefficient of the P-dopant atoms is also increased [16]. Therefore, more P-dopant atoms can diffuse through the nanocrystalline layer as the temperature is increased resulting in lower sheet resistance.
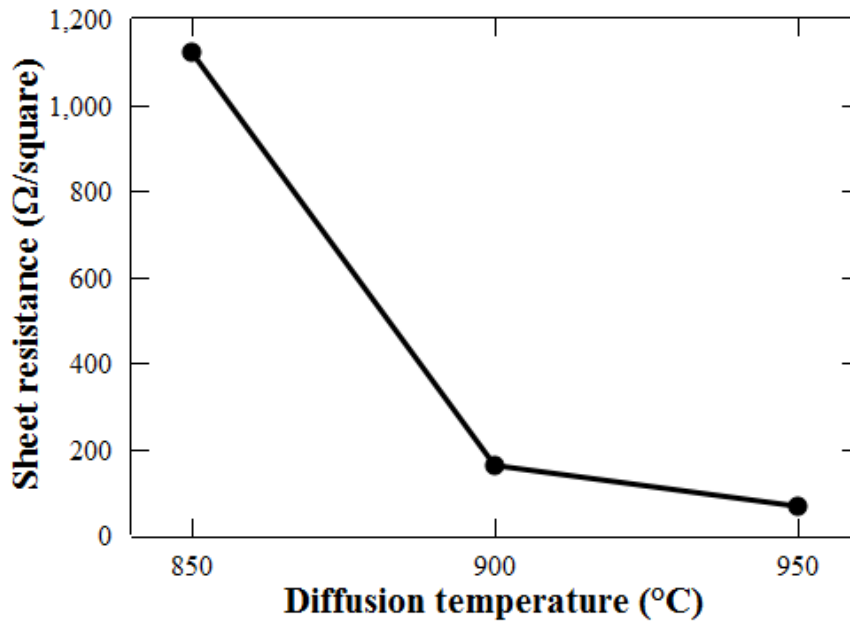
Fig. 4-6. Sheet resistances of the doped nanocrystalline Si/Si structure at various diffusion temperatures. The diffusion time is fixed to 10 min.

Fig. 4-7 shows the changes in sheet resistance for both nanocrystalline Si/Si and single crystalline Si specimens at a fixed diffusion temperature of 950°C in varying diffusion times. It can be observed that for both nanocrystalline Si/Si and single crystalline Si, the sheet resistance decreased as the diffusion time was increased from 10 min to 60 min. This is due to the formation of a thicker n-layer as the diffusion time is increased. However, it can also be observed that the sheet resistance of the nanocrystalline Si is lower than that of the single crystalline Si at any given doping condition. These results suggest that the diffusion mechanism of P-dopant atoms is different from a nanocrystalline Si surface as compared to a crystalline surface. Formation of the nanocrystalline Si surface leads to a significant increase in the surface area. Therefore, the P-dopant atoms diffuse from the entire area of the nanocrystalline Si layer and this surface-enhanced diffusion may lead to a higher concentration and thicker n-region for a nanocrystalline Si specimen.
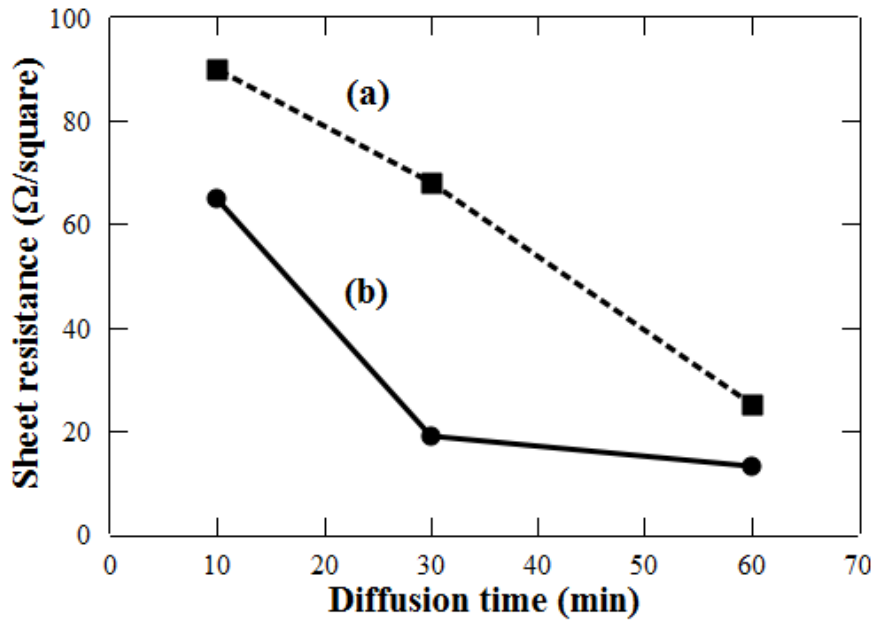
Fig. 4-7. Sheet resistance of the doped single crystalline Si (a) and nanocrystalline Si/crystalline Si specimens (b) at various diffusion times. The diffusion temperature was fixed to 950°C.

Fig. 4-8 shows the current-voltage characteristics of the nanocrystalline Si solar cells with various the sheet resistances. Curves a, b, and c corresponds to sheet resistances of 1120 Ω/square, 160 Ω/square, and 65 Ω/square respectfully. Curves a and b were observed to possess very low fill factors due to the very high series resistances. The high series resistance is the result of having high sheet resistances in the doped n-region. However, when the sheet resistance was decreased further to 65 Ω/square, the fill factor was increased due to the reduction of the series resistance in the doped n-region.
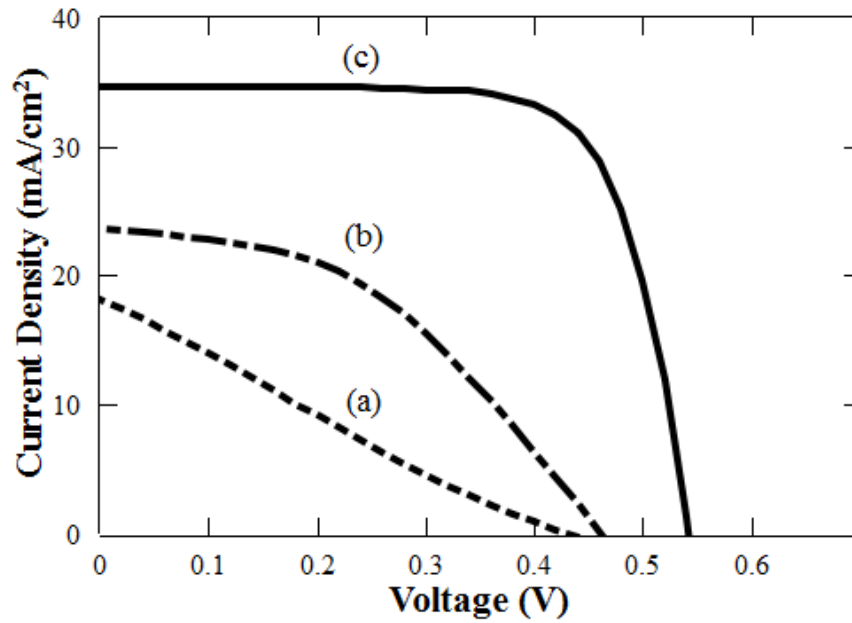
Fig. 4-8. I-V characteristics of the nanocrystalline Si solar cell with sheet resistances of 1200 Ω/square (a), 160 Ω/square (b) and 65 Ω/square (c).

Table 4-1. Solar cell parameters of nanocrystalline Si/crystalline Si structure at various sheet resistances.

Solar cell	V_{OC} (V)	J_{SC} (mA/cm^2)	FF	% n
1200 Ω/square	0.429	18.2	0.234	1.83
160 Ω/square	0.480	30.9	0.253	3.75
65 Ω/square	0.542	34.7	0.726	13.6

\

4-3-4 High photocurrent density nanocrystalline Si solar cells

The best nanocrystalline Si solar cells were produced at a diffusion temperature of 970°C for 10min. The sheet resistance was measured to be 60 Ω/square. Fig. 4-9

shows the current-voltage characteristics of the Si(100) with and without the SSCT method. Table 4-2 summarizes the V_{oc}, J_{sc}, FF, and efficiency of the solar cells as shown in Fig. 4-9. The 27.3 mA/cm^2 photocurrent density of the solar cell without SSCT increased by 42% to 38.8 mA/cm^2 after SSCT. The 0.567 V open-circuit voltage of the solar cell with SSCT slightly increased from 0.561 V that of the polished Si(100). However, the fill factor for the solar cell with SSCT was observed to slightly decrease to 0.754, as compared to 0.774 of a polished Si(100). The 11.9% conversion efficiency of the solar cell without SSCT was observed to increase to 16.6%, i.e., an absolute increase of 4.7%.
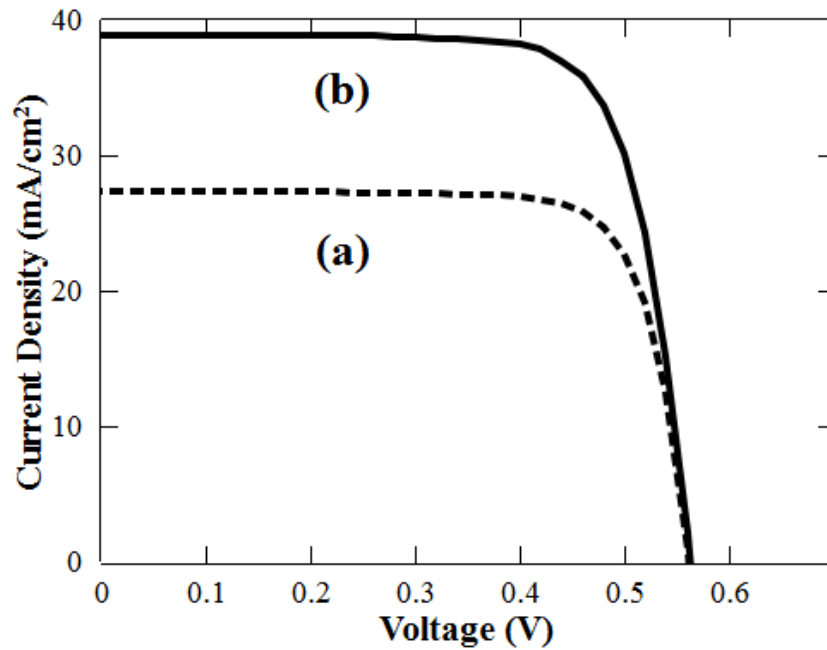
Fig. 4-9. I-V characteristics of the single crystalline Si solar cell with (b) and without (a) the SSCT method.

Table 4-2. Characteristics of the single crystalline Si solar cells with and without the SSCT method.

Solar cell sample	V_{OC} (V)	J_{SC} (mA/cm^2)	FF	% n
Polished Si(100)	0.561	27.3	0.774	11.9
SSCT treated Si(100)	0.567	38.8	0.754	16.6

Due to the ultra-low reflectivity of the nanocrystalline Si surface after the SSCT method, the nanocrystalline Si solar cell was able to generate a high photocurrent density. The ultra-low reflectivity nanocrystalline Si surface can absorb more of incoming light resulting in production of more electron-hole pairs. The production of more electron-hole pairs resulted in high photocurrent density. The great increase in surface area [17-19] for the nanocrystalline Si was not observed to decrease the open circuit voltage, i.e., increase in surface recombination. In chapter 3, it was observed that the minority carrier lifetime was increased after the production of the nanocrystalline Si surface. The minority carrier lifetime greatly affects the open-circuit voltage, i.e., 10 times increase in minority carrier lifetime results to a 30 mV increase in open-circuit voltage (to be discussed in chapter 5). However, the effect of the band-gap widening and the great increase in minority carrier lifetime (i.e., from chapter 3) for a p-Si surface after the SSCT didn't actually translate to a great increase in open-circuit voltage. The total dark current is equal to the dark current of the front area and the back area. Without BSF, the dark current in the back area is greater than the dark current in the front area. Therefore, the open-circuit voltage is determined by the dark current in the back area which explains the small increase in the open-circuit voltage after the SSCT. The slight decrease in fill factor might be due to series resistance arising from poor

contact between the nanocrystalline Si and the Ag electrode.
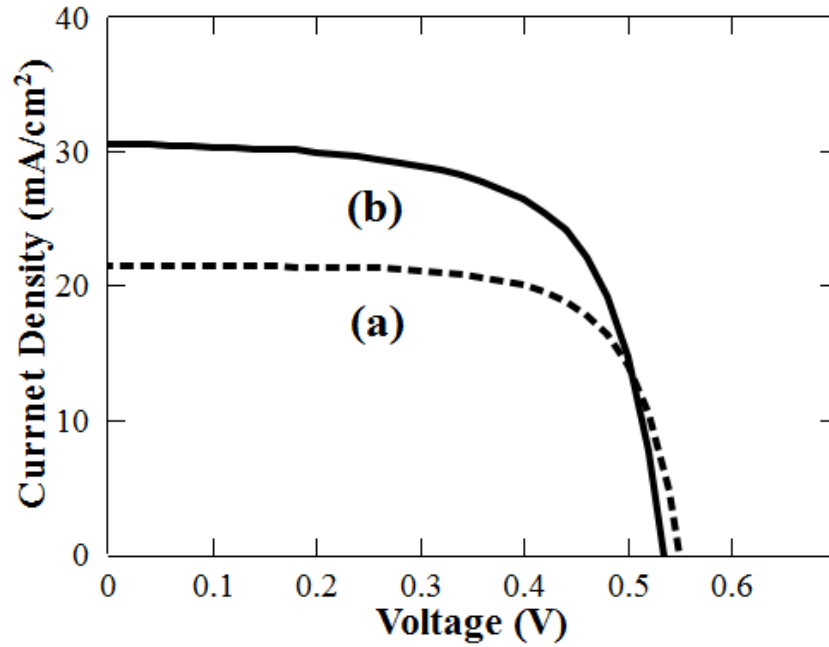
Fig. 4-10. I-V characteristics of the polycrystalline Si solar cell with (b) and without (a) the SSCT method.

Fig. 4-10 shows the current-voltage characteristics of the polycrystalline Si with and without the SSCT method. Table 4-3 summarizes the V_{oc}, J_{sc}, FF, and efficiency of the solar cells shown in Fig. 4-10. The short-circuit photocurrent density of the polycrystalline Si solar cells without SSCT increased from 21.5 mA/cm^2 to 30.5 mA/cm^2 with the SSCT method, an increase of 42%. However, both the open-circuit voltage and fill factor were observed to decrease from 0.550 V and 0.700, respectively, of the saw damage removed polycrystalline Si to 0.535 V and 0.655, respectively, after SSCT. The solar cell conversion efficiency increased from 8.3% without SSCT to 10.7% with SSCT, an increase of 29% and an absolute increase of 2.4%.

Table 4-3. Solar cell parameters of the polycrystalline Si with and without the SSCT method.

Solar cell sample	V_{OC} (V)	J_{SC} (mA/cm^2)	FF	% n
Polycrystalline Si	0.550	21.5	0.700	8.3
SSCT treated polycrystalline Si	0.535	30.5	0.655	10.7

As with the SSCT treated single crystalline Si solar cells, the SSCT treated polycrystalline Si solar cells were also found to increase in the photocurrent density by 42% as compared to without SSCT. However, the open-circuit voltage and fill factor were observed to have significant decreases. Phosphorus diffusion in polycrystalline Si may also occurs through the grain boundaries [20-21]. As shown in the earlier section, diffusion through the nanocrystalline Si/Si structure is surface enhanced as compared to a flat surface. Therefore, the enhancement in phosphorus diffusion could have also increased the recombinations occurring at the grain boundaries resulting to a lower open-circuit voltage. The decrease in fill factor might be due to series resistance arising from poor contact between the nanocrystalline Si and the Ag electrode.

## 4-4 Summary

Simple structured solar cells without antireflection coating and BSF were produced from the ultra-low reflectivity Si surfaces fabricated by the surface structure chemical transfer method. The solar cells produced were observed to generate high photocurrent density, i.e., 38.8 mA/cm^2, a 42% increase as compared to without SSCT even in the absence of an anti-reflection coating.   The high photocurrent density was attributed to the production of more electron-hole pairs due to the absorption of more light. The high photocurrent density leads to a high conversion efficiency of 16.6%, an absolute increase of 4.7% compared to without SSCT.

References

[1]   M.A. Green, J. Zhao, A. Wang, S.R. Wenham, *Electron Devices, IEEE Transactions on* **46** 1940 (1999)

[2]   H. R. Philipp and E.A. Taft, *Phys. Rev*. **120** 37 (1960)

[3]   Z. Huang, N. Geyer, P. Werner, J. de Boor, and U. Gosele, *Advanced Materials* **23** 285 (2011)

[4]   P. Lianto, S. Yu, J. Wu, C.V. Thompson, and W.K. Choi, *Nanoscale* **4** 7532 2012

[5]   S. Yae, T. Kobayashi, T. Kawagishi, N. Fukumuro, and H. Matsuda, *Sol. Ener*. **80**, 701 (2006)

[6]   X. Li, and P.W. Bohn, *Appl. Phys. Lett*. **77** 2572 (2000)

[7]   C. Chartier, S. Bastide, and C. Levy-Clement, *Electrochimica Acta* **53** 5509 2008

[8]   K. Tsujino, M. Matsumura, and Y. Nishimoto, *Sol. Energy Mater. Sol. Cells*. **90** 100 (2006)

[9]   H. Lv, H. Shen, Y. Jiang, C. Gao, H. Zhao, and J. Yuan, *Appl. Surf. Sci*. **258** 5451 (2012)

[10]   J. Oh, H. Yuan, and H. Branz, *Nature Nanotechnology* **7** 743 (2012)

[11]   D. Mathiot, A. Lachiq, A. Slaoui, J. Muller, and C. Dubois, *Materials Science in Semiconductor Processing* **1** 231 (1998)

[12]   S. Sen, J. Siejka, A. Savtchouk, and J. Lagowski, Appl. Phys. Lett. 70 2253 (1997)

[13]   Z. Liu, H. Takato, C. Togashi, and I. Sakata, *Appl. Phys. Lett*. **96** 153503 (2010)

[14]   J. Kato, and Y. Ono, *J. Electrochem. Soc*. **132** 1730 (1985)

[15]   F. Toor, M.R. Page, H.M. Branz, and H.C. Yuan, *37th IEEE PVSC Proceedings* (2011) 000020-000024

[16]   I. M. Mackintosh, *J. Electrochem. Soc*. **109** 392 (1962)

[17]   J. Buriak, *Phil. Trans. R. Soc. A*. **364** 217 (2006)

[18]   N. Nama, M. Abdulsattar, and Ahmed Abdul-Lettif, *Journal of Nanomaterials* **2010** 952172 (2010)

[19]   J. Sailor, and E. Lee, *Advanced Materials* **9** 783 (1997)

[20]   K. Schimpf, J. Palm, and H. Alexander, *Cryst. Res. Tech*. **29** 1123 (1994)

[21]   A. Bentzen, B.G. Svensson, E.S. Marstein, and A. Holt, *Sol. Energ. Mat. Sol. Cells* **90** 3193 (2006)

Chapter V

Changes in Minority Carrier Lifetime of Hydrogen-Terminated Si Surfaces in Dry- and Wet-Air

5-1   Introduction

Chapter 3 introduced a simple method to produce ultra-low reflectivity Si surfaces by the surface structure chemical transfer method. And in chapter 4, solar cells were produced from the ultra-low reflectivity surfaces and were observed to generate a high photocurrent density due to the avoidance of reflection loss. However, in order to achieve high efficiency solar cells, surface recombination must be greatly reduced. Therefore, surface passivation methods must be done in order to reduce the surface recombination and increase the photogenerated minority carrier lifetime.   In this chapter, minority carrier lifetime changes of H-terminated Si surfaces were investigated and the changes in the chemical species present on the Si surface due to surface oxidation in air.

Study on initial oxidation of Si is of importance not only from an academic viewpoint but also for application to semiconductor products such as solar cells and LSI. Semiconductor devices are usually fabricated using Si wafers after cleaning with the RCA method [1] followed by hydrofluoric acid (HF) etching. HF-etching forms ideal hydrogenterminated Si surfaces (i.e., only mono-hydride, Si-H) in the case of Si(111), [2] while mono-, di- (Si-H$_2$), and tri- (Si-H$_3$) hydride species are produced on technologically more important Si(100) surfaces [3–5]. HF-etched Si(100) surfaces with Si-H$_2$ and Si-H$_3$ are less stable in air than Si(111). Oxidation of HF-treated Si surfaces is enhanced by the presence of metal contaminants, more active species, defects, fluorineadsorbed sites, etc., [6,7]. Initial oxidation of HF-treated Si surfaces were investigated using Fourier transform infrared spectroscopy (FT-IR), X-ray photoelectron spectroscopy (XPS), Ultraviolet photoelectron spectroscopy (UPS),

etc.6–9 Chabal et al., [6] reported that when HF-treated Si(100) surfaces were kept in air, vibrational peaks due to SiH, SiH$_2$, SiH(O)$_3$, and SiH$_2$(O)$_2$ were observed, indicating that O atoms occupied back-bonds with Si-H bonds remaining on Si surfaces. Hirose et al., [7] also concluded that oxygen attacked Si back-bonds and surface Si-H bonds were still present after the oxygen attack. The minority carrier lifetime strongly affects the electrical characteristics of semiconductor devices [10]. It is greatly decreased by the presence of defect states such as interface states [11,12]. In the case of solar cells, photovoltages are markedly influenced by the minority carrier lifetime [13].

To show how the minority carrier lifetime (τ_{eff}) affects the open-circuit photovoltage (V_{oc}), V_{oc} is described as:

$$V_{oc} = \frac{k_B T}{q} \ln\left(\frac{J_{ph}}{J_0} + 1\right)$$

(5-1)

The reverse saturation current density, J_o is given by:

$$J_o = q n_i^2 \left(\frac{D_p}{L_p N_D} + \frac{D_n}{L_n N_A}\right)$$

(5-2)

where n_i is the intrinsic carrier density, D_p is the hole diffusion coefficient, D_n is the electron diffusion coefficient, N_D is the donor concentration, N_A is the acceptor concentration, L_p is the hole diffusion length, and L_n is the electron diffusion length. For p-type Si-based solar cells, $N_D \gg N_A$, then we have

$$J_o \approx \frac{q n_i^2 D_n}{L_n N_A} \qquad (5\text{-}3)$$

where,

$$L_n = \sqrt{D_n \tau_{eff}} \qquad (5\text{-}4)$$

Therefore, as the minority carrier lifetime increases (decreases), the dark current density decreases (increases), and results in an increase (decrease) of the photovoltage. Combinations of equations (5-3) and (5-4) shows V_{oc} increases by 30 mV with an increase in minority carrier lifetime by one order.

Recombination of electron-hole pairs generated in the surface region proceeds at surface states, resulting in a decrease in the quantum efficiency of short-wavelength light, and thus in a decrease in the photocurrent density [14]. Recombination currents possess a large ideality factor, e.g., 2, [15] and thus, a fill factor is also decreased.

In this chapter, changes of minority carrier lifetime for HF-treated Si surfaces with time kept in dry- and wet-air air have been investigated. It was found that the minority carrier lifetime strongly depends on humidity.

5-2   Experiments

Phosphorus-doped n-type Si(100) wafers with 1 ~ 10 Ω·cm resistivity were cut into 2.5×2.5 cm^2 pieces and cleaned using the RCA method. Then, the wafers were immersed in 0.5 wt% HF solutions for 2 min, followed by rinse with ultra-pure water. The HF-treated Si wafers were kept in air with the humidity of either 5 or 95% at room temperature. Hereafter, air with 5 and 95% humidity is called dry-air and wet-air, respectively.

Minority carrier lifetime of the Si wafers was determined from measurements of microwave reflectivity decay caused by 904 nm wavelength incident light with a carrier injection density of 1×10^{15}/cm^3 using a KOBELCO Wafer LTA-1510. XPS measurements were carried out using a VG Scientific ESCALAB 220i-XL spectrometer with a monochromatic Al Kα radiation source. Photoelectrons were detected in the surface-normal direction. Measurements of workfunction changes were performed by a contact potential difference method using a McAllister KP6500 Digital Kelvin Probe.

5-3 Results and discussion

5-3-1 Changes in minority carrier lifetime in wet- and dry-air

Figure 5-1 shows changes of the minority carrier lifetime for the HF-treated Si(100) specimens vs. the time kept in wet- (curve a) and dry-air (curve b). The lifetime value of the Si wafers before HF treatment was 32 μs. The initial lifetime measured after 5 min exposure to wet-air (~78 μs) was higher than that to dry-air (~63 μs). In the initial stage, the lifetime decreased rapidly with time, followed by a slow decrease beyond 12 h. Over 20 h, the lifetime became almost constant. The lifetime for the HF-treated Si specimens in wet-air decreased more rapidly than that in dry-air.

5-3-2 Changes in minority carrier lifetime in wet- and dry-air switched at 12 h

Figure 5-2 also shows the lifetime changes vs. the time. For curve a, the HF-treated Si(100) specimens were kept in wet-air up to 12 h, and then the atmosphere was switched to dry-air. The lifetime increased immediately after changing the atmosphere followed by a slow decrease. In cases where the atmosphere was changed from dry-air to wet-air at 12 h (curve b), on the other hand, the lifetime decreased more rapidly up to 15 h than that in dry-air up to 12 h.
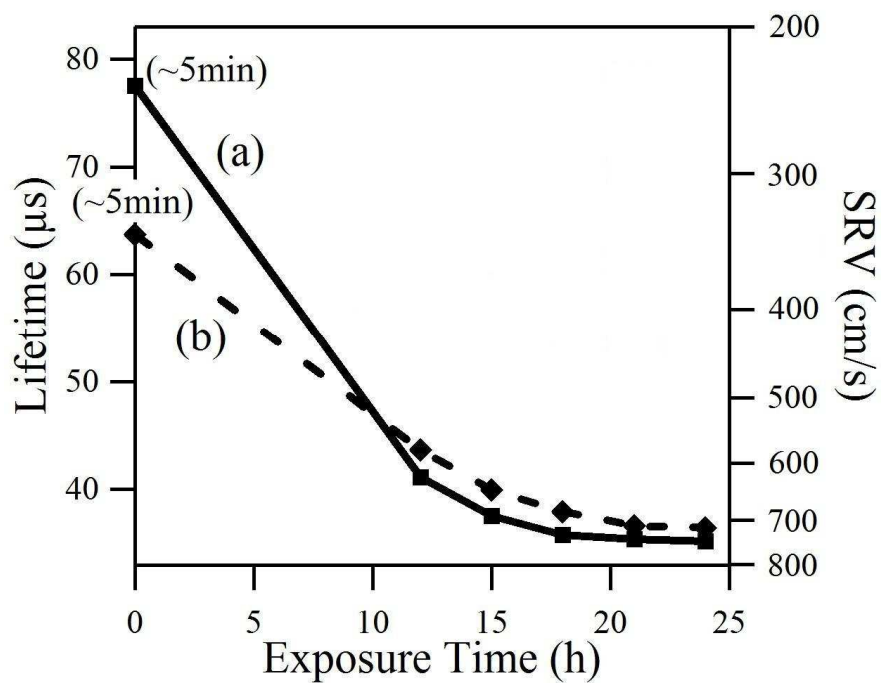
Fig. 5-1. Minority carrier lifetime of the HF-treated Si(100) surfaces vs. the period of time kept in wet-air (a) and dry-air (b). Surface recombination velocity (SRV) was roughly estimated from the minority carrier lifetime.
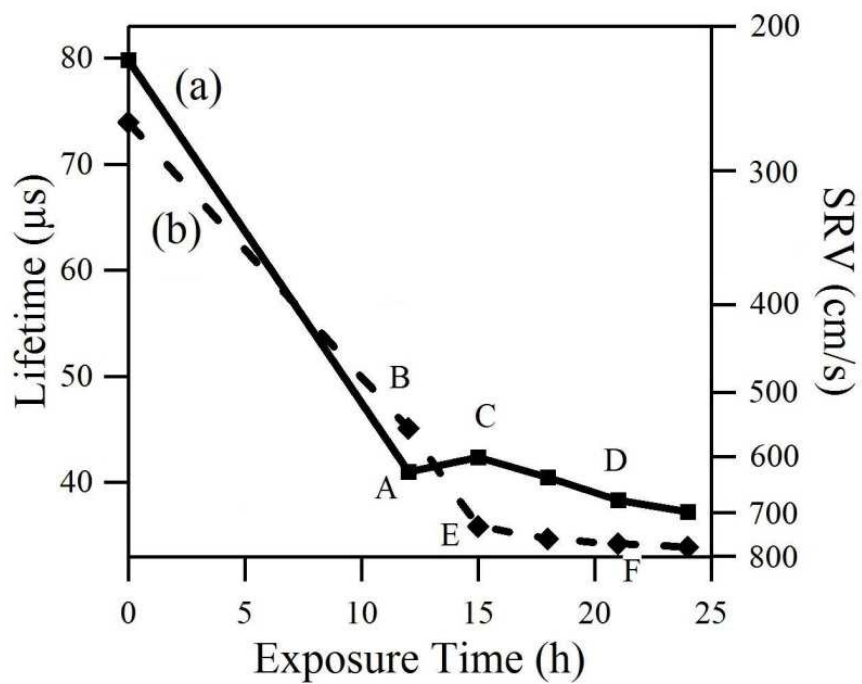
Fig. 5-2. Minority carrier lifetime of the HF-treated Si(100) surfaces vs. the period of time in the following atmospheres: (a) wet-air switched to dry-air at 12 h; (b) dry-air switched to wet-air at 12 h. Surface recombination velocity (SRV) was roughly estimated from the minority carrier lifetime.

5-3-3 XPS measurements in wet- and dry-air switched at 12 h

Figures 5-3a and 5-3b show the normalized XPS spectra in the O 1s and Si 2p regions, respectively, for the HF-treated Si(100) surfaces. The XPS peak areas were normalized to that of the Si substrate in the Si 2p region for each specimen. Spectra A to F were observed at points A to F, respectively, in Figure 2. Table 5-1 summarized the normalized peak areas for the hydroxyl groups (C_{SiOH}) and bridge-backbonded O atoms ($C_{Si-O-Si}$) in the O 1s region and the ratio of $C_{SiOH}/C_{Si-O-Si}$. For the specimen kept in dry-air for 12 h (spectrum B), only one peak attributable to bridge-backbonded O atoms was observed in the O 1s region while other spectra were deconvoluted into two peaks at 533.1 eV and 532.1 eV due to O atoms in OH species and in Si-O-Si bridges, respectively [16,17]. It is easily inferred that O atoms in OH species are less negatively charged than those in Si-O-Si bridges because the electronegativity of hydrogen atoms (2.1) is higher than that of Si atoms (1.8), and therefore hydrogen atoms are less positively charged than Si atoms. C_{SiOH} and $C_{Si-O-Si}$ increased with exposure time. When the atmosphere was switched from wet- to dry-air at 12 h and kept in dry-air for 3 and 9 h, the $C_{SiOH}/C_{Si-O-Si}$ ratio decreased from 0.768 (spectrum A) to 0.713 (spectrum C) and 0.708 (spectrum D), indicating dominant formation of bridge-backbonded O atoms. When the atmosphere was switched from dry- to wet-air at 12 h and kept in wet-air for 3 and 9 h, the $C_{SiOH}/C_{Si-O-Si}$ ratio increased from 0 (spectrum B) to 1.75 (spectrum E) and 2.45 (spectrum F), indicating dominant formation of OH species. In the Si 2p spectra for 1 h exposure to wet-air, no peak was present in the higher energy region of the substrate Si $2p_{3/2}$ and $2p_{1/2}$ peaks. When the exposure time was increased to more

than 12 h, a clear peak appeared at 104 eV in the Si 2p region for the spectra of C to F, and attributable to SiO_2, i.e., an O atom bound to four Si atom [18,19]. From the area intensity ratio between the substrate peaks and the SiO_2 peak, the SiO_2 thickness was estimated to be 0.07, 0.22, 0.41, and 0.59 nm for points C, D, E and F, respectively [20].
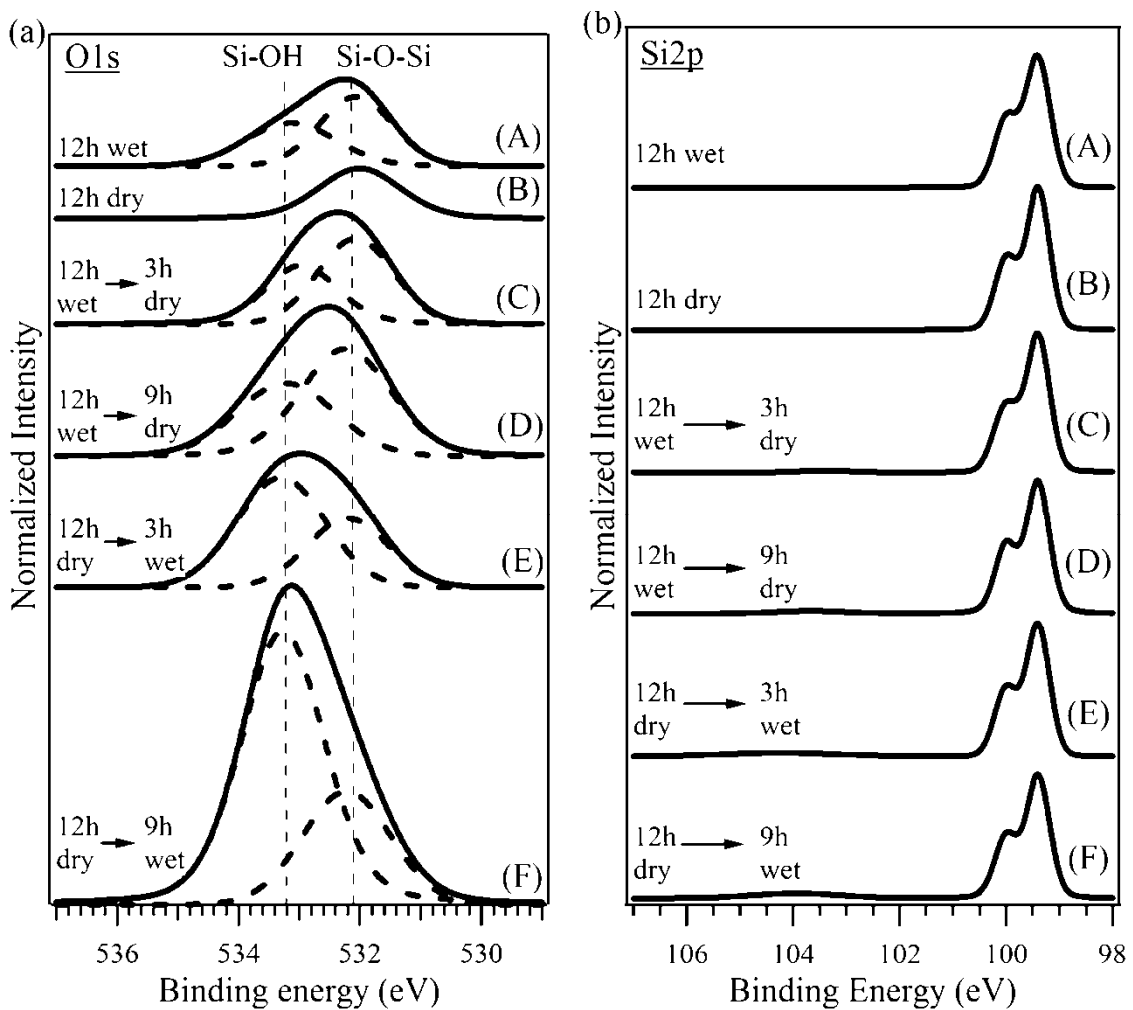
Fig. 5-3. Normalized XPS spectra in the O 1s (a) and Si 2p (b) regions for the H-terminated Si(100) surfaces The top, the second, the third, the fourth, fifth and the bottom spectra correspond to points A, B, C, D, and E, respectively, in Figs. 2 and 4.

113

TABLE 5-1. Normalized XPS peak area and peak ratio of the SiOH and Si-O-Si species after deconvolution of the O 1s spectra.

sample	C_{SiOH}/C_{Si}	$C_{Si\text{-}O\text{-}Si}/C_{Si}$	$C_{SiOH}/C_{Si\text{-}O\text{-}Si}$
(A) 12 h wet	1.21	1.58	0.768
(B) 12 h dry	---	1.38	0.000
(C) 12 h wet → 3 h dry	1.45	2.04	0.713
(D) 12 h wet → 9 h dry	2.24	3.17	0.708
(E) 12 h dry → 3 h wet	3.06	1.74	1.75
(F) 12 h dry → 9 h wet	7.65	3.12	2.45

5-3-4 Discussion of minority carrier lifetime and XPS results

The initial lifetime in wet-air is higher than that in dry-air. Water is partially dissociatively adsorbed on Si, leading to formation of Si-H and Si-OH [23]. Therefore, it is very likely that adsorption of water on H-terminated Si surfaces causes replacement of Si-H to Si-OH (Figure 5-4b) without formation of Si dangling bonds, resulting in the higher lifetime. On the other hand, oxygen adsorption requires the formation of strained Si-O-Si bonds on the surface (Figure 5-4a), probably resulting in the formation of surface Si dangling bonds. From the above argument, it can be concluded that surface OH results in higher lifetime than surface O while backbonded OH lowers the lifetime more greatly than bridge-backbonded O. These results indicate that Si wafers should be processed immediately after HF etching or HF-treated Si wafers be kept in dry-air.
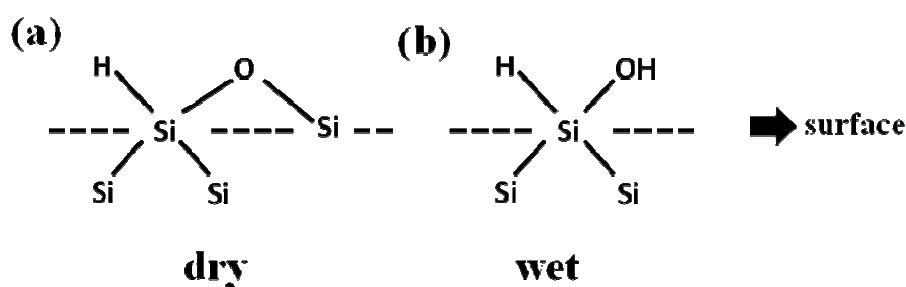

Figure 5-4. Surface chemical species present after ~5 min exposure in dry- (a) and wet-air (b). The dotted line represents the Si surface.

When the H-terminated Si surfaces are kept in air, the lifetime is greatly decreased with time. The lifetime decrease is caused by attack of back-bonds by oxygen and water. The faster decrease in wet-air is because OH species (Figure 5-5b) cannot form network structure, resulting in a high dangling bond density as reported for native oxide growth on HF-treated Si(111) [21,22] while O atoms (Figure 5-5a) can form network structure (i.e., SiO_2), leading to a lower density of Si dangling bonds.
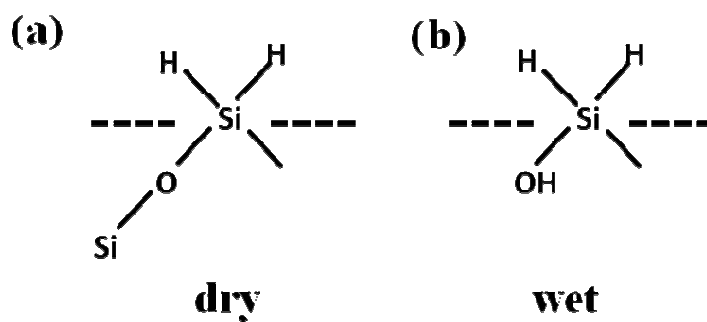
Figure 5-5. Surface chemical species present after exposure over time in dry- (a) and wet-air (b). The dotted line represents the Si surface.

When the atmosphere is switched from wet- to dry-air, the concentration of bridge-backbonded O (Figure 5-6a) increases (C in Table 5-1), accompanied with an increase in the lifetime (C in Figure 5-2). By switching the atmosphere from dry- to wet-air, on the other hand, the rate of the lifetime decrease is enhanced (E in Figure 5-2). These results demonstrate that the density of defect states resulting from OH species inserted into the Si-Si backbonds (Figure 5-6b) is much higher than that from bridge-backbonded O atoms.

116
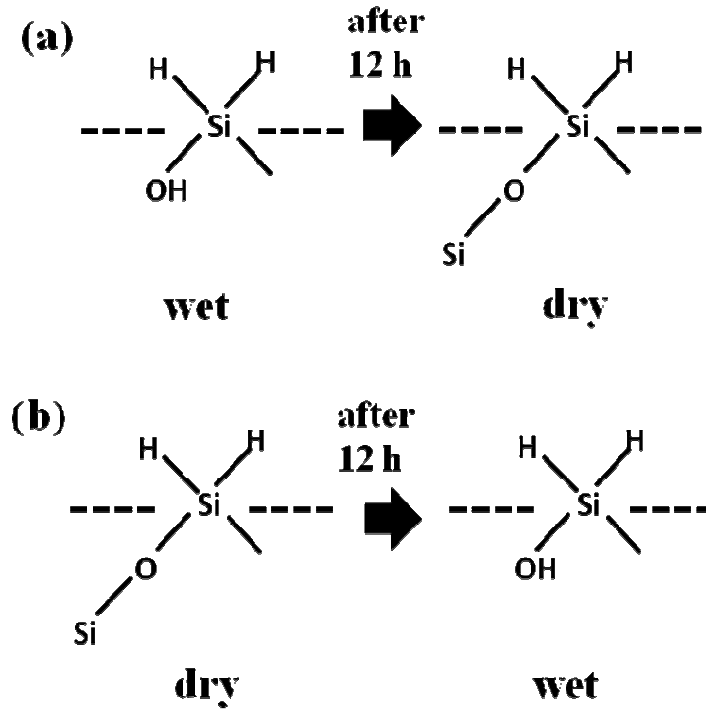
Figure 5-6. Surface chemical species present after switching at 12 h from wet- to dry-air (a) and dry- to wet-air (b). The dotted line represents the Si surface.

The chemical states of the Si surface changed during exposure to dry- and wet-air, as described above. This leads to changes in the surface recombination velocity which directly affects the minority carrier lifetime of the Si wafers. The surface recombination velocity, S, can be estimated using the following equation: [24,25]

$$\frac{1}{\tau_{eff}} = \frac{1}{\tau_{bulk}} + \frac{1}{\tau_s} = \frac{1}{\tau_{bulk}} + \frac{1}{\dfrac{d^2}{\pi^2 D} + \dfrac{d}{2S}} \qquad (5\text{-}5)$$

where τ_{eff} is the effective lifetime, τ_{bulk} is the bulk lifetime, τ_S is the surface lifetime, d is the thickness of the Si wafer, D is the hole diffusion constant of ~12 cm^2/s, and S is the surface recombination velocity. The bulk lifetime, τ_{bulk} is estimated to be ~190 μs, assuming the iodine passivation completely eliminates surface recombination, and using this value, the surface recombination velocity, S, is calculated as shown in the vertical axis of Figures 5-1 and 5-2.

5-3-5 Workfunction changes in wet- and dry-air switched at 12 h

Figure 5-8 shows the workfunction change of the HF-treated Si(100) surfaces vs. the period of time kept in air. For curve a, the atmosphere was switched from wet- to dry-air at 12 h, and vice versa for curve b. For both the curves, the workfunction initially decreased. If replacement of surface Si-H to surface Si-OH or Si-O was the dominant reaction, the workfunction would increase because a net charge on OH and O is more negative than H on the surface (Figure 5-7a). Inclusion of OH and/or O in the Si-Si backbonds (i.e., below the surface), on the other hand, decreases the workfunction (5-7b). The decrease in the workfunction indicates that insertion of OH and O in the Si-Si backbonds is dominant over replacement of surface H to OH or O. This mechanism is in good agreement with the FT-IR observation that by leaving HF-treated Si surfaces in air, Si-O-Si bonds are formed with Si-H bonds remaining on the surfaces [5,6].

118
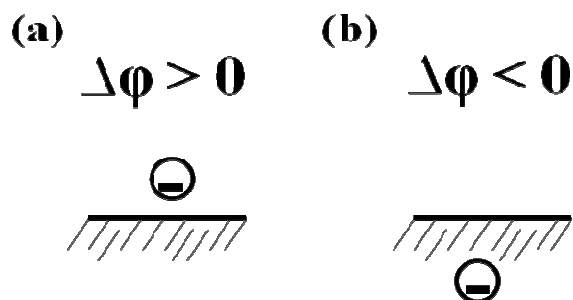
Figure 5-7. Workfunction changes in the presence of an electronegative chemical specie above (a) and below (b) the surface.

When the atmosphere was switched from dry-air to wet-air, the workfunction increased (E in Figure 5-7). Replacement of bridge-backbonded O to backbonded OH increases the workfunction, while that of surface O to surface OH decreases it. Therefore, it can be concluded that replacement in backbond sites is the dominant reaction. By switching the atmosphere from wet-air to dry-air, the workfunction decreased more rapidly (plot a). This result indicates that replacement of backbonded OH to bridge-backbonded O is dominant. These mechanisms can also well explain the lifetime change, as explained above.

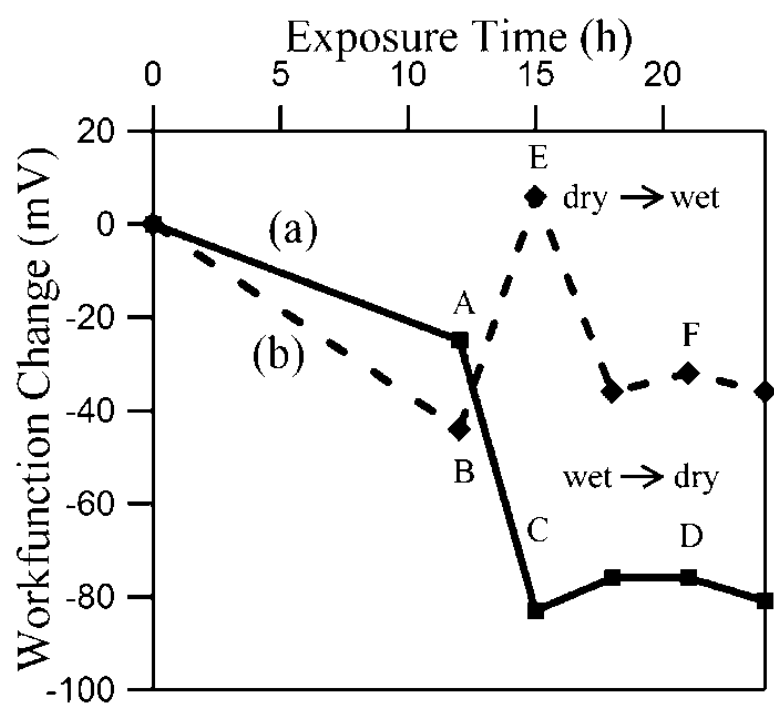Fig. 5-8. Workfunction changes of the HF-treated Si(100) surfaces in the following atmospheres: (a) wet-air switched to dry-air at 12 h; (b) dry-air switched to wet-air at 12 h.

5-4　Summary

The initial minority carrier lifetime of the H-terminated Si(100) was higher for Si surfaces exposed to wet-air than Si surfaces exposed to dry-air. Surface Si-OH is formed in wet-air, while strained Si-O-Si is formed in dry-air. When the H-terminated Si surfaces are kept in air, the minority carrier lifetime is decreased with time, due to the insertion of O and OH in Si-Si backbonds. Bridge-backbonded O forms Si-O-Si network structure while backbonded OH does not, and therefore, the decrease in the minority carrier lifetime in wet-air is larger than that in dry-air. On the other hand, surface O results in a lower lifetime than surface OH. When the atmosphere is switched between dry-air and wet-air, formation of backbonded O (or OH) is the dominant reaction.

(i)　　In wet-air:　　Si-OH-bonds $\rightarrow$ no network formation $\rightarrow$ high dangling bond density $\rightarrow$ low minority carrier lifetime

(ii)　　In dry-air:　　Si-O-Si $\rightarrow$ network formation $\rightarrow$ low dangling bond density $\rightarrow$ high minority carrier lifetime

(iii)　　For Si wafer processing:　　It is highly recommended that the Si specimens be kept in N_2 ambient or processed immediately to prevent the formation of native oxides

References

[1]   W. Kern and D. A. Puotinen, *RCA Rev.* 187 (1970)

[2]   G. S. Higashi, Y. J. Chabal, G. W. Trucks, and K. Raghavachari, *Appl. Phys. Lett.* **56**, 656 (1990)

[3]   Y. J. Chabal, G. S. Higashi, K. Raghavachari, and V. A. Burrows, *J. Vac. Sci. Technol.* **A7**, 2104 (1989)

[4]   M. Nishida, M. Okuyama, and Y. Hamakawa, *Appl. Surf. Sci.* **79/80**, 409 (1994)

[5]   G. F. Cerofolini, A. Giussani, A. Modelli, D. Mascolo, D. Ruggiero, D. Narducci, and E. Romano, *Appl. Surf. Sci.* **254**, 5781 (2008)

[6]   F. Hirose, M. Nagato, Y. Kinoshita, S. Nagase, Y. Narita, and M. Suemitsu, *Surf. Sci.* **601**, 2302 (2007)

[7]   X. Zhang, E. Garfunkel, Y. J. Chabal, S. B. Christman, and E. E. Chaban, *Appl. Phys. Lett.* **79**, 4051 (2001)

[8]   G. F. Cerofolini, E. Romano, D. Narducci, P. Belanzoni, and G. Giorgi, *Appl. Surf. Sci.* **256**, 6330 (2010)

[9]   M. Wilde, K. Fukutani, S. Koh, K. Sawano, and Y. Shiraki, *J. Appl. Phys.* **98**, 023503 (2005)

[10]   S. Rein, Lifetime Spectroscopy: A Method of Defect Characterization in Silicon for Photovoltaic Applications, Springer, Germany, 2005

[11]   Y. D. Kim, S. Park, J. Song,S. J. Tark, M, G. Kang, S. Kwon, S. Yoon, and D. Kim, *Solar Energy Mater. Solar Cells,* **95**, 73 (2011)

[12]   C. L. Garrido, D. Stolik, J. Rodriguez, and A. Morales, *Solar Ener. Mater. Solar Cells,* **57**, 239 (1999)

[13] A. Datta, J. Damon-Lacoste, M. Nath, P. Rocai Cabarrocas, and P. Chatterjee, *Mater. Sci. Eng.* **B159-160**, 10 (2009)

[14] A. Luque, and S. Hegedus, Handbook of Photovoltaic Science and Engineering, John Wiley and Sons, UK, (2011)

[15] C.T. Sah, R.N. Noyce, and W. Shockley, *Proc. Inst. Radio Engrs.* **45**, 1228 (1957)

[16] D. Briggs, and M.P. Seah, Practical Surface Analysis, Auger and X-ray Photoelectron Spectroscopy, Vol. 1, John Wiley & Sons, New York, (1990)

[17] R.K. Schulz, and J.F. Evans, *Appl. Surf. Sci.* **81**, 449 (1994)

[18] K.-J. Kim, J.-S. Jang, and D.-W. Moon, *Metrologia* **43**, L28 (2006)

[19] S. Ichimura, A. Kurokawa, K. Nakamura, H. Itoh, H. Nonaka, and K. Koike, *Thin Solid Films*, **377-378**, 518 (2000)

[20] F.J. Himpsel, F.R. McFeely, A. Taleb-Ibrahimi, J.A. Yarmoff, and G. Hollinger, *Phys. Rev. B* 38, 6084 (1988)

[21] H. Angermann, Th. Dittrich, H. Flietner, *Appl. Phys.* **A59**, 193 (1994)

[22] W. Henrion, M. Rebien, H. Angermann, A. Röseler, *Appl. Surf. Sci.* **202**, 199 (1994)

[23] D. Gräf, M. Grundner, R. Schulz, and L. Mühlhoff, *J. Appl. Phys.* **68,** 5155 (1990)

[24] K. Peter, R. Kopecek, E. Enebakk, A. Soiland, and S. Grandumand, Abstract of 35th Photovoltaic Specialists Conference (2010) 799-805

[25] Z. Liu, A. Masuda ad M. Kondo, *J. Appl. Phys.* **103**, 104909 (2008)

[26] T. S. Horanyi, T. Pavelka, and P. Tutto, Appl. Surf. Sci. 63, 306 (1993)

Chapter VI

General Conclusion

In this thesis, chemical methods for the improvement of solar cell processes and devices were studied. Ultra-low reflectivity Si surfaces were fabricated by the process called the surface structure chemical transfer (SSCT) method. The ultra-low reflectivity Si surfaces were then used to produce solar cells. Lastly, oxidation in air of the HF-treated Si wafers was evaluated by minority carrier lifetime measurements.

Ultra-low reflectivity (i.e., 2~4%) Si surfaces were produced by the surface structure chemical transfer method. A Pt catalytic mesh was contacted with a Si wafer in $HF:H_2O_2$ solutions. The ultra-low reflectivity was attributed to the formation of a nanocrystalline Si surface having a thickness in the range between 100 and 150 nm. Photoluminescence at 670 nm was observed due to the presence of Si nanocrystals whose diameter is ~ 2.5 nm. The increase in minority carrier lifetime (i.e., from 1 μs to 5 μs) was attributed to the band-gap widening of Si after the formation of the nanocrystalline Si layer due to the suppression of electron-hole pair recombination at the nanocrystalline Si/Si interface.

High photocurrent density (i.e., 38.8 mA/cm^2) nanocrystalline Si/Si structured solar cells were fabricated without an anti-reflection coating. The pn-junction was formed simply by spin-doping a P-dopant source onto the nanocrystalline Si/Si structure and diffusion at high temperature (i.e., 950°C). The high photocurrent density was attributed to the ultra-low reflectivity surface due to the absorption of more light. The open-circuit voltage was not decreased, which means that the surface recombination was not increased after the formation of the nanocrystalline Si layer. The solar cell efficiency (i.e., 16.6%) obtained was relatively high considering no anti-reflection coating and no passivation methods were performed.

Exposure of HF-treated Si wafers in air result to the formation of native oxides within one-day of exposure. However, depending on the humidity conditions, the decrease in minority carrier lifetime varies. In wet-conditions, interstitial Si-OH species are dominant which cannot form a network structure resulting to a lower minority carrier lifetime. In dry-conditions, interstitial Si-O-Si species are dominant which can form a network structure resulting to higher minority carrier lifetime.

The surface structure chemical transfer (SSCT) method is a fast and simple method to produce ultra-low reflectivity Si surfaces. High photocurrent density Si solar cells can be easily fabricated from the nanocrystalline Si/Si structured surface. To further increase the conversion efficiency of the Si solar cells, a stable passivation method must be performed, along with the optimized: pn-junction formation, edge-isolation and back-surface field processes.

List of Publications

Publications arising from the work in this thesis

Refereed Journal Papers

[1]   F. F. Jr. Corpuz, T. Matsumoto, W.-B. Kim, H. Kobayashi, "Changes in
minority carrier lifetime of hydrogen-terminated Si surfaces in dry- and wet-air"
ECS. Solid-State Lett., **1** 89 (2012)

[2]   K. Imamura, F. Franco Jr., T. Matsumoto, and H. Kobayashi "Ultra-low
reflectivity polycrystalline silicon surfaces formed by surface structure chemical
transfer method" *Appl. Phys. Lett*. **103**, 013110 (2013)

Conference Oral Presentations

[3]   F.C. Franco Jr.，金佑柄，小林光，Stability of Nitric Acid Oxidized Silicon
Wafers Evaluated by Microwave Photoconductance Decay
Spectroscopy，日本物理学会大66回年次大会，新潟，2011年3月25日～28
日

[4]   Francisco C. Franco Jr., Woo-Byoung Kim, Hikaru Kobayashi，Initial Stages of
Oxidation of HF Passivated Si(100) Evaluated by Carrier
Lifetime，物理学会2011年秋季大会，富山，2011年9月21日～24日

[5]   F. Franco, Jr., W.-B. Kim, H. Kobayashi, Dependence minority carrier lifetime
on humidity for initial oxidation of Si, The 6th International Symposium on
Surface Science, Tokyo, December 11-15, 2011

[6]   F. Franco，今村健太郎，小林光，Ultra-low reflectivity poly-crystalline Si surfaces fabricated by surface structure chemical transfer method，第60回応用物理学関係連合講演会，神奈川，2013年3月27日〜30日

Poster Presentations

[7]   F. Franco Jr., W.-B. Kim, H. Kobayashi, Humidity condition dependence of the initial stages of Si oxidation, The 15th SANKEN International Symposium and the 10th SANKEN Nanotechnology Symposium, Osaka, Jan. 12-13, 2012

Acknowledgments

I would like to express my deepest appreciation to everyone who made the writing of this thesis possible.

I would like to express my indebted gratitude to Professor Hikaru Kobayashi, for all his encouragement, ideas, knowledge, time and allowing me to learn and grow under his supervision.

I am very grateful to Associate Professor Masao Takahashi and Assistant Professor Taketoshi Matsumoto for all the discussions, knowledge, and advice. I would also like to thank Dr. Woo-Byoung Kim and Assistant Professor Kentaro Imamura for the many meaningful discussions, close assistance in the experiments, and constant encouragement. I would also like to give my thanks to Dr. Yoshihiro Nakato, Dr. Sumio Terakawa, Dr. Tatsuo Saga and Dr. Shigeki Imai for all the discussions and advice.

I would also like to thank Ms. Chika Kurosaki for all the help and cooperation especially with the bureaucratic related matters. I would also like to express my appreciation to all the members of Kobayashi laboratory for all the support and help, especially with the Japanese translations and reading.

I would like to show my gratitude to Professor Toshiaki Munakata for all the advices and discussions for the improvement of this thesis. I am very grateful to Professor Michio Okada for all the support, encouragement, ideas, and many meaningful discussions.

I am very thankful to Dr. Toshio Kasai support, knowledge, and for giving me the opportunity. I am very much thankful to Dr. Gerardo Janairo and Dr. Derrick Yu at

De La Salle University Manila for all the advice and great support.

I am very grateful to all my friends in japan who made my stay in japan comfortable and bearable.

Last but not the least; I am very much thankful for the never ending support I received from my family throughout the last four years.